DISSERTATION

AN INVESTIGATION OF AN EAST PACIFIC EASTERLY WAVE GENESIS PATHWAY AND THE IMPACT OF THE PAPAGAYO AND TEHUANTEPEC WIND JETS ON THE EAST PACIFIC MEAN STATE AND EASTERLY WAVES

Submitted by

Justin W. Whitaker

Department of Atmospheric Science

In partial fulfillment of the requirements

For the Degree of Doctor of Philosophy

Colorado State University

Fort Collins, Colorado

Fall 2021

Doctoral Committee:

Advisor: Eric D. Maloney

Michael M. Bell
Kristen L. Rasmussen
Jeffrey D. Niemann

ABSTRACT

AN INVESTIGATION OF AN EAST PACIFIC EASTERLY WAVE GENESIS PATHWAY AND THE IMPACT OF THE PAPAGAYO AND TEHUANTEPEC WIND JETS ON THE EAST PACIFIC MEAN STATE AND EASTERLY WAVES

Part one of this dissertation investigates the transition of a Panama Bight mesoscale convective system (MCS) into the easterly wave (EW) that became Hurricane Carlotta (2012). Reanalysis, observations, and a convective-permitting Weather Research and Forecasting (WRF) model simulation are used to analyze the processes contributing to EW genesis. A vorticity budget analysis shows that convective coupling and vortex stretching are very important to the transition in this case, while horizontal advection is mostly responsible for the propagation of the system. In the model, the disturbance is dominated by stratiform vertical motion profiles and a mid-level vortex, while the system is less top-heavy and is characterized by more prominent low-level vorticity later in the transition in reanalysis. The developing disturbance starts its evolution as a mesoscale convective system in the Bight of Panama. Leading up to MCS formation the Chocó jet intensifies, and during the MCS to EW transition the Papagayo jet strengthens. Differences in the vertical structure of the system between reanalysis and the model suggest that the relatively more bottom-heavy disturbance in reanalysis may have stronger interactions with the Papagayo jet. Field observations like those collected during the Organization of Tropical East Pacific Convection (OTREC) campaign are needed to further our understanding of this east Pacific EW genesis pathway and the factors that influence it, including the important role for the vertical structure of the developing disturbances in the context of the vorticity budget.

In parts two and three of this dissertation, the Weather Research and Forecasting (WRF) model is used to quantify the impact that the Papagayo and Tehuantepec wind jets have on the east Pacific mean state and east Pacific easterly waves. Specifically, a control run simulation is compared with a gaps filled simulation, where mountain gaps in the Central American mountains are "filled in" to block the Papagayo and Tehuantepec wind jets. In the absence of these wind jets, the northern half of the east Pacific mean state becomes drier, supporting a reduction in convective activity and precipitation there. Further, a 700 hPa positive vorticity feature that is linked to the Papagayo jet is reduced. An easterly wave tracking algorithm is developed and shows that easterly wave track density and genesis density are generally reduced in the eastern half of the basin for the gaps filled run. An eddy kinetic energy (EKE) budget is also calculated and highlights that EKE, barotropic conversion, and eddy available potential energy (EAPE) to EKE conversion all decrease for easterly waves when the wind jets are blocked. A composite analysis reveals that there are slight horizontal structural changes between waves in the simulations, while the waves have surprisingly similar strengths. Overall, the Papagayo and Tehuantepec wind jets are shown to be supportive influences on east Pacific easterly waves.

ACKNOWLEDGEMENTS

First, I want to thank my wife, Alissa Williams. Alissa, thank you for seeing my potential as a scientist many years ago before I ever could. Thank you for believing in me and for motivating me to get to this point. I am so glad that we met at Wofford College — I've really enjoyed all of the memories that we have made together. Alissa, you are an incredible woman who pushes me to be better: I will always be amazed that you finished your Ph.D. and started a postdoc while pregnant. Next, I want to thank my advisor Eric Maloney and my committee members Kristen Rasmussen, Michael Bell, and Jeffrey Niemann. Eric, thank you for your support and understanding during my graduate career and for helping me develop as a scientist. Kristen, Michael, and Jeffrey, thank you for serving on my committee and for all of your questions about my dissertation research. To my family, Ray, Lauren, Steven, and Noah, thank you all for your support of my academic journey and for being such a loving family to grow up in. To Tyler Slonecki and Sean Freeman, thank you both for always being there for me; it has been cool to watch our friendships grow over the years. Finally, this research was made possible by funding from the National Science Foundation under Grant #AGS-1735978.

Thank you also to all of the teachers and coaches that I have had while at Free Home Elementary School, Macedonia Elementary School, Creekland Middle School, Creekview High School, Wofford College, and Colorado State University. Thank you to all of my friends from high school, Wofford, and CSU — I've been fortunate to meet great people during my education. Thank you to the members of the intramural sports teams that I have been on in Colorado; I have really enjoyed all of the kickball, flag football, and dodgeball games we played together. Thank you to Fort Collins Adaptive Recreation Opportunities for being a great organization to volunteer with. Thank you to Gordon, my cat, for your love — you were a great quarantine work buddy during the pandemic. Finally, I am thankful for the OTREC 2019 field campaign. I learned so much during my time in Costa Rica and I am grateful to have been a member of the team.

TABLE OF CONTENTS

LIST OF TABLES

LIST OF FIGURES

Chapter 1

Introduction

Since 2010, several studies have investigated east Pacific easterly waves, ranging from observational analyses (Huaman et al., 2021) to idealized modeling studies (Torres et al., 2021). A group of studies have examined the formation of east Pacific easterly waves (Serra et al., 2010; Toma and Webster, 2010; Rydbeck et al., 2017; Torres et al., 2021) without an African easterly wave precursor (e.g., Frank, 1970). Serra et al. (2010) showed that the region near the Papagayo jet was a location of easterly wave genesis from a wave tracking analysis. Toma and Webster (2010) examined how the east Pacific Intertropical Convergence Zone can support the generation of waves. Torres et al. (2021) showed that a mid level jet feature in the Caribbean and east Pacific can support wave growth from an idealized stratiform heating profile. Finally, Rydbeck et al. (2017) showed that Panama Bight mesoscale convective systems (MCSs) support easterly wave activity in the basin, and that they can grow into easterly waves.

Other easterly wave research has focused on environmental factors that impact their growth. One set of studies has examined how low-level wind jets and gap winds influence easterly wave development (Holbach and Bourassa, 2014; Whitaker and Maloney, 2018; Fu et al., 2021). Whitaker and Maloney (2018) examined how strong and weak phases of the Caribbean low-level jet modulated easterly wave eddy kinetic energy (EKE), barotropic conversion, and eddy available potential energy (EAPE) to EKE conversion. Holbach and Bourassa (2014) found that the Papagayo and Tehuantepec wind jets (e.g., Chelton et al., 2000) are important for the tropical cyclogenesis process. Recently, Fu et al. (2021) found that Central American gap winds are important for tropical cyclone activity, and also show that easterly wave activity decreases when the gap winds are blocked. Additionally, research into how easterly waves are affected by the Madden-Julian Oscillation (MJO) has been performed (Crosbie and Serra, 2014; Rydbeck and Maloney, 2014, 2015; Whitaker and Maloney, 2018). In particular, Rydbeck and Maloney (2014) and Rydbeck and Maloney (2015) show how the EKE budget and moisture budget of easterly waves, respectively, are altered by phases of the MJO. Finally, studies like Rydbeck and Maloney (2015), Adames and Ming (2018), and Wolding et al. (2020) have shown the importance of moisture in supporting easterly wave disturbances through the link between moisture and convection.

This dissertation will add to this recent body of easterly wave work by examining a case study of the easterly wave genesis pathway discussed in Rydbeck et al. (2017), and by investigating the impact of the Papagayo and Tehuantepec wind jets on the east Pacific mean state, easterly wave tracks, easterly wave composite structure and strength, and the easterly wave EKE budget. Chapter 2 of this work will examine the growth of a Panama Bight MCS into an easterly wave, and has been published in *Journal of the Atmospheric Sciences*. Chapter 3 uses Weather Research and Forecasting (WRF) model simulations to compare changes to the mean state and easterly wave characteristics between a control simulation and a simulation that blocks the Papagayo and Tehuantepec jets. Chapter 4 extends the analysis of Chapter 3 and calculates the easterly wave EKE budget for both simulations. Chapters 3 and 4 are in preparation for submission to an academic journal. Finally, Chapter 5 presents conclusions from this dissertation and discusses future work.

Chapter 2

Genesis of an east Pacific easterly wave from a Panama Bight MCS: A case study analysis from June 2012[1]

2.1 Introduction

Panama Bight mesoscale convective systems (MCSs) are important to the climate and weather of the east Pacific basin. The convective complexes contribute to yearly average rainfall totals ranging from approximately 2600 mm to 5250 mm in the region (Mapes et al., 2003b). Velasco and Fritsch (1987) and Mapes et al. (2003b) found that MCSs and precipitation in the Panama Bight generally occur year-round, but most often during boreal summer. Mapes et al. (2003a) describes a mechanism for MCS propagation away from the Colombian Andes into the Panama Bight, where the initiated convection moves offshore due to a gravity wave response from the elevated heating over land, and eventually becomes more organized into MCS structures during the night and early morning hours (Mapes et al., 2003b). These MCS features were characterized as wide convective cores and broad stratiform regions by Zuluaga and Houze (2015), indicative of mature convection, which can support the development of a mid-level vortex in the disturbance (e.g., Houze, 2004). In addition, the Chocó jet, a westerly wind feature that peaks at 925 hPa and extends across the Panama Bight and onshore plays a role in the heavy precipitation of the region (Poveda and Mesa, 2000). The Chocó jet is supported by the strong SST gradient in the region (e.g., Poveda and Mesa, 2000), with colder water to the south along the South American coast and warmer water to the north in the east Pacific basin and the Panama Bight (Figure 1). The jet supports MCS development by directing low-level moisture into the Panama Bight and toward the Andes (Poveda and

[1]Chapter 2 of this dissertation and the first half of the abstract are published in *Journal of the Atmospheric Sciences*.

Mesa, 2000; Zuluaga and Houze, 2015). Field campaigns like the Organization of Tropical East Pacific Convection (OTREC; https://www.eol.ucar.edu/field_projects/otrec) project in summer 2019 (Fuchs-Stone et al., 2020) and CHOCO-JEX in 2016 (Yepes et al., 2019) aimed to obtain *in situ* observations of the MCSs and Chocó jet to better understand their interactions.

East Pacific easterly waves (EWs) are also essential components of the boreal summer conditions in the basin. EWs in the east Pacific are coupled to convection (e.g., Rydbeck and Maloney, 2015; Adames and Ming, 2018) and are frequently identified as sources of east Pacific tropical cyclogenesis (e.g., Frank, 1970; Molinari and Vollaro, 2000; Dunkerton et al., 2009; Pasch et al., 2009). East Pacific EWs are composed of both deep convective and stratiform elements (Petersen et al., 2003), and have their strongest circulation at mid-levels (Serra et al., 2008, 2010). EWs have periods of around five days and length scales on the order of 4000-5000 km (Serra et al., 2008) and tracks that are near and parallel to the Central American coastline (e.g., Thorncroft and Hodges, 2001; Serra et al., 2010). East Pacific EWs rely primarily on convective invigoration and barotropic conversion for growth (e.g., Maloney and Hartmann, 2001; Rydbeck and Maloney, 2014), and environmental moisture anomalies are crucial for anomalous convection in the wave (Rydbeck and Maloney, 2015). Further, modulations to the background environment of the basin by phenomena such as the Madden-Julian Oscillation (MJO) and Caribbean low-level jet (CLLJ) significantly alter characteristics of the EWs (Maloney and Hartmann, 2001; Crosbie and Serra, 2014; Rydbeck and Maloney, 2014, 2015; Whitaker and Maloney, 2018). For example, anomalous low-level westerly phases of the MJO are associated with stronger waves that are driven more by convective invigoration and have tracks closer to Central America relative to easterly periods (Crosbie and Serra, 2014; Rydbeck and Maloney, 2014, 2015; Whitaker and Maloney, 2018). These enhanced EWs during westerly MJO phases also coincide with a marked increase in tropical cyclone activity in the basin (Maloney and Hartmann, 2000), underscoring the need for further investigations into the lifecycle of east Pacific EWs from EW genesis to development.

Recently, features and processes within the east Pacific region have been suggested as significant sources of EWs (e.g., Mozer and Zehnder, 1996; Ferreira and Schubert, 1997; Serra et al., 2010; Toma and Webster, 2010; Rydbeck et al., 2017), as opposed to African EWs crossing Central America (e.g., Shapiro, 1986; Pasch et al., 2009; Serra et al., 2010). Central American topography can play an important role in local EW genesis, with the mountains perturbing the incoming easterly flow into downstream eddies in idealized simulations (Zehnder, 1991; Mozer and Zehnder, 1996). The CLLJ and the Papagayo jet, an extension of the CLLJ through a gap in the mountains near Costa Rica and Nicaragua, were found at times to have a sign reversal of the meridional potential vorticity gradient near 700 mb in time mean flows over a season from June 15 to September 30, 1991 (Molinari et al., 1997). Due to this sign reversal, Molinari et al. (1997) note that the Charney-Stern necessary condition for instability is met, which allows for synoptic disturbances like EWs to form in the jet regions. Serra et al. (2010) found that EW genesis does in fact occur in the Papagayo jet region, driven by barotropic energy conversions. Tropical cyclogenesis has also been linked to gap flows from the Papagayo jet, as well as the Tehuantepec jet in Mexico (e.g., Holbach and Bourassa, 2014).

Convective development from the east Pacific intertropical convergence zone (ITCZ) and Panama Bight has also been shown to lead to EWs (e.g., Ferreira and Schubert, 1997; Toma and Webster, 2010; Rydbeck et al., 2017). Breakdown of ITCZ convection into EW-like disturbances was simulated in an idealized sense by Ferreira and Schubert (1997), and was cataloged in observations and reanalysis by Wang and Magnusdottir (2006). Near the Panama Bight, Kerns et al. (2008) found that the track density of mid-level vorticity maxima extends to the coasts of Panama and Colombia, and that this region is productive for eventual tropical cyclogenesis—vorticity signatures originating from this area are linked to tropical cyclone formation later on. In a modeling study, Rydbeck et al. (2017) analyzed the transition of Panama Bight MCSs into EWs from a composite perspective using a vorticity budget. In that study, horizontal vorticity advection and vortex stretching were found to be the primary contributors to transform the MCSs into EWs as they moved away from the Bight (Rydbeck et al., 2017). EW development from an initial convective heat source has been simulated over Africa (Thorncroft et al., 2008), and more recently for the Panama Bight (Torres and Thorncroft, 2018) in an idealized primitive equation model.

The purpose of this study is to investigate the Panama Bight MCS to EW growth mechanism in a case study of the EW that led to Hurricane Carlotta (2012). The case will be first analyzed with reanalysis and observational data, before being examined in detail with a regional convective-permitting simulation. The simulation will be used to better understand the role of convective processes in the MCS transition and this impact will be quantified through a vorticity budget. While the reanalysis data used relies on parameterized convection, the model simulation will be able to better resolve convection in the developing disturbance and hence should provide a potentially more realistic picture of the role of convection in this transition. Further, this simulated case will be compared with the composite results for the MCS to EW transition found in Rydbeck et al. (2017). The second section of this paper discusses the data, the modeling setup, and the methodology applied in this study. The third and fourth sections describe the case study and the results of the vorticity budget, respectively. The fifth section investigates possible interactions of the disturbance with low-level wind jets, while the sixth section provides a discussion of the results.

2.2 Data, Model Setup, and Methodology

To select a case of EW genesis from a Panama Bight MCS, the National Hurricane Center's Tropical Cyclone Reports (https://www.nhc.noaa.gov/data/tcr/) and NASA Worldview satellite imagery (https://worldview.earthdata.nasa.gov/) were first used. The disturbance that contributed to the development of Hurricane Carlotta in June 2012 seemed a reasonable instance of this mechanism, as the NHC report states "the genesis of Carlotta can be traced back to an area of disturbed weather that moved westward from Colombia..." (Pasch and Zelinsky, 2012). True Color satellite imagery from NASA Worldview also supports this notion by highlighting a cloud cluster in the Panama Bight on June 11 that expands in size as it moves northwestward and has a reminiscent tilt from the southwest to northeast on June 13 (Figure 2), like previously studied EWs (e.g., Serra et al., 2008).

To investigate the formation of the EW prior to Carlotta, reanalysis, observations and a model simulation are employed and compared. First, the observational and reanalysis investigation of the case consists of data from the new European Center for Medium-Range Weather Forecasts ERA5 reanalysis data (ERA5; Copernicus Climate Change Service (C3S) (2017)) and precipitation data from the NOAA Climate Prediction Center (CPC) morphing method (CMORPH) dataset (CMORPH; Joyce et al. (2004)). The ERA5 data for this analysis consists of 23 vertical levels from 1000 hPa to 200 hPa, a spatial resolution of 0.5°, and a temporal resolution of three hours from 0000 UTC 5 June to 2100 UTC 19 June. Observational sources input to the ERA5 reanalysis include data from satellites, buoys, radiosondes, and aircraft (C3S 2017). The CMORPH precipitation data has a spatial resolution of 0.25° and the same temporal resolution and duration as the ERA5 data.

To simulate the evolution of the MCS into an EW, the Weather Research and Forecasting ARW model, version 3.9.1.1 (WRF; Skamarock et al. (2008)) is used. The model setup and simulation details are displayed in Table 1, and highlight that WRF is run at convective-permitting scales (4 km horizontally, 40 vertical levels) without a cumulus or shallow cumulus parameterization to better represent the convective development of the system in the east Pacific. This model setup contrasts with that of Rydbeck et al. (2017), which investigated MCS to EW transitions in a composite sense over several years in WRF with parameterized convection and an inner domain grid spacing of 18 km. In addition to employing a higher spatial resolution and removing the cumulus parameterization, this study uses the Thompson et al. (2008) microphysics scheme instead of the WRF single-moment six-class scheme, forces and initializes the model with an improved and higher-resolution reanalysis (ERA5), and simulates a single disturbance over a smaller domain. The Thompson et al. (2008) scheme was selected due to its effectiveness in simulating MCS development (K. L. Rasmussen, personal communication) and has been used in higher resolution simulations of MCSs (e.g., Rasmussen and Houze, 2016). Although the Thompson et al. (2008) scheme has been shown to lead to more top-heavy structures and MCS organization (Feng et al., 2018), a sensitivity test with the WRF single-moment six-class microphysics scheme yielded similar results to the Thompson et al. (2008) scheme used in this study. The input data for the simulation is ERA5 data that is three-hourly, has 0.5° horizontal grid spacing, and has 29 pressure levels. ERA5 sea surface temperature data are used at the same temporal and horizontal resolution and are updated every 24 hours. The ERA5 input data are used for the lateral boundary forcing for this single domain, non-nested run and are used to initialize the simulation. Additionally, the simulation begins at 1200 UTC 11 June after the MCS disturbance has formed (e.g. Figure 2) and is run to 0000 UTC 15 June, as we are most interested in the model's representation of the MCS to EW transition as opposed to the initiation of the MCS convection prior to its evolution. To account for potential model spin up time, the analysis of the WRF run begins at 1800 UTC 11 June. Additionally, the reasonable representation of the MCS to EW transition in WRF compared to ERA5 gives confidence to this initialization approach.

For a more direct comparison to the ERA5 and CMORPH data, model output and simulated precipitation rates were degraded to approximate resolutions of 0.5° and 0.25°, respectively, by averaging the higher resolution model data to these grid sizes. Further, for displaying the model data in Hovmöller and plan view formats, a spatial Gaussian filter was used to smooth the data. For the WRF Hovmöller diagram, vorticity anomalies were smoothed using a filter with a standard deviation of σ= 0.5 (corresponding to a filter spatial standard deviation of 0.25° and temporal standard deviation of 1.5 hours), while for all model plan view figures and the ERA5 vorticity in Figures 4 and 11 the contoured fields were smoothed using a filter with a standard deviation of σ = 0.6 (corresponding to a filter spatial standard deviation of 0.3° for the 0.5° resolution data and 0.15° for the 0.25° resolution data). In this study, anomalies are calculated relative to the time mean over each respective time period (ERA5 and CMORPH: 0000 UTC 5 June to 2100 UTC 19 June; WRF: 1200 UTC 11 June to 0000 UTC 15 June). The results of ERA5 anomalies are fairly similar when calculated over the WRF simulation time period. Further, anomalous vertical profiles for the disturbance are calculated by taking the area-average at each pressure level over an approximate 2° $\times$ 2° box centered on the unsmoothed 500 hPa vorticity anomaly maximum, and then subtracting off the respective time mean over that specific region at all levels. Finally, for analyzing the Chocó and Papagayo jets, a time series of the area-averaged 925 hPa horizontal vector wind speed was calculated over the regions (3°N-7°N, 77°W-85°W) and (9°N-13°N, 86°W-89°W), respectively.

The Papagayo jet averaging region is the same region that was defined in Whitaker and Maloney (2018) for a CLLJ index.

2.3 Case Study Overview

The disturbance leading to Hurricane Carlotta in June 2012 highlights the broader implication of the EW genesis mechanism proposed by Rydbeck et al. (2017) (that a Panama Bight MCS can develop into an EW, which then transitions into a tropical cyclone) and is also documented in Pasch and Zelinsky (2012). According to the National Hurricane Center's report on Carlotta (Pasch and Zelinsky, 2012), the disturbance "can be traced back to an area of disturbed weather that moved westward from Colombia to near and just south of Panama on 11 June." In addition, Pasch and Zelinsky (2012) state that "Extrapolation and analyses...suggest that this system was associated with a tropical wave that departed Africa in early June, although this is uncertain since the wave became ill-defined over the central Atlantic." Figure 2 shows the progression of a Panama Bight MCS into Hurricane Carlotta through True Color satellite imagery (human vision-related visible wavelengths) from NASA Worldview. On 10 June, sporadic deep convection is occurring across the east Pacific, while the Panama Bight region is relatively clear. On the next day, a MCS can clearly be identified in the imagery as a circular region of deep clouds, and by 13 June the system has moved to the northwest and transitioned into an EW having a larger area of convection that is oriented from southwest to northeast, reminiscent of the EW structures found by Serra et al. (2008), Rydbeck and Maloney (2014), and others. Carlotta achieved tropical storm and hurricane strength on 0600 UTC 14 June and 1200 UTC 15 June, respectively (Pasch and Zelinsky, 2012), and an eye is visible in the satellite imagery on June 15 (Figure 2). Ultimately, Carlotta is reported to have made landfall near Puerto Escondido, Mexico, and reached its maximum wind speed of 109 mph four hours prior to landfall (Pasch and Zelinsky, 2012). Although this study focuses on the growth of the MCS into an EW, the fact that a landfalling hurricane was produced as a result of this EW further underscores the importance of investigating this pathway to EW genesis.

Figure 3 highlights the progression of the MCS in ERA5 and CMORPH and the WRF simulation through Hovmöller diagrams (averaged from 11°N to 2.5°N) of precipitation rate and anomalous 700 hPa vorticity (relative to each respective time mean). Analyses at 700 hPa have been performed in prior studies to feature EW circulations (Serra et al., 2008, 2010; Rydbeck and Maloney, 2014) and 700 hPa is used to highlight the development of the system from MCS to EW as well as the transition from EW to tropical cyclone. In ERA5 and CMORPH, the MCS feature starting on 1200 UTC 11 June between 80°W and 85°W has rain rates up to 6 mm hr^{-1} that are roughly in phase with the vorticity signature, while at later times starting around 0000 UTC 13 June the EW has lower rain rates and generally higher vorticity. Further, the continuous signal in both CMOPRH precipitation and ERA5 vorticity from around 80°W to 91°W over two days displays the propagation of the disturbance from the Panama Bight at an approximate phase speed of 7 m s^{-1}. An extension of the Hovmöller diagram analysis further back in time and to the east (not shown) reaffirms the findings of Pasch and Zelinsky (2012) that there was not a definitive African EW precursor to this disturbance, and points to this EW likely being formed locally within the east Pacific. The WRF model produces a similar Hovmöller diagram to that of ERA5 and CMORPH and reasonably reproduces the growth of the MCS into an EW. For the simulated MCS, the precipitation is lighter than in observations to the east of 85°W, with maximum values only up to 4 mm hr^{-1}, which may be a consequence of using the Thompson et al. (2008) microphysics scheme. As will be described with Figure 5, a vorticity feature that is tilted from southwest to northeast becomes apparent by 1800 UTC 12 June. This tilted vorticity structure is consistent with the formation of an EW and will be used as the metric for determining EW formation in this study. The approximate longitude of EW genesis is highlighted in Figure 3 and occurs near 86°W to 87°W. The EW feature in WRF has similar precipitation values to the observations. Further, the model produces a slightly more coherent propagation of the vorticity feature in the disturbance when compared to ERA5.

Figures 4 and 5 provide a map of the evolution of 700 hPa vorticity anomalies and precipitation for the disturbance in both observations (Figure 4) and in the WRF simulation (Figure 5). In Figure

4 on 0000 UTC 11 June, the initial convection is beginning to develop along the western coast of Colombia and 12 hours later has moved offshore forming an MCS with CMORPH rain rates over 20 mm hr^{-1}, having similar timing to the diurnal cycle results of Mapes et al. (2003b). For example, Mapes et al. (2003b) found that Panama Bight precipitation maximized around 06 to 08 Local Time in the mean diurnal cycle, which is close to the time (1200 UTC 11 June) that the MCS structure is shown in Figure 4. Between 0000 UTC 12 June and 0000 UTC 13 June the disturbance moves parallel to the Central American coastline and begins transitioning with the development of a broad region of enhanced vorticity. By 0000 UTC 13 June an EW structure of southwest to northeast tilted vorticity has formed at 700 hPa, which has precipitation within and around the disturbance. From 0000 UTC 13 June to 1200 UTC 14 June, the EW disturbance strengthens into tropical storm Carlotta (Pasch and Zelinsky, 2012).

Figure 5 shows that the initialized MCS also grows into an EW in the WRF simulation. The simulated MCS in WRF appears to be weaker than in observations, with generally lower precipitation at 1800 UTC 11 June versus the mature MCS at 1200 UTC 11 June in Figure 4. It is important to note that due to the chaotic nature of convection, we do not necessarily expect the model to perfectly match the observations and reanalysis. Between 0000 UTC 12 June and 0000 UTC 13 June the transition from an MCS into an EW features narrow regions of stronger precipitation that are aligned with the vortex axis, particularly at 0600 UTC (not shown) and 1200 UTC. This behavior is not as apparent in observations and ERA5. The enhanced precipitation co-located with the vorticity feature suggests that deep convection and the resulting stratiform precipitation in WRF could be important to the MCS to EW transition. Rydbeck and Maloney (2015) showed that deep convection is important to EW development, while persistent stratiform precipitation and heating from an MCS can help maintain a mid-level vortex (e.g., Houze, 2004). As will be shown later, vertical profiles of the disturbance suggest strong stratiform support in growing the disturbance. By 1800 UTC 12 June, the 700 hPa vorticity is tilted horizontally from southwest to northeast to form an EW (not shown) and the horizontally tilted structure persists over the next twelve hours as the system strengthens (Figure 5). The simulated disturbance then transitions into a tropical cyclone-like structure by 1200 UTC 14 June, matching the progression shown in Figure 4. These results support the hypothesis for EW genesis via MCS growth proposed by Rydbeck et al. (2017) and highlight the large role that convective processes seem to play in this process in WRF. In summary, the timeline of this process can be broken into three sections: MCS stage up to 0000 UTC 12 June, MCS to EW transition from 0000 UTC to 1800 UTC 12 June, and EW formation at 1800 UTC 12 June with subsequent development.

2.4 Vorticity Budget

To further investigate the development of the MCS into an EW, a vorticity budget at 500 hPa is calculated. This pressure level is chosen to better analyze the transition of the MCS into an EW, as the vortex tends to generally be maximized near 500 hPa during that period (Figures 13 and 14), and to compare against the more generalized results in Rydbeck et al. (2017). Similar to Rydbeck et al. (2017), the vorticity budget equation is given as:

$$\underbrace{\frac{\partial \zeta_z}{\partial t}}_{\text{time tendency}} = \underbrace{-\left(u\frac{\partial \eta}{\partial x} + v\frac{\partial \eta}{\partial y}\right)}_{\text{horizontal advection}} + \underbrace{\eta\frac{\partial \omega}{\partial p}}_{\text{stretching}} + \underbrace{\left[\frac{\partial}{\partial x}\left(-\zeta_u\frac{\omega}{\rho g}\right) + \frac{\partial}{\partial y}\left(-\zeta_v\frac{\omega}{\rho g}\right)\right]}_{\text{tilting}} + \underbrace{R}_{\text{residual}} \tag{2.1}$$

where $\zeta_z = \left(\frac{\partial v}{\partial x} - \frac{\partial u}{\partial y}\right)$ is the vertical vorticity, u is the zonal wind, v is the meridional wind, $\eta = \zeta_z + f$ is the absolute vorticity, ω is the vertical pressure velocity, p is pressure, $\zeta_u = \left(\frac{-1}{\rho g}\frac{\partial \omega}{\partial y} - \frac{\partial v}{\partial p}(-\rho g)\right)$ is the zonal component of vorticity, $\zeta_v = \left(\frac{\partial u}{\partial p}(-\rho g) - \frac{-1}{\rho g}\frac{\partial \omega}{\partial x}\right)$ is the meridional component of vorticity, g is the acceleration due to gravity, and $\rho = \frac{p}{RT}$ is the density of air, with $R = 287Jkg^{-1}K^{-1}$ and T being temperature. The vorticity equation describes the evolution of vertical vorticity that is modulated by the sum of the horizontal advection of vorticity, vortex stretching and tilting, and a budget residual which accounts for factors like friction and turbulent mixing. The budget residual is of the same order of magnitude as the other budget terms, but this analysis will focus primarily on horizontal advection and vortex stretching, the important terms in this process identified by Rydbeck et al. (2017).

2.4.1 WRF

Figures 6, 7, and 8 provide the vorticity budget analysis for the convective-permitting WRF simulation across the MCS to EW transition time period noted in Figure 5. Vorticity budget terms in Figures 6, 7, and 8 are not decomposed into a perturbation and background, with the total field plotted. The total field budget terms closely resemble the time-mean anomalies. For the vorticity budget results, we focus primarily on the WRF simulation as the convective processes in the model should provide a more realistic representation of the role of convection as well as its vertical structure in the MCS to EW transition versus that from ERA5 reanalysis where convective heating is parameterized, which is of particular concern given the data sparseness of the east Pacific. We provide more discussion below about the different realizations of the vertical heating structure in WRF and ERA5 and implications for the vorticity budget. We also acknowledge the chaotic nature of tropical convection in this region, and that even a different realization of the model may produce somewhat different convective evolution and effect on the vorticity budget. However, we are reassured through examination of Figure 3 that the WRF simulation we examine produces a plausible evolution of the vorticity growth of the disturbance given the similarities relative to reanalysis in the vorticity field and relationship to observed precipitation.

Figure 6 shows the 500 hPa vorticity tendency term and vorticity anomaly for the disturbance. During the MCS phase on 1800 UTC 11 June, the vorticity anomaly is fairly circular with strong positive tendency on the western side. Over the next 24 hours, the small disturbance moves northwestward, expands and horizontally tilts. A positive vorticity tendency tends to occur on the leading side with a negative tendency on the trailing side, consistent with propagation. However, a positive vorticity tendency is also often found co-located with the vortex center during these times, implying vortex growth. Overall, a strong positive tendency near the disturbance center as it leaves the coast and a tendency dipole agree with the composite results of (Rydbeck et al., 2017); however, the findings in this study are likely noisier due to the nature of a case study.

Figures 7 and 8 depict the horizontal advection of vorticity and vortex stretching for the simulated disturbance, respectively. For horizontal advection, the pattern of positive (negative) values on the leading (trailing) sides of the system reflect the portion of the tendency in Figure 6 that are consistent with propagation, especially at the EW stage. While Rydbeck et al. (2017) found that the initial mesoscale vortex expands in the composite over many events due to differences in horizontal advection on either side of the system, with horizontal advection contributing to vortex growth, this process does not appear as prominent in the model simulation for this single case. For example, Rydbeck et al. (2017) show strong positive horizontal advection leading the mid-level vorticity anomaly that is larger in absolute value than the trailing negative advection. In this case study, the leading positive horizontal advection seems to be similar in absolute value, or even weaker than, the trailing negative advection feature (Figure 7). However, vortex stretching associated with convective activity appears to have a consistent impact on vortex growth in our case study (Figure 8). A positive stretching tendency first occurs within the initial MCS feature on 1800 UTC 11 June allowing the vortex to intensify. During the transition period from 0000 UTC to 1800 UTC 12 June, a strong positive stretching feature occurs within the vorticity anomaly and on the southwest and northeast sides of the system. This promotes wave tilting and eddy kinetic energy growth by eddy-mean flow interactions in a region of background cyclonic shear of the mean zonal wind (Rydbeck and Maloney, 2015). To this end, positive stretching in these regions will support an expansion of the vortex to the southwest and northeast, generating a horizontal tilt. Further, a cyclonic wave tilted from southwest to northeast in a favorable mean cyclonic shear environment will acquire eddy kinetic energy through barotropic energy conversions (e.g., Maloney and Hartmann, 2001; Serra et al., 2010). Thus, this result supports the findings of Figure 5 that a strong coupling between convective processes and the vortex in the model aids EW genesis from the MCS, and is further highlighted by the elevated rain rates in Figure 5 being co-located with regions of strong vortex stretching in Figure 8, particularly at 1800 UTC 11 June and 0600 UTC, 1200 UTC 12 June and vertical Q1 profiles of the system center indicative of convective activity (not shown). Further, the locations of strong stretching within and at the flanks of the vortex center are consistent with the composite results of Rydbeck et al. (2017) that stretching contributes to the strengthening and expansion of the system, especially considering that the simulation is run at convective-permitting scales. Finally, while vortex tilting in the simulation weakly supports MCS intensification in the initial stages and also produces positive vorticity tendency on the leading side of the system in its development, tilting does not seem to play as large of a role in the MCS transition to an EW compared to stretching (not shown).

2.4.2 Vertical Profiles

In addition to the 500 hPa plan view snapshots of the vorticity budget, anomalous area-averaged vertical profiles of the budget terms were calculated for the MCS to EW transition in WRF (Figure 9). The vertical profile anomalies for the disturbance are calculated via a Lagrangian analysis by taking the area average at each vertical level across a $2^\circ \times 2^\circ$ box centered on the unsmoothed 500 hPa vorticity anomaly maximum for the disturbance at a given time and location, and then subtracting away the area-averaged time mean of the same current box location. The track of this vorticity maximum is shown in Figure 1. By removing the model basic state, the profiles will focus on the development of the perturbation vortex. When analyzing the full variable fields to include the background state, the WRF budget term profiles are similar to those for the perturbation vortex (not shown).

Figure 9 shows that vortex intensification during the MCS to EW transition is dominated by stretching between 800 hPa and 400 hPa. Each vertical profile except for 1800 UTC 11 June has a positive maximum in stretching near 600 hPa and the three highest values of stretching occur toward the end of the transition to an EW at 0600 UTC, 1200 UTC, and 1800 UTC 12 June. An analysis of the stretching term, $\eta\frac{\partial\omega}{\partial p} = \zeta_z\frac{\partial\omega}{\partial p} + f\frac{\partial\omega}{\partial p}$, indicates that the term with ζ_z is the dominant contributor to stretching when compared to the Coriolis parameter (not shown). Further, the ζ_z contributions to the stretching profiles in Figure 9 are largely composed of vorticity from the EW anomaly or convection acting within the mesoscale vortex, rather than from the background vorticity (not shown). The shape of the stretching profiles suggests a top-heavy convective structure to the system where anomalous convergence is occurring in the middle troposphere, which is conducive to forming a mid-level vortex (e.g., Houze, 2004) and is supported by Figure 13. The top-heavy structure of the disturbance was also observed in a 2° × 2° full-field analysis to incorporate the background state (not shown). Rydbeck et al. (2017) also identified that a top-heavy heating structure was present in their analysis. On the other hand, horizontal advection is generally weak or negative during the MCS to EW transition and is strongly negative after an EW has formed in the final two profiles. Vortex tilting does not seem to play as large of a role in vortex development as the other two terms but does positively contribute to growth at lower levels at 1200 UTC and 1800 UTC 12 June, possibly associated with shearing effects due to the Papagayo jet. Overall, vertical profiles of the budget terms point to the importance of convective coupling and a top-heavy structure in the EW genesis pathway for vorticity generation in this case study, as also seen in Figures 5 and 8.

Vorticity budget results for ERA5 (not shown) are generally similar to those presented for WRF in Figures 6-9; however, there are a few notable differences. First, the MCS vortex in ERA5 seems to expand early on through horizontal advection and has negative stretching at 500 hPa during these times, which is not seen in WRF. Like in WRF, stretching is very important to the MCS to EW transition in ERA5, but stretching tends to have a more consistent impact on MCS upscale growth in the model than in observations. In terms of the budget vertical profiles, stretching in ERA5 tends to peak slightly higher in the middle troposphere than in the WRF, but there is also evidence of strong low-level stretching at 0000 UTC 13 June in ERA5 that does not occur in the model. This later signal has implications for interactions with wind jets, which maximize at low levels in this region. One interesting caveat to the WRF results in Figure 9 is that when the box was expanded for a 5° × 5° full-field analysis (not shown), there was an increase in low-level stretching and low-level heating, while still maintaining strong mid-level stretching and top-heaviness. This suggests the possibility of jet interactions and/or deep convection in WRF further away from the mid-level vortex and highlights some modest sensitivity of the results to the box size.

2.5 Potential Interactions with Low-Level Wind Jets

The Chocó and Papagayo low-level jets have been shown to be important in the development of MCSs, EWs, and tropical cyclones (Serra et al., 2010; Holbach and Bourassa, 2014; Zuluaga and Houze, 2015). This section will investigate the behavior of these wind jets over the course of this case study, and test the hypothesis that the Papagayo jet, in particular, helps strengthen the developing MCS.

Figure 10 gives time series of the westerly Chocó and easterly Papagayo jet features in both ERA5 and the WRF simulation. As discussed above, the Chocó jet is defined as the average horizontal vector wind speed at 925 hPa over 3°N-7°N, 77°W-85°W, while the 925 hPa Papagayo jet wind speed is averaged over the same area that was used in Whitaker and Maloney (2018, 9°N-13°N; 86°W-89°W). In ERA5, both the Papagayo and Chocó jets are relatively weak six to three days before the mature MCS on 1200 UTC 11 June, having wind speeds below 6 m s^{-1}. Over the following couple of days, the Papagayo jet strengthens to over 8 m s^{-1} on 0000 UTC 10 June and then weakens over the next 24 hours. Meanwhile, the Chocó jet strengthens by roughly 4 m s^{-1} over 24 hours starting on 1200 UTC 10 June and then maximizes to a wind speed of 6 m s^{-1} at 1200 UTC 11 June, when the MCS has formed over the Panama Bight and when the WRF simulation begins. The Papagayo jet begins to greatly intensify as the MCS convection develops, starting around 0000 UTC 11 June. By the time the MCS has formed 12 hours later, the jet wind speed is up to around 10 m s^{-1}.

Looking at times following the WRF simulation start time, both ERA5 and WRF show that the Chocó jet steadily weakens as the MCS disturbance propagates away from the South American coast. However, the Papagayo jet continues to strengthen during the MCS to EW transition (which occurs between 0000 UTC to 1800 UTC 12 June) while the disturbance moves to the northwest toward Costa Rica and the jet region. In both reanalysis and the model, the Papagayo jet intensifies by about 4 m s^{-1} from 1200 UTC 11 June to 1200 UTC 12 June and maximizes around 14 m s^{-1}. In fact, looking from the time of initial MCS convective activity on 0000 UTC 11 June, ERA5 documents an almost 8 m s^{-1} increase in the jet to its maximum strength a day and a half later.

In the hours after peak jet strength, the disturbance completes its transition into an EW and the jet weakens. Finally, as the EW continues propagating to the northwest and eventually forms Carlotta, ERA5 and WRF show that the strength of the Papagayo jet greatly tapers off.

Figure 11 shows the evolution of 925 hPa geopotential height (with the average diurnal cycle removed), 925 hPa vorticity anomalies (relative to the 0000 UTC 5 June - 2100 UTC 19 June time mean), and the total unfiltered 925 hPa wind during the MCS to EW transition in ERA5. In the first two panels on 10 June, the weakness of the easterly Papagayo jet is evident, even though the broader Caribbean low-level jet can be observed further to the east. Further, the Chocó jet begins to set up on June 10 with westerly flow occurring around 5°N by 2100 UTC, and an increase in jet strength highlighted in Figure 10. Over the next 24 hours during June 11, the initiated MCS convection seen in Figure 2 becomes apparent in the geopotential height anomalies, with low pressure and stronger westerlies in the Panama Bight. Additionally, the Papagayo jet is more prominent by 2100 UTC 11 June, with the lower level vorticity feature extending out from the Central American coast and a stronger meridional pressure gradient associated with the strong high pressure anomalies to the north on the Caribbean side of Central America and the weak low pressure anomalies in the east Pacific. A pressure gradient across the Central American terrain has been shown to lead to an intensification of gap wind features (Schultz et al., 1997), while a fluctuation of the trade winds may also be supporting the Papagayo jet (Chelton et al., 2000). During the MCS to EW transition from 0000 UTC to 1800 UTC 12 June, the Papagayo jet reaches its maximum strength over the case study region and is accompanied by enhanced low-level vorticity. On 0900 UTC 12 June, the transitioning disturbance is still to the southeast of the jet and the low-level vorticity anomaly; a broad low pressure anomaly that is likely aided by the MCS continues to support the overall pressure gradient across the Papagayo gap. On 2100 UTC 12 June, an elongated 925 hPa vorticity feature extends to the southwest from the coastline and the recently formed EW vorticity feature is starting to become almost co-located with it (not shown). Thus, the low pressure anomaly of the MCS during its evolution appears to have aided a broader pressure gradient that was set up by the Caribbean high pressure anomalies, and this pressure gradient likely forced the enhanced Papagayo gap flow. This enhanced easterly gap flow, coupled with the monsoon trough westerlies produced positive low-level shear vorticity on the equatorward side of the jet for the system to interact with, as described in Holbach and Bourassa (2014). Holbach and Bourassa (2014) also found that surface vorticity generated by the Papagayo jet supports TC genesis.

Figure 12 shows the 925 hPa evolution of the wind jets and geopotential height (with the average diurnal cycle removed) in WRF. Early on during the MCS stage, the Chocó jet is apparent, directing westerly flow toward the disturbance. During the MCS to EW transition from 0000 UTC to 1800 UTC on 12 June, the Papagayo jet undergoes a similar progression as in ERA5 (Figure 11), with positive shear vorticity being generated to the south of the jet. This low-level vorticity feature is out in front of the mid-level vortex highlighted in Figures 1 and 6-8, possibly limiting its interaction with the core of the disturbance and differing from the near co-location noted for ERA5 above. So, while WRF and ERA5 have similar jet structures and evolutions, differences in vertical profiles between the cases may be important to potential interations, as will be discussed next.

Figures 13 and 14 show vertical profiles of the centered, area-averaged anomalies of ω and vorticity for the disturbance across a $2^{\circ} \times 2^{\circ}$ region in WRF and ERA5, respectively. Figure 13 shows that the developing disturbance in WRF generally has upward vertical motion at upper levels and downward motion at lower levels, indicative of a stratiform structure. In particular, this anomalous top-heavy structure is supported by a full-field analysis of omega and Q1 (apparent heat source) that shows that the overall structure of the disturbance including the background state is also top-heavy (not shown). Coupled with this structure is a consistent vorticity profile that peaks at mid-levels. Although the mid-level vortex intensifies over the course of the MCS to EW transition, there does not seem to be a strong increase in anomalous low-level vorticity across the profiles, which suggests that interactions with the Papagayo jet during this time do not produce a positive vorticity tendency beneath the mid-level center, and is consistent with a vertical velocity structure that suggests anomalous divergence in the lower troposphere. Figure 9 also supports this notion, with positive stretching mostly being confined to mid-levels. Although there is some evidence of positive tilting at the level of the jet (Figure 9), a low-level spin up due to the jet is not reflected in the WRF vorticity profiles (Figure 13). An analysis of the stretching term points to the vertical relative vorticity of the vortex itself being more important to intensification when compared to the environmental vorticity (not shown). So, the stratiform structure of the disturbance is persistent throughout the transition into an EW in WRF.

In reanalysis, Figure 14 shows that vertical velocity profiles are generally not as top-heavy as in WRF. This feature also holds for a full-field $2^\circ \times 2^\circ$ analysis of omega and Q1 that includes the background state, suggesting overall stronger low-level vertical motion in ERA5 versus WRF (not shown). Low-level convergence is suggested from the anomalous vertical velocity profiles in ERA5 for several of the times, suggesting positive vorticity generation at low-levels. During the final two profiles, the low-level vorticity increases, indicating that the system may be interacting with the low-level vorticity anomaly associated with the Papagayo jet shown in Figure 11. This interaction with the jet comes around the time the EW has formed, and thus may be more important to the development of the EW rather than the transition of the MCS. So, while the disturbance in WRF is more top-heavy with a mid-level vortex, the reduced top-heaviness of the ERA5 disturbance along with the timing of the mid-level vortex may be allowing for stronger interactions with the Papagayo jet. Interestingly, both sets of anomalous omega profiles suggest that as the system develops, the profiles become less top-heavy near the vortex center, which could be due to the system transitioning into an EW from an MCS. In EWs, deep convection plays a more important role in supporting the disturbance and is maintained by moisture advection from the EW circulation (Rydbeck and Maloney, 2015). Again, there is some sensitivity to the size of the averaging box used. For example, in WRF a $5^\circ \times 5^\circ$ full-field analysis finds that stronger low-level upward vertical motion and enhanced low-level vorticity occur in the vertical profiles, although the Q1 and omega profiles are still top-heavy. This highlights some sensitivity to these findings and indicates that potential jet interactions and deep convection could be occurring further away from the mid-level vortex center. On the other hand, the anomalous profiles for the perturbation vortex at the

$5^\circ \times 5^\circ$ box size do not show much low-level vertical motion and have some increased low-level vorticity (not shown).

For the same disturbance, ERA5 and WRF have differing vertical motion profiles near the maximum of the mid-level vortex. These differences have important implications, such as the model supporting a mid-level vortex through a primarily stratiform structure and ERA5 providing opportunities for convection and vorticity generation at lower levels. In addition, the shape of the vertical motion profiles in the disturbance are important to understanding interactions with the Papagayo jet, where shear vorticity has been generated to the south of the jet (Holbach and Bourassa, 2014). Low-level upward motion in the vicinity of the jet shear vorticity anomaly would lead to additional vorticity generation there. Thus, field observations like those collected during OTREC (e.g., Fuchs-Stone et al., 2020) will be important to improving our understanding of the vertical structure of east Pacific disturbances and their representation in models and reanalyses. What east Pacific vertical convective structure looks like was one of the primary motivations for OTREC. Given the parameterized nature of convection in ERA5 and the relatively data poor east Pacific, we are not confident that vorticity budget processes are necessarily better represented in ERA5 versus the model that has higher resolved convective processes and improved representation of the complex topography of this region.

2.6 Discussion

The formation of east Pacific EWs encompasses an array of remote and local factors. While a traditional view is that east Pacific EWs are simply African EWs that have entered the basin (e.g., Frank, 1970; Pasch et al., 2009), other studies have proposed several mechanisms for EW genesis in the basin without a precursor wave (e.g., Ferreira and Schubert, 1997; Toma and Webster, 2010; Rydbeck et al., 2017). One such mechanism is the upscale growth of Panama Bight MCSs, investigated in a modeling study by Rydbeck et al. (2017). The present study reaffirms this type of EW genesis by providing a case study of this process, and analyzes an MCS to EW transition that occurred on 11-12 June 2012 with a WRF simulation at convective-permitting scales.

Echoing the findings of Kerns et al. (2008) and Rydbeck et al. (2017), the Panama Bight MCS vortex was able to grow as it moved northwestward, with vortex stretching being a key aspect of the process. Vortex stretching associated with convective processes, and top-heavy structures in particular, is the driver of the MCS transition into an EW, supporting Rydbeck et al. (2017), while horizontal advection is associated with the propagation of the system with positive advection leading the advancing vortex and negative advection trailing it. Positive vortex stretching regions occur within and on the southwest and northeast portions of the system vorticity anomaly, which allows the smaller MCS vortex to intensify, expand, and tilt its wave axis, assisting the transition into a structure resembling an EW. Rydbeck and Maloney (2015) show that convection in the southwest and northeast regions of an EW supports the tilting of a wave and leads to continued wave growth.

Anomalous vertical profiles of stretching, vertical motion, and relative vorticity near the mid-level vortex maximum highlight that the MCS growth process in this case seems to be primarily associated with stratiform structures. Positive stretching occurs at mid-levels, which acts on and subsequently strengthens a mid-level vortex. In the WRF simulation, Figure 13 shows that the peak vorticity at the EW stage (the final profile) is almost double that of the peak vorticity at the MCS stage (the first profile). Figure 5 highlights that precipitation is fairly co-located with the developing vortex, and combined with the findings of a consistent top-heavy structure and strong mid-level stretching, precipitation processes seem to have a strong influence on the growth of the disturbance.

In addition to conducting a vorticity budget on the developing MCS, the possible interactions of low-level wind jets with the growth process were investigated. Similar to the findings of Zuluaga and Houze (2015), a strong Chocó jet is present as the MCS forms, with the horizontal vector wind speed increasing by 4 m s^{-1} in ERA5 from 1200 UTC 10 June to 1200 UTC 11 June in the build up to the MCS forming (Figure 10). In addition, Figure 10 shows that the Papagayo jet reaches its peak intensity around one day after the MCS has formed, both in observations and in the model. Figures 13 and 14 emphasize that the disturbance in WRF is more top-heavy than in ERA5 and that the ERA5 disturbance has an increase in low-level vorticity during the later anomalous profiles, while the vorticity in the simulated system remains concentrated at mid-levels. In light of the less top-heavy vertical motion profiles, implied low-level convergence, and the increase in low-level vorticity, there is evidence of stronger possible interactions with the Papagayo jet in ERA5 near the location of the mid-level vorticity maximum. Field observations from OTREC will be useful for better understanding the shape and variability of vertical motion profiles of developing disturbances as well as investigating interactions with the Papagayo and Chocó jets. For example, (Fuchs-Stone et al., 2020) found that bottom-heavy profiles generally occurred during OTREC, which provides support to ERA5's interactions with the Papagayo jet as reflected in the ERA5 results and serves as a caveat to WRF, although these events occured over different time periods. Further modeling that spans a larger number of EW development cases will also help to address this issue. A caveat to these results is the selection of averaging box size. While a smaller box size focuses on the development of the primary mid-level vortex, a larger box size could useful in examining more exterior impacts on the disturbance. While the results in this study highlight a strong stratiform profile in the WRF system, an analysis with a larger box size suggests that deep convection as well as interactions with the Papagayo jet could be relatively more prominent further from the mid-level center.

While this case study gives additional context to the MCS to EW mechanism proposed by Rydbeck et al. (2017), many questions still remain, for example: How often does this process occur in a given hurricane season? Why do some Panama Bight MCSs develop into EWs and not others? Can we improve our forecasts of EWs and possibly even hurricanes by knowing more about this process? To this end, additional studies of this process, which will be aided by observations gathered during the OTREC field campaign in summer 2019, are necessary to improve our understanding of east Pacific EW activity.

Table 2.1: WRF model and simulation setup

Model	WRF-ARW V3.9.1.1; (Skamarock et al. (2008))
Domain	2-14°N; 100-74°W
Simulation dates	1200 UTC 11 June 2012 to 0000 UTC 15 June 2012
Input interval	10800 seconds; input data from ERA5 (0.5°)
Time step	30 seconds
Resolution	4 km (horizontal); 40 vertical levels
Cumulus parameterization	none
Microphysics	Thompson; (Thompson et al. (2008))
Radiation	CAM; (Collins et al. (2004))
Land surface model	Noah; (Tewari et al. (2004))
PBL scheme	YSU; (Hong et al. (2006))

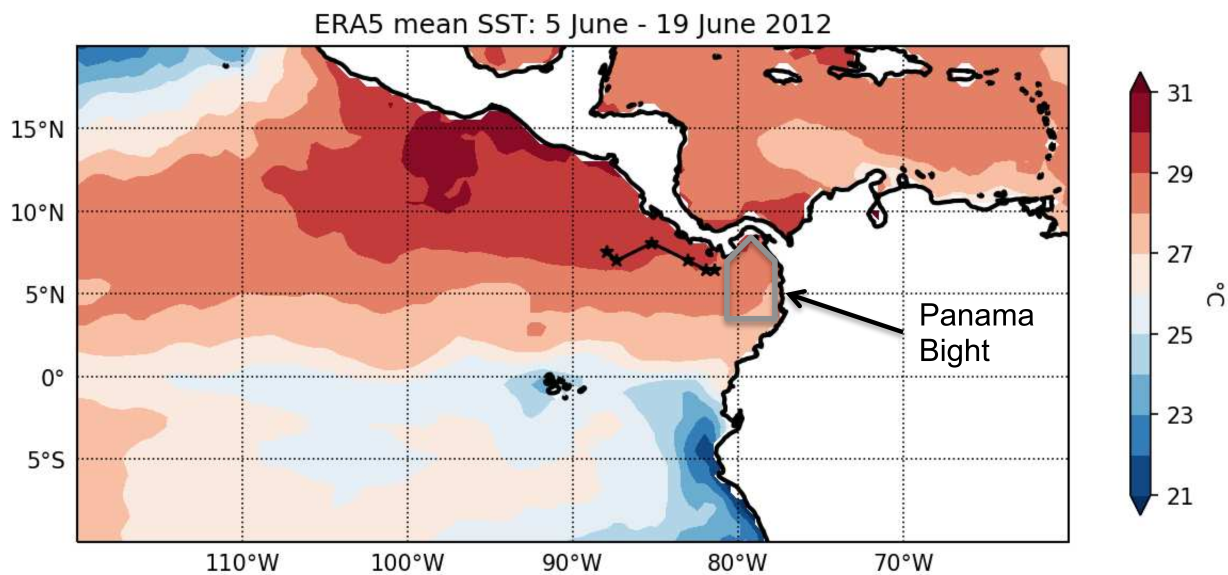

Figure 2.1: ERA5 mean SST from 0000 UTC 5 June to 2100 UTC 19 June 2012 (Celsius, color contours), WRF 500 hPa unsmoothed vorticity maximum track for the vertical profile analysis (black stars), and approximate region considered the "Panama Bight" in this study (gray region). Black stars from east to west correspond to the location of the WRF disturbance at 1800 UTC 11 June, 0000 UTC 12 June, 0600 UTC 12 June, 1200 UTC 12 June, 1800 UTC 12 June, and 0000 UTC 13 June, respectively.

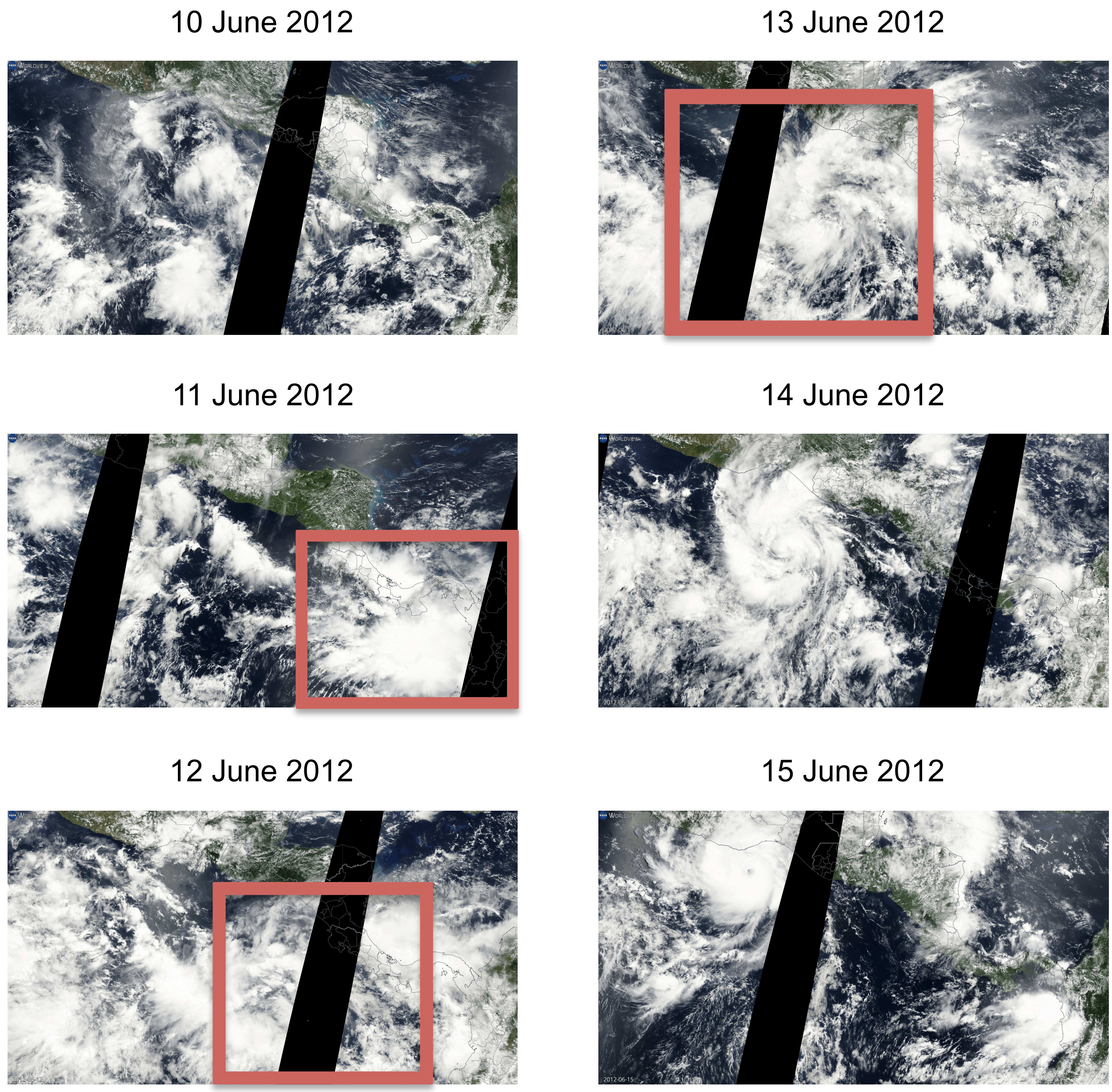

Figure 2.2: Terra/MODIS True Color imagery of the development of Hurricane Carlotta (10-15 June 2012). Red boxes indicate the region of the developing disturbance. Imagery was taken from NASA Worldview.

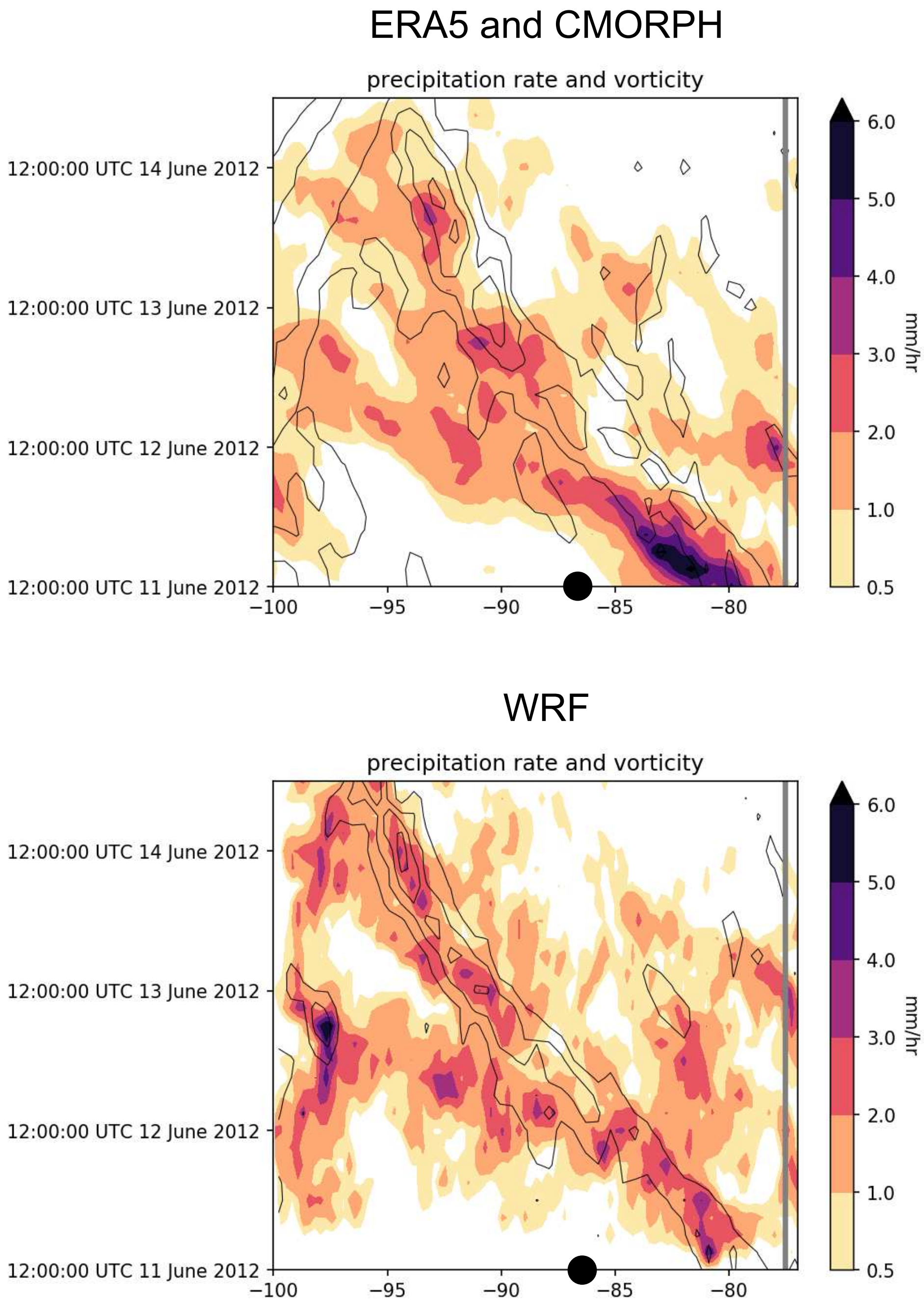

Figure 2.3: Hovmöller diagrams of precipitation rate (mm hr^{-1}; color contours) and anomalous 700 hPa relative vorticity (s^{-1}; line contours, 1×10^{-5} s^{-1} to 7×10^{-5} s^{-1} by 2×10^{-5} s^{-1}) for ERA5 and CMORPH (top) and the WRF simulation (bottom). Data is averaged from 11°N to 2.5°N, and the gray vertical line at 77.5°W represents the Pacific coast of South America. The black dots on the longitude axis represent the approximate longitude of the vorticity disturbance at the time of easterly wave genesis (1800 UTC 12 June 2012).

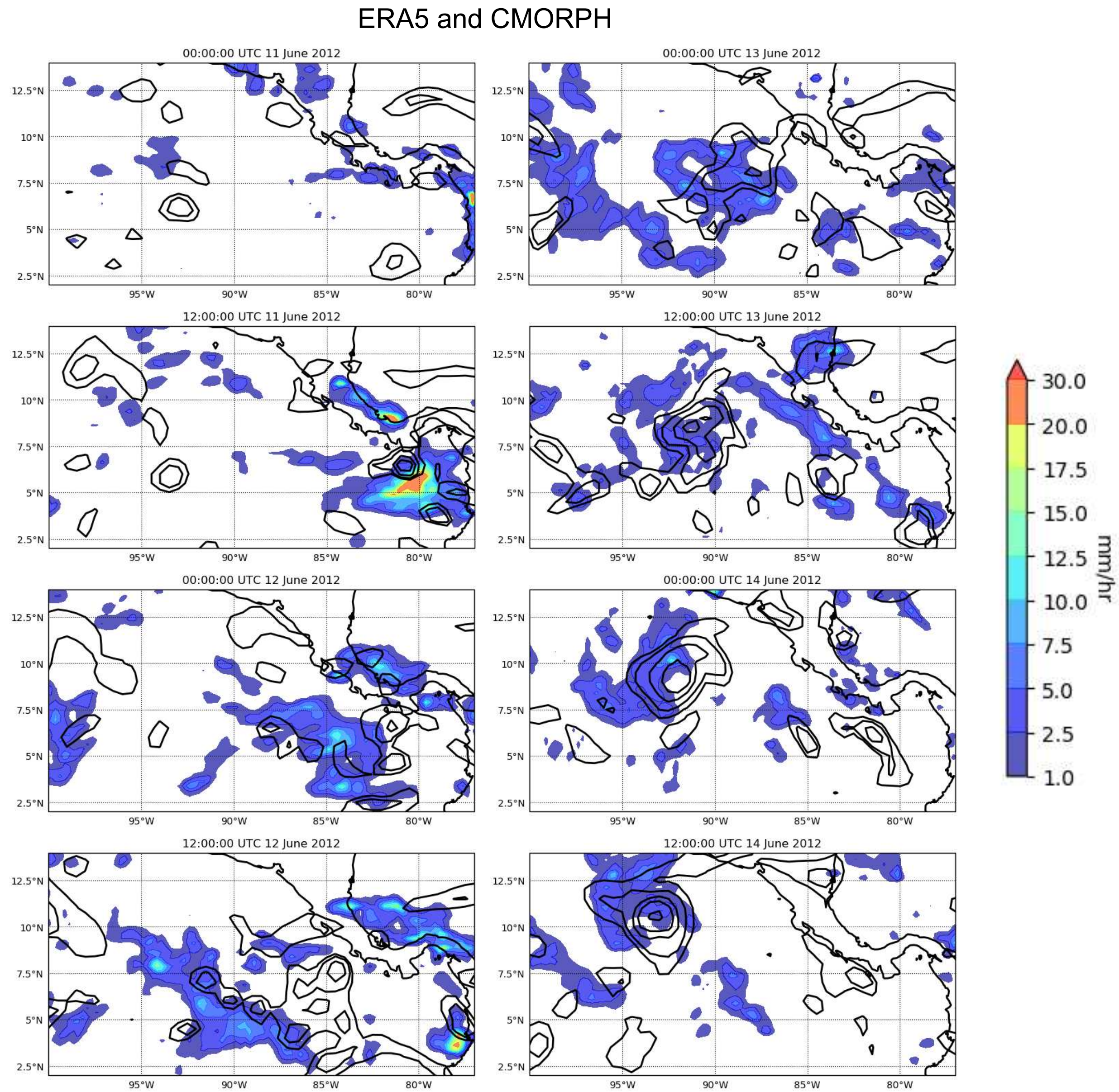

Figure 2.4: ERA5 700 hPa relative vorticity anomalies (s^{-1}; line contours) and CMORPH precipitation rate (mm hr^{-1}; color contours) for the developing disturbance. Vorticity contour interval is: 2.5, 5, 10, 15, 25, 45, 65×10^{-5} s^{-1}.

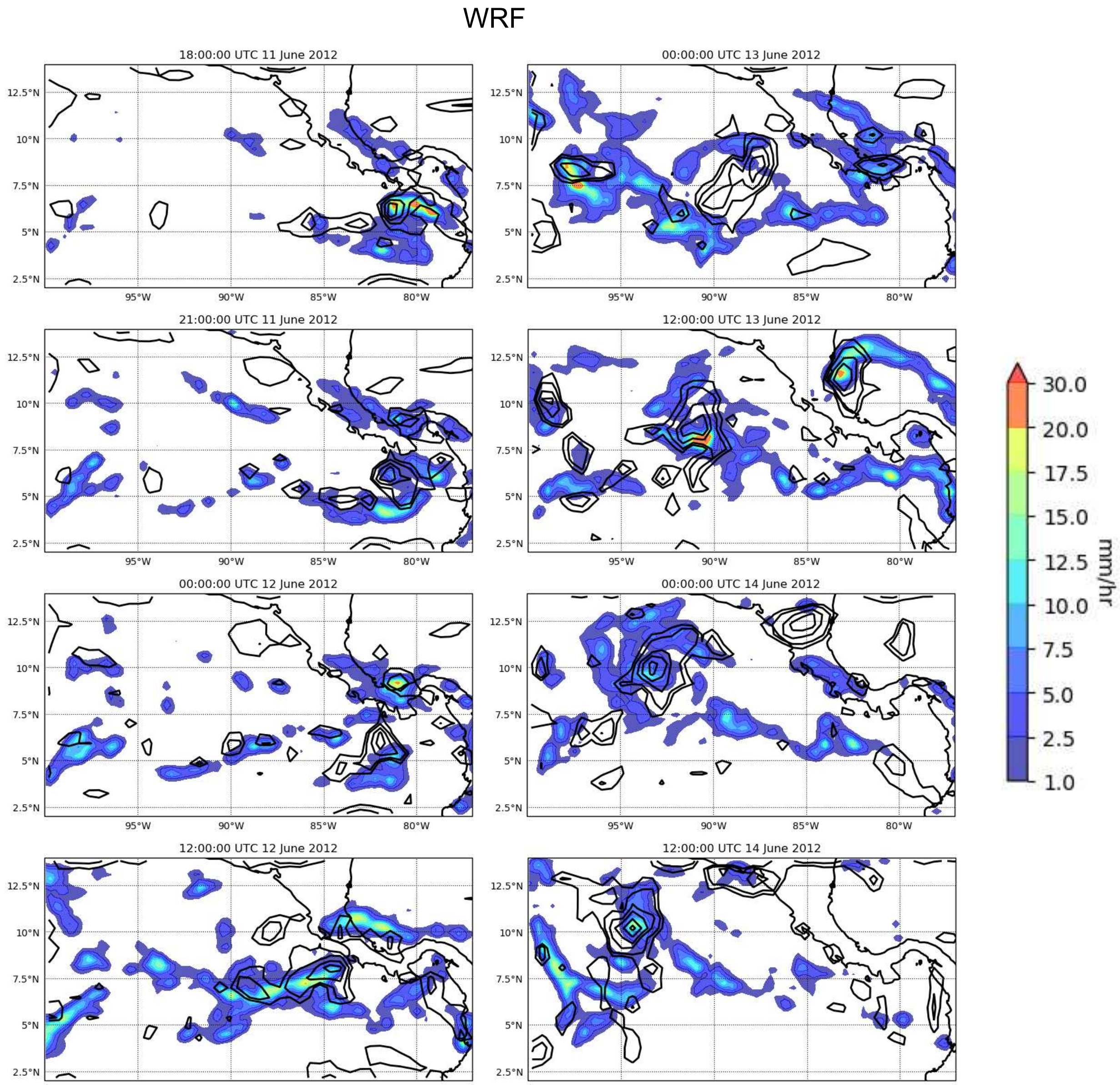

Figure 2.5: WRF 700 hPa relative vorticity anomalies (s^{-1}; line contours) and precipitation rate (mm hr^{-1}; color contours) for the developing disturbance. Vorticity contour interval is: 2.5, 5, 10, 15, 25, 45, 65×10^{-5} s^{-1}.

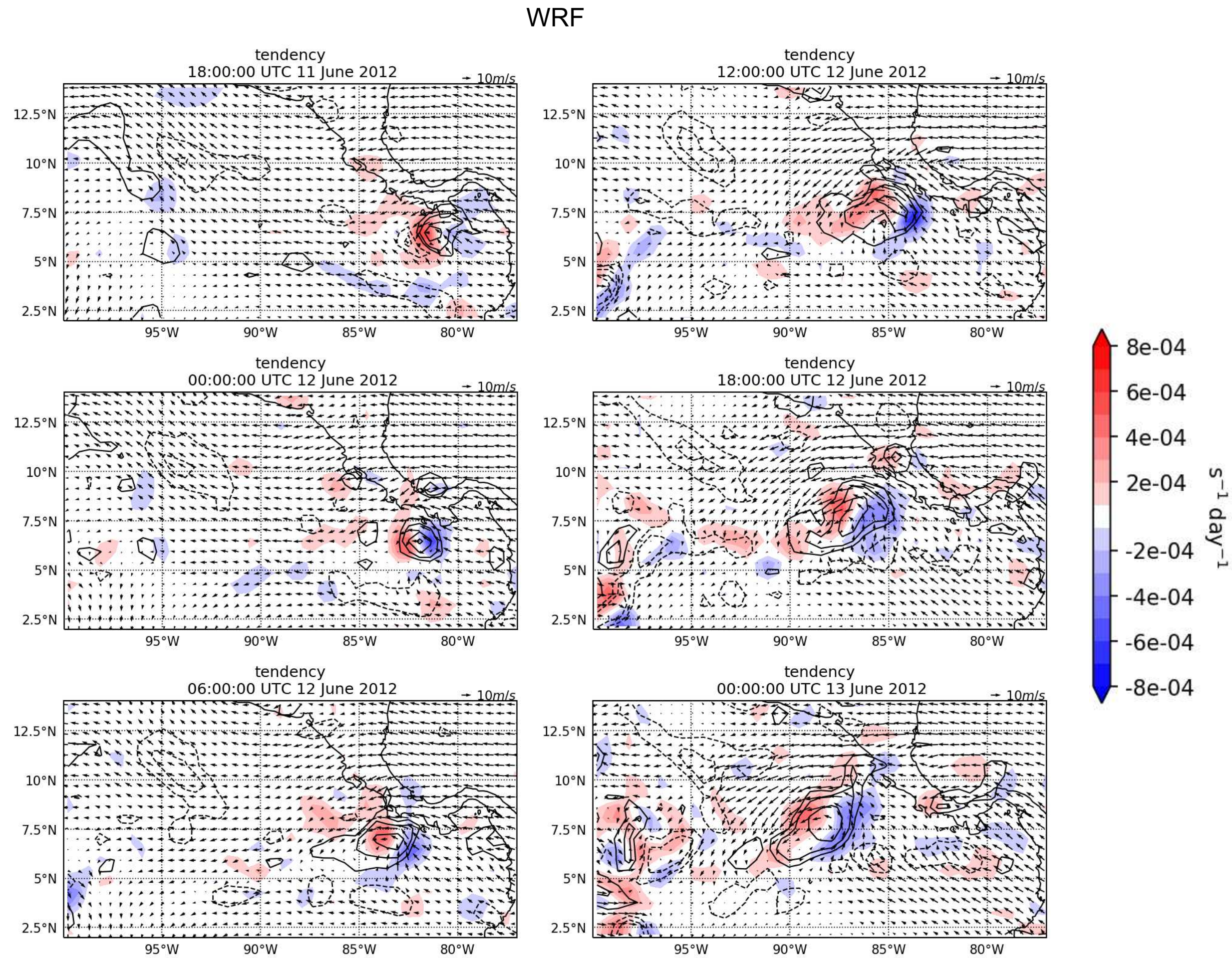

Figure 2.6: WRF total 500 hPa vorticity time tendency (s^{-1} day^{-1}; color contours), anomalous 500 hPa relative vorticity (s^{-1}; line contours), and total 500 hPa wind (m s^{-1}; vectors, reference vector of 10 m s^{-1}). Relative vorticity contour interval is: $\pm$ 2.5, 5, 10, 15, 25, 45, 65$\times 10^{-5}$ s^{-1}.

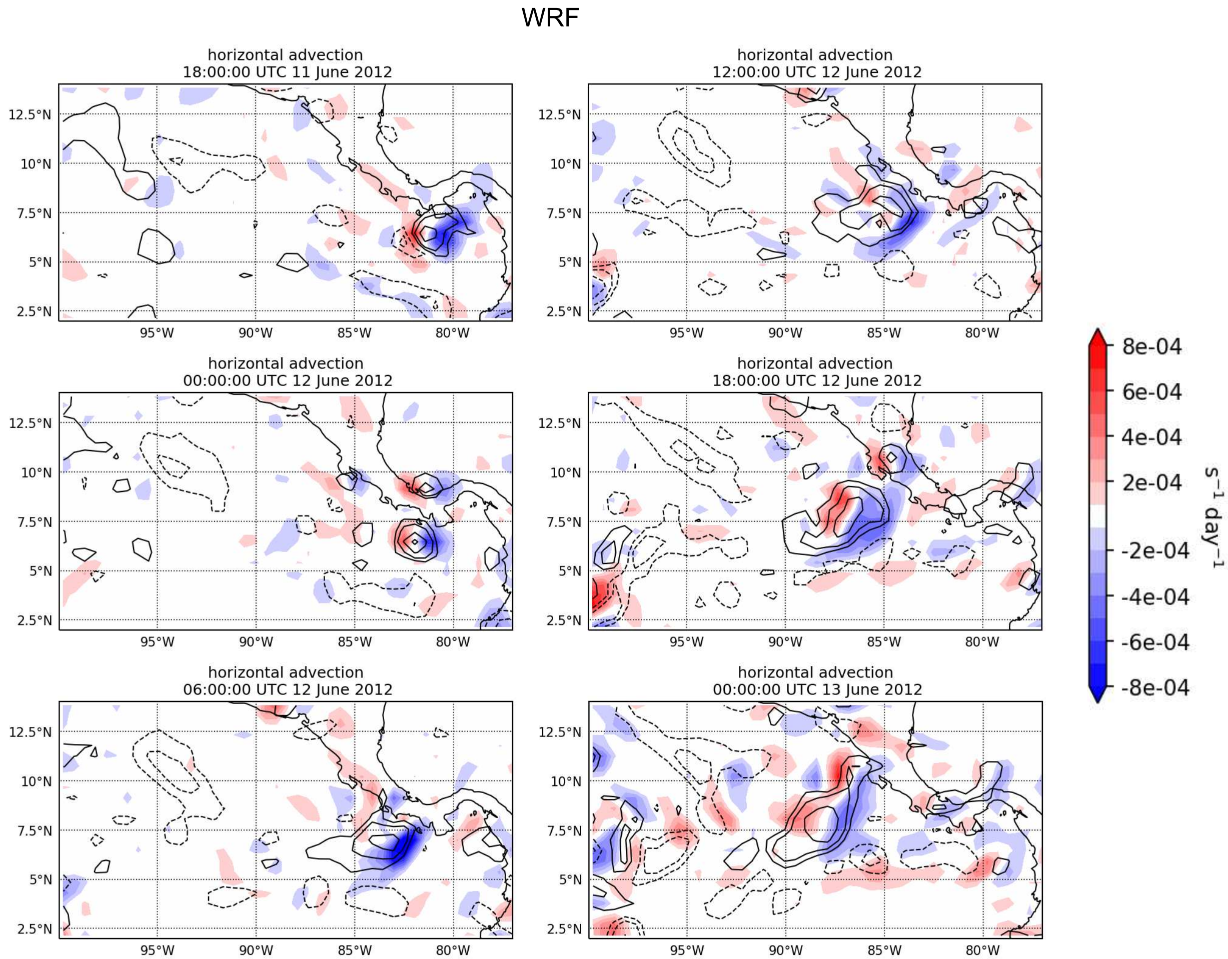

Figure 2.7: WRF total 500 hPa horizontal advection of vorticity (s^{-1} day^{-1}; color contours) and anomalous 500 hPa relative vorticity (s^{-1}; line contours). Relative vorticity contour interval is: $\pm$ 2.5, 5, 10, 15, 25, 45, 65×10^{-5} s^{-1}.

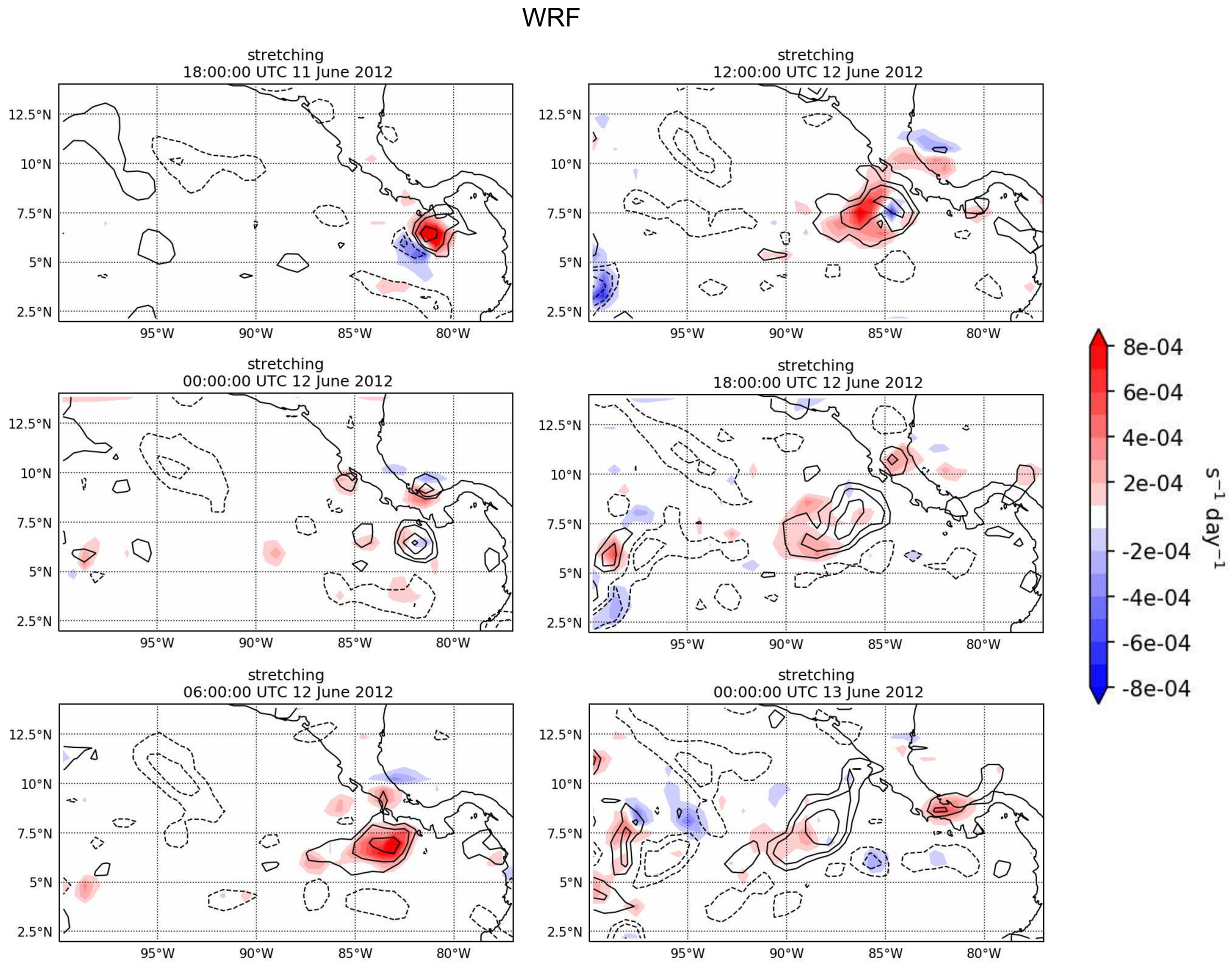

Figure 2.8: WRF total 500 hPa vorticity stretching (s^{-1} day^{-1}; color contours) and anomalous 500 hPa relative vorticity (s^{-1}; line contours). Relative vorticity contour interval is: $\pm$ 2.5, 5, 10, 15, 25, 45, 65×10^{-5} s^{-1}.

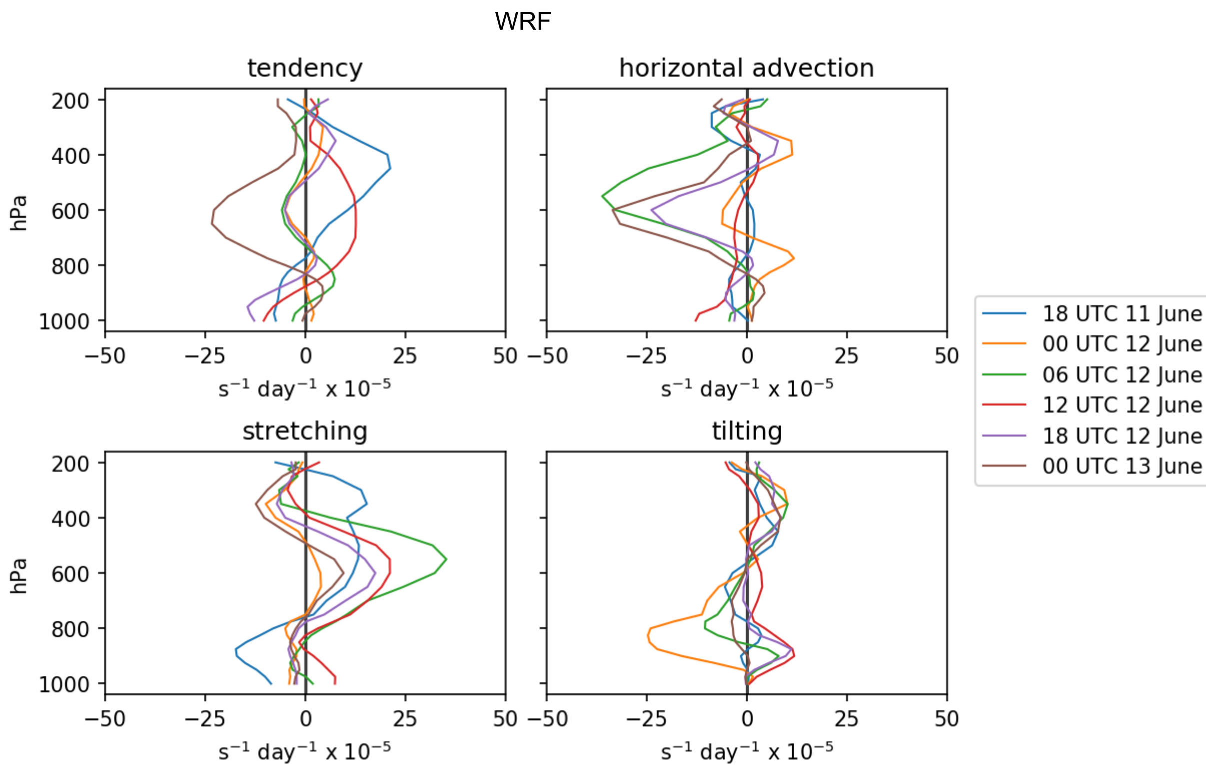

Figure 2.9: Vertical profiles of average WRF vorticity budget term anomalies (s^{-1} day^{-1} $\times 10^{-5}$) across an approximate $2^{\circ} \times 2^{\circ}$ box centered on the 500 hPa vorticity maximum of the disturbance every six hours starting at 1800 UTC 11 June 2012. Anomalies are relative to the time mean for the full simulation (1200 UTC 11 June 2012 to 0000 UTC 15 June 2012) over each respective box.

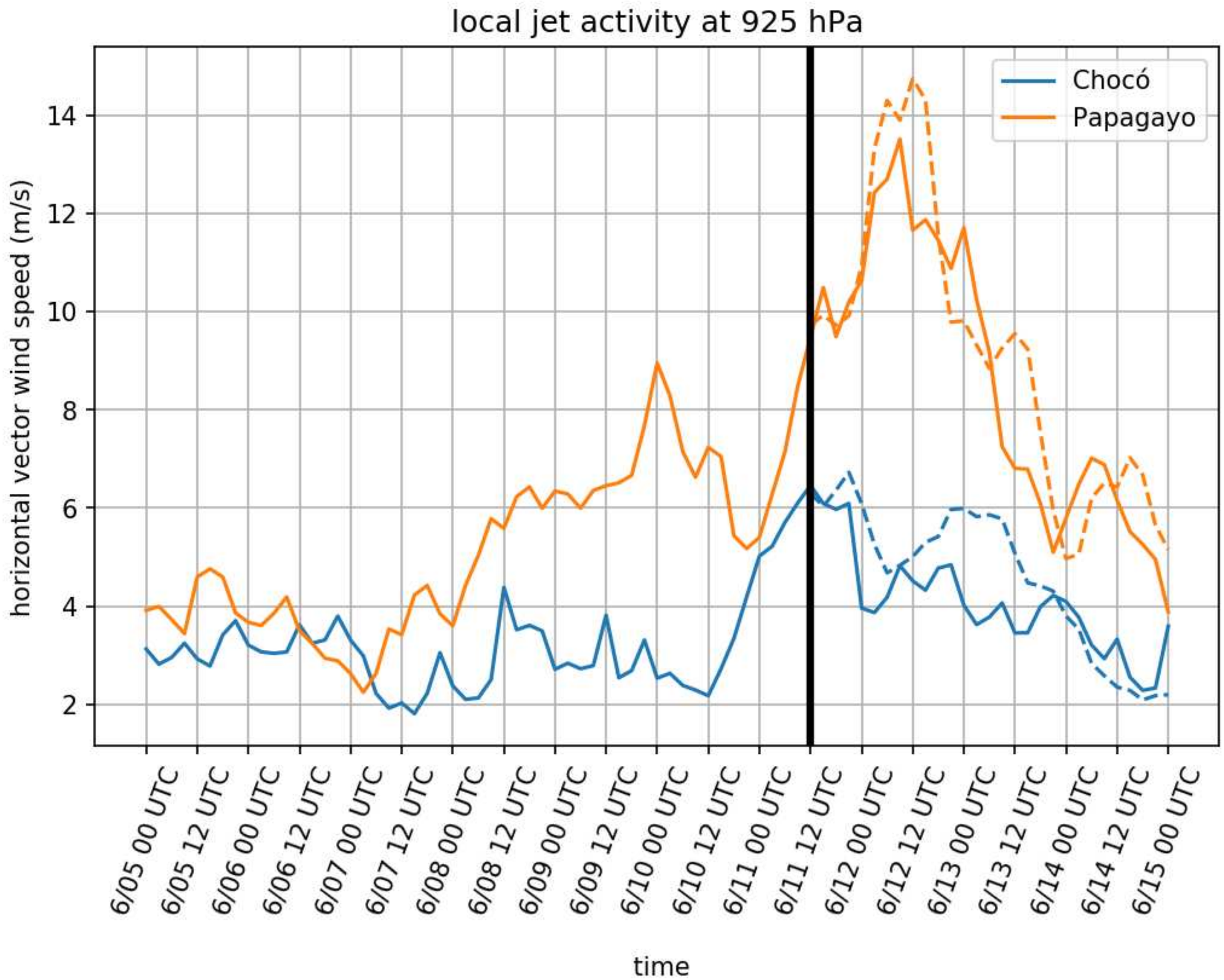

Figure 2.10: Horizontal vector wind speed ($\mathrm{m\ s^{-1}}$) at 925 hPa for the Papagayo (orange) and Chocó (blue) jets in ERA5 (solid) and WRF (dashed). The black vertical line at 1200 UTC 11 June 2012 represents the start of the WRF simulation.

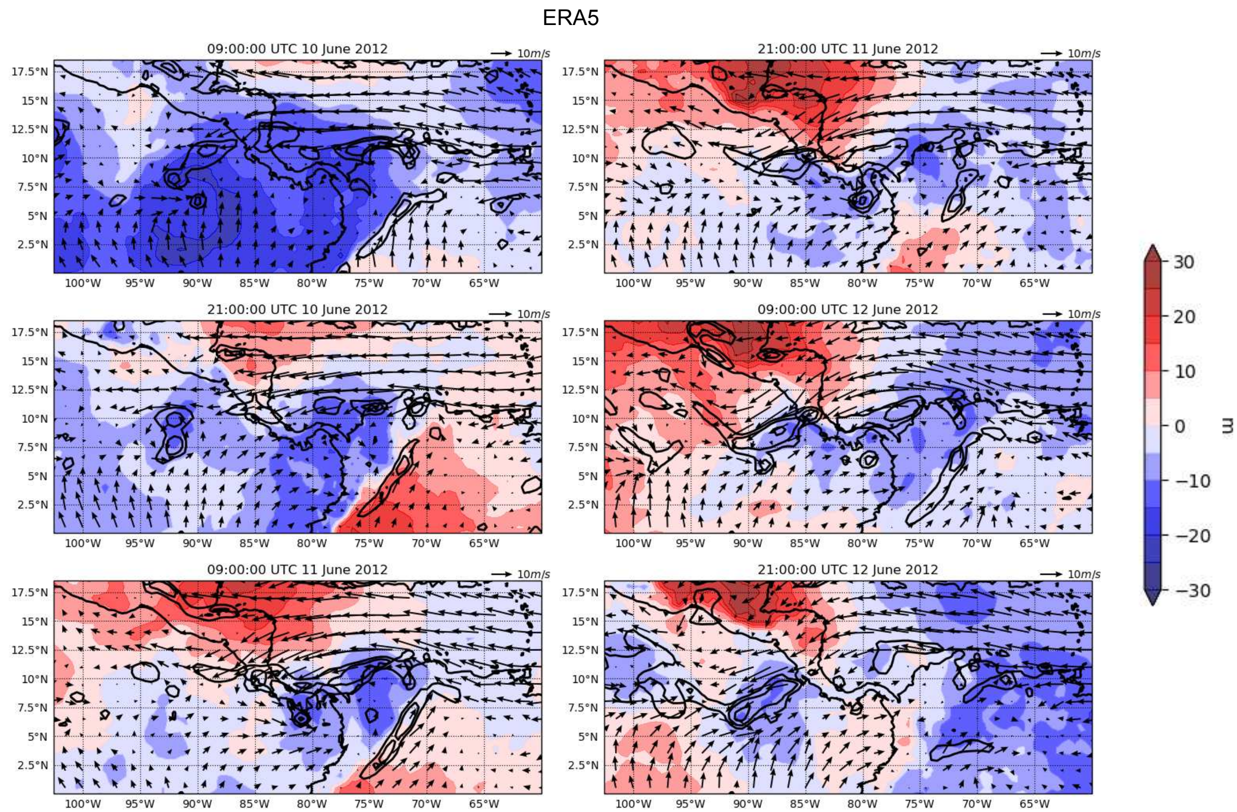

Figure 2.11: ERA5 925 hPa geopotential height with the average diurnal cycle removed (m; color contours), 925 hPa relative vorticity anomalies (s^{-1}; line contours), and 925 hPa wind (m s^{-1}; vectors, reference vector of 10 m s^{-1}). Vorticity contour interval is: 2.5, 5, 10, 15, 25, 45, 65×10^{-5} s^{-1}.

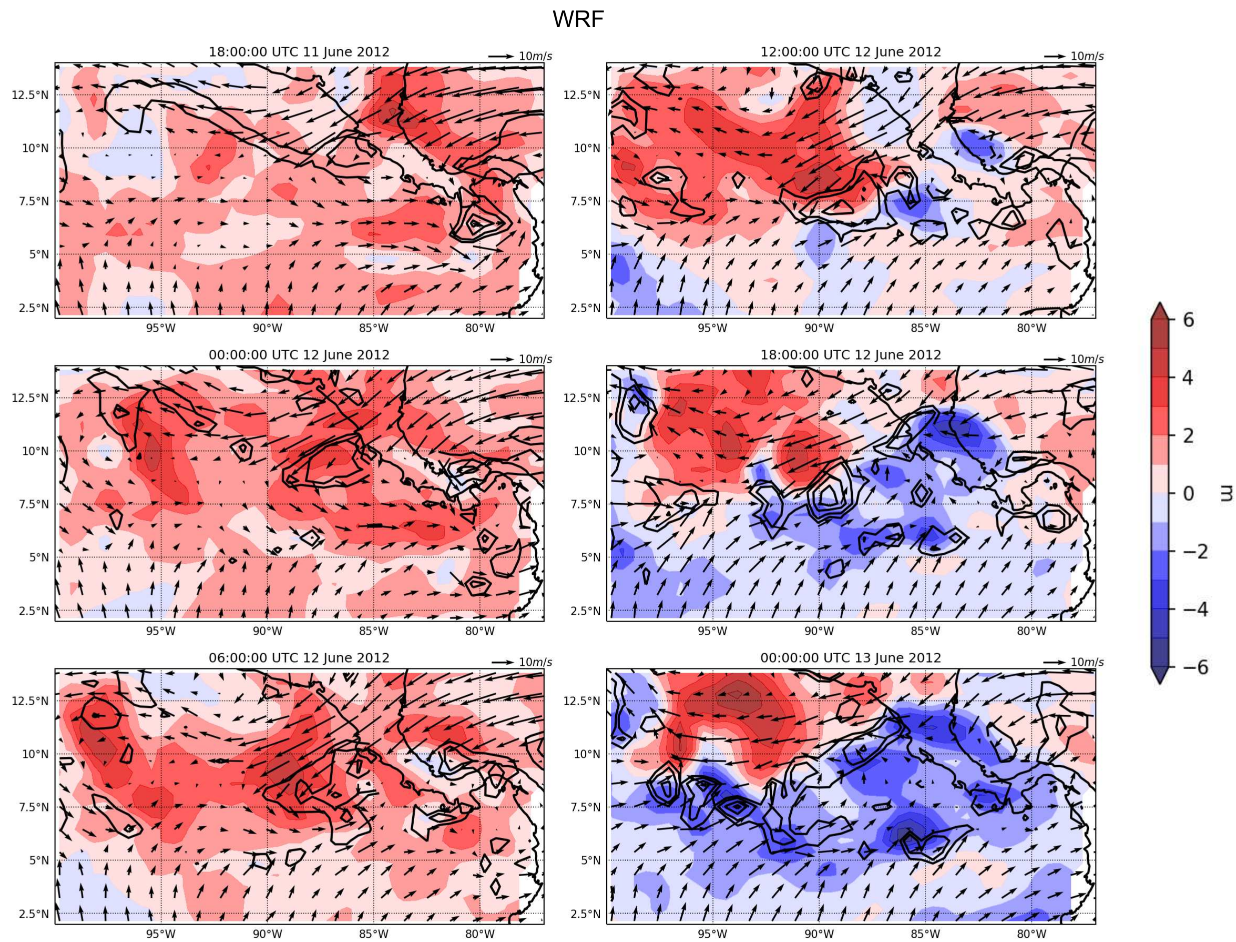

Figure 2.12: WRF 925 hPa geopotential height with the average diurnal cycle removed (m; color contours), 925 hPa relative vorticity anomalies (s^{-1}; line contours), and 925 hPa wind (m s^{-1}; vectors, reference vector of 10 m s^{-1}). Vorticity contour interval is: 2.5, 5, 10, 15, 25, 45, 65×10^{-5} s^{-1}.

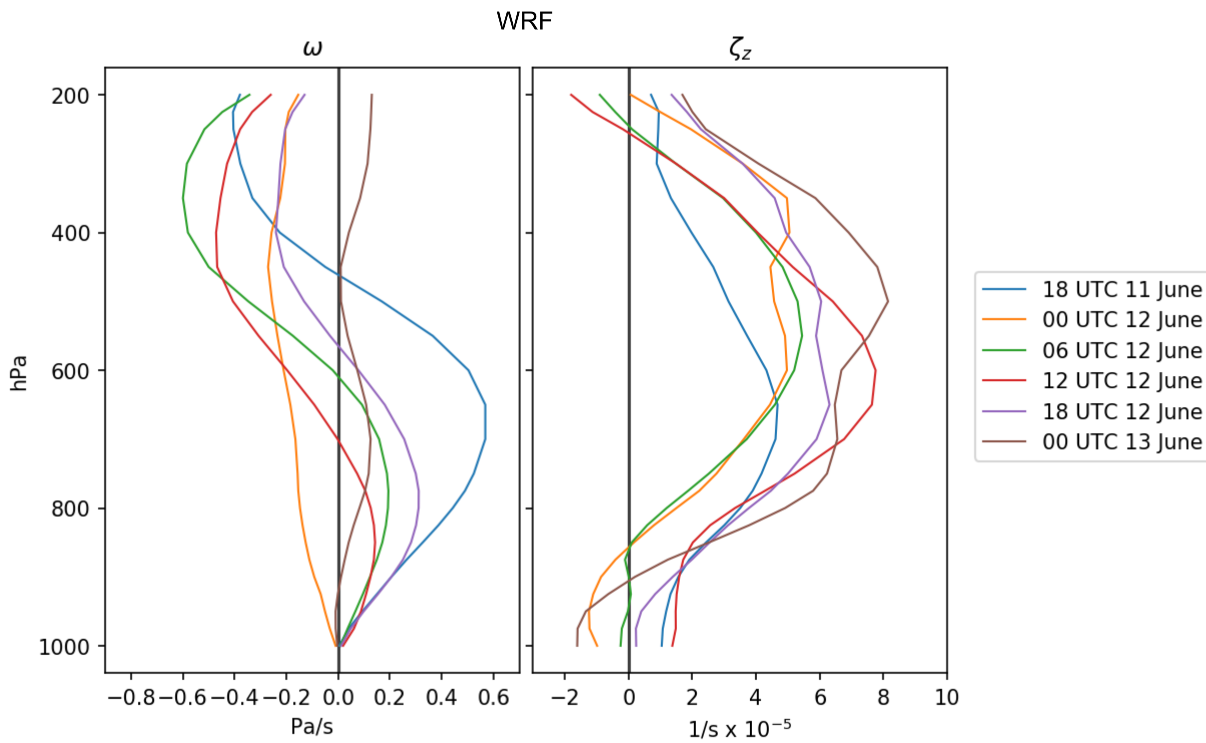

Figure 2.13: Vertical profiles of average WRF omega and vertical vorticity anomalies (Pa s^{-1}, and s^{-1} $\times 10^{-5}$, respectively) across an approximate 2°x2° box centered on the 500 hPa vorticity maximum of the disturbance every six hours starting at 1800 UTC 11 June 2012. Anomalies are relative to the time mean for the full simulation (1200 UTC 11 June 2012 to 0000 UTC 15 June 2012) over each respective box.

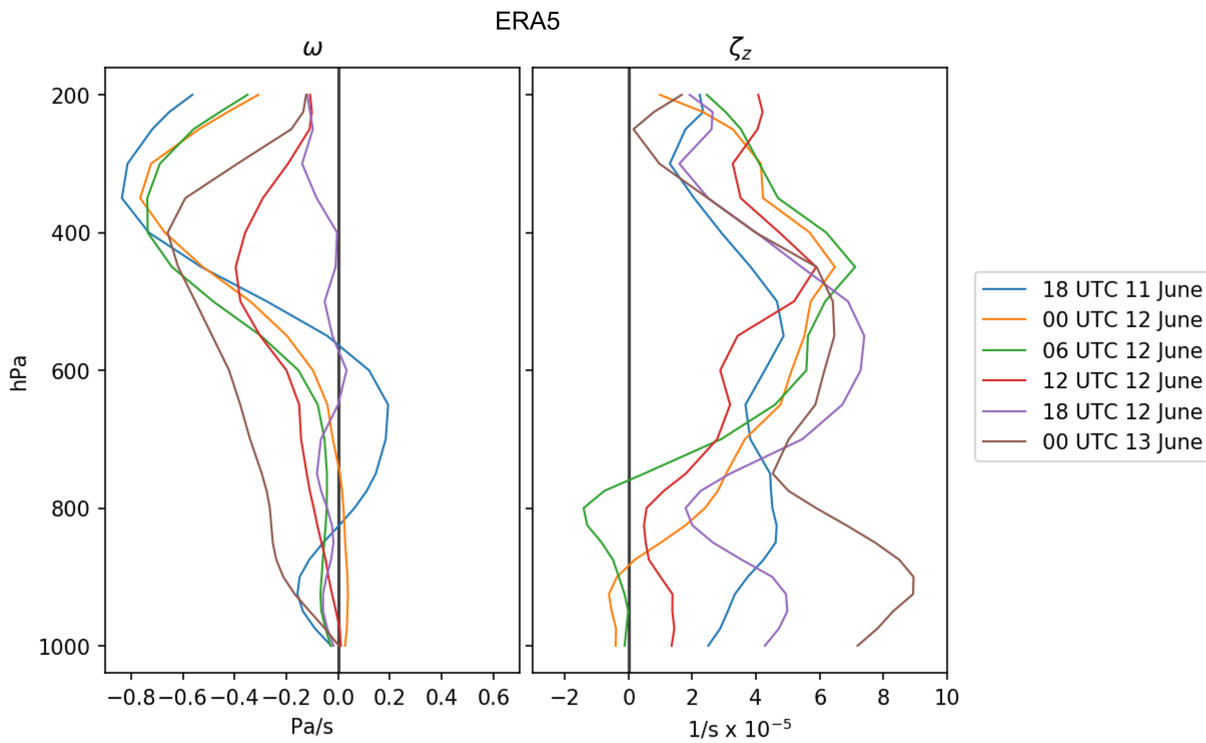

Figure 2.14: Vertical profiles of average ERA5 omega and vertical vorticity anomalies (Pa s^{-1}, and s^{-1} $\times 10^{-5}$, respectively) across a 2°x2° box centered on the 500 hPa vorticity maximum of the disturbance every six hours starting at 1800 UTC 11 June 2012. Anomalies are relative to the time mean for 0000 UTC 5 June 2012 to 2100 UTC 19 June 2012 over each respective box.

Chapter 3

The Impact of Central American Gap Winds on the East Pacific Background State and Easterly Wave Tracks

3.1 Introduction

The Papagayo and Tehuantepec wind jets are gap wind features stemming from the mountains of Central America. These wind jets have been shown to be active in both boreal winter and summer, with the Papagayo jet associated with easterly and northeasterly flow extending over the Pacific from Nicaragua and Costa Rica, and the Tehuantepec jet associated with northerly flow entering the east Pacific basin from Mexico (e.g., Chelton et al., 2000; Holbach and Bourassa, 2014). Both of the jets are observed at low levels (Chelton et al., 2000; Romero-Centeno et al., 2007; Serra et al., 2010; Holbach and Bourassa, 2014), and the Papagayo jet and its preceding easterly flow, the Caribbean low level jet (CLLJ), have been shown to extend up to around 700 hPa (Molinari et al., 1997; Wang, 2007; Amador, 2008). Holbach and Bourassa (2014) highlight that positive surface vorticity can be generated transiently due to horizontal shearing from the wind jets, while Serra et al. (2010) show that in the summer mean, the Papagayo jet supports a region of positive low level vorticity on its south flank extending westward into the basin. The gap winds and the CLLJ also transport moisture westward into the east Pacific, with jet activity in July and August supporting the midsummer drought in Central America (Mestas-Nuñez et al., 2007; Romero-Centeno et al., 2007; Perdigón-Morales et al., 2021).

East Pacific easterly waves are tropical disturbances that propagate westward and northwestward through the Intertropical Convergence Zone (ITCZ) and parallel to Central America (Thorncroft and Hodges, 2001; Serra et al., 2010). Serra et al. (2008) documents that east Pacific easterly waves have periods of about 5 days, wavelengths around 4000-5000 km, and phase speeds around

11 m s^{-1}. Convective processes in the waves and barotropic conversions between the wave and the background flow have been shown to intensify easterly waves in this region (e.g., Maloney and Hartmann, 2001; Serra et al., 2010; Rydbeck and Maloney, 2014, 2015; Whitaker and Maloney, 2018). Recent studies have also found that environmental moisture is crucial to easterly wave development by aiding in the coupling between the cyclonic wave circulation and convection (Rydbeck and Maloney, 2015; Adames and Ming, 2018; Wolding et al., 2020). Prior to their growth stage, east Pacific easterly waves can be initiated by several pathways, including: instability of the ITCZ flow (Ferreira and Schubert, 1997; Toma and Webster, 2010), triggering by Panama Bight mesoscale convective systems (Rydbeck et al., 2017; Whitaker and Maloney, 2020), and the propagation of African easterly waves into the basin (e.g., Frank, 1970; Serra et al., 2008). Once formed, easterly waves can develop into tropical cyclones (e.g., Dunkerton et al., 2009) and also produce around 50% of the summer rainfall across most of Central America (Dominguez et al., 2020), which underscores the need to investigate phenomena that impact the wave lifecycle.

The Papagayo and Tehuantepec jets have been linked to the genesis of tropical disturbances in the east Pacific (Mozer and Zehnder, 1996; Molinari et al., 1997; Serra et al., 2010; Holbach and Bourassa, 2014; Whitaker and Maloney, 2020). Mozer and Zehnder (1996) used an idealized model to show that easterly flow approaching the Sierra Madre mountains leads to a Tehuantepec-like jet that supports the generation of easterly waves downstream. Molinari et al. (1997) found that in 1991, the 700 hPa mean state flow in the vicintity of the CLLJ and Papagayo jet may have been unstable, which aids easterly wave formation in those regions. In easterly wave tracking results, Thorncroft and Hodges (2001) and Serra et al. (2010) found that easterly wave genesis does occur near the Papagayo jet region and continues along the east Pacific ITCZ. Whitaker and Maloney (2020) show that ERA5 reanalysis data of a case study suggests that interactions with the Papagayo jet may have supported the development of an easterly wave from a Panama Bight disturbance. Holbach and Bourassa (2014) highlight that both gap winds can also play a role in instances of tropical cyclogenesis in the basin, with the Papagayo jet being relatively more important.

Once formed, the development of east Pacific easterly waves in relation to gap winds and gap wind variability has also been studied (Mozer and Zehnder, 1996; Serra et al., 2010; Rydbeck and Maloney, 2014; Whitaker and Maloney, 2018). Mozer and Zehnder (1996) and Serra et al. (2010) highlight that in the vicinity of wind jets, barotropic conversions to eddy kinetic energy (EKE) are important for the growth of easterly waves. Whitaker and Maloney (2018) used a CLLJ index from the Papagayo jet region during periods isolated from Madden-Julian Oscillation (MJO) influence to find that weak jet periods have enhanced EKE, eddy available potential energy (EAPE) to EKE conversions, and barotropic conversions north of 10N relative to strong jet periods. Strong jet periods were found to have higher easterly wave track density to the south along the east Pacific ITCZ (Whitaker and Maloney, 2018), consistent with the findings of Serra et al. (2010). Maloney and Esbensen (2007) found that the MJO intensifies the Tehuantepec and Papagayo jets during its easterly phase. However, this MJO easterly phase is also associated with reduced precipitation in the eastern half of the basin (e.g., Maloney and Esbensen, 2007) and weaker easterly waves (Rydbeck and Maloney, 2014, 2015).

The purpose of this study is to isolate and quantify the impact that the Papagayo and Tehuantepec jets have on the east Pacific mean state and easterly waves. This will be accomplished through two regional modeling simulations, a boreal summer control run and a simulation that "fills in" the mountain gaps in Central America to remove the wind jets. Section 2 describes the methodology of this study, including the model setup and easterly wave tracking algorithm used. Sections 3 and 4 present results describing how the east Pacific mean state and easterly wave activity change with the gaps filled, respectively. Section 5 discusses possible reasons for the changes and further examines characteristics of easterly waves between the simulations. Section 6 provides the conclusions for this study.

3.2 Methodology

Data used in this study comes from the ERA5 reanalysis (Copernicus Climate Change Service (C3S), 2017; Hersbach et al., 2018) and from Weather Research and Forecasting (WRF) model

(Skamarock et al., 2008) simulations. The ERA5 data have a horizontal grid spacing of 0.5°, a temporal resolution of 6 hours, and consist of 29 pressure levels. Two WRF model simulations are used to test the influence of gaps winds on east Pacific easterly waves, and the details of the simulations are listed in Table 1. The first simulation is a control run and the second "fills in" the mountain gaps in the Central American mountains to block the gap winds. Both model simulations are run at 18 km horizontal resolution, have 40 vertical levels, are run with timesteps of 30 seconds, and output data every 6 hours. The horizontal resolution used in these WRF simulations is the same as in Rydbeck et al. (2017), who studied the impact of Panama Bight MCSs on easterly wave activity by flattening Central and South American topography. Each simulation consists of five May-November seasonal runs (2013-2017) to capture easterly wave activity over an extended period of time for more robust statistics. The New Simplified Arakawa-Schubert cumulus parameterization scheme (Han and Pan, 2011, NSAS) and the WRF Single Moment Six Class microphysics scheme (Hong and Lim, 2006, WSM6) were used in these simulations; Wu et al. (2015) and Dominguez et al. (2020) showed that these schemes could reasonably capture many of the mean state conditions in the east Pacific. As an example, the control run mean precipitation distribution in Figure 4 compares well with the observed precipitation in the region (e.g., Maloney and Esbensen, 2007; Crosbie and Serra, 2014; Wu et al., 2015; Rydbeck et al., 2017), although the simulated values of rain rate are elevated. Finally, WRF model output is regridded and vertically interpolated to 0.5°horizontally and 1000 hPa to 200 hPa by 50 hPa vertically for direct comparison to ERA5.

The experimental model simulation modifies the topography of Central America in order to block the Tehuantepec and Papagayo gap wind features. In this study, this model simulation will be referred to as either the "gaps filled" or "modified topography" simulation. The method for filling in the gaps was inspired by Yoo et al. (2017), who looked at gap wind impacts on the genesis of tropical cyclone Arlene (2005) in the Caribbean Sea. The topography of Central America is altered as follows. First, the model geography file is loaded in, and then for each longitude between 7N°-22N°, 81W°-100W°, the maximum height of the topography and its associated coordinates are found. From these maximum height topography points, only points that are 1500 m or higher are retained to establish connecting points. Then, line segment coordinates are calculated between these connecting points. Then, along this path, if the points are less than 2000 m, the height is set to 2000 m, similar to what is done in Yoo et al. (2017). Further, points that are adjacent to the path (to the north, south, east, and west) are then raised to 1500 m if they have a height that is less than 1500 m. This new topography is then used in the WRF simulations. Figure 1 shows the topography in both WRF simulations, and the modified topography (bottom) has a similar appearance to that in Yoo et al. (2017).

Easterly wave tracking in this study is accomplished by using a tracking algorithm that is adapted and modified from the tracking algorithm used in Heikenfeld et al. (2019) (the "tobac" tracking algorithm), which utilizes the trackpy package (Allan et al., 2019). In Heikenfeld et al. (2019), the tracking algorithm was used to track individual clouds in model simulations and satellite data. The easterly wave tracking algorithm used in this study starts by loading in the u and v wind from the WRF output data for each May-Nov. year, vertically averaging it from 850 hPa to 600 hPa, and calculating vertically averaged relative vorticity. Next, the vorticity is bandpass filtered to 2.5-12 days, subsetted to retain only June-October (for both filtered and unfiltered vorticity), and then smoothed spatially with a Gaussian filter with σ = 1.5.

Now, with the spatially smoothed, bandpass filtered, 850 to 600 hPa vorticity, easterly wave features are first highlighted by creating a binary image of vorticity areas that are greater than the threshold of 0.636×10^{-5} s^{-1}, with tropical cyclone features retained as well. This threshold was determined by taking half of the control run season average ITCZ (5N°-12.5N°, 105W°-85W°) unsmoothed filtered vorticity standard deviation. With regions greater than the threshold calculated, an erosion of 2 pixels (1°) was applied to the binary regions, similar to what is done in Heikenfeld et al. (2019). Next, these regions of above-threshold vorticity are detected based on an algorithm adapted from trackpy (Allan et al., 2019): the vorticity regions are labeled at each time step, are filtered to only include features whose centroids occur in 4N°-25N°, 62.5W°-117.5W°, and have areas of at least 9 pixels (approximately $2^{\circ 2}$). The features are then stored with their centroid, label, and time step information, among other characteristics.

The features are tracked in time using the trackpy package (Allan et al., 2019) and is done in a similar manner to what is done in Heikenfeld et al. (2019), with a search range of 6 pixels that corresponds to a radius of 3°. As described in Heikenfeld et al. (2019), the search range represents the maximum expected distance a feature could travel from a predicted position in the next time step; using a phase speed of 15 m s^{-1} (greater than the phase speeds noted in Serra et al. (2008)) leads to approximately 3°of maximum expected movement over six hours. Similar to Heikenfeld et al. (2019), the previous velocities of the features are taken into account for predicting motion during tracking as well. The trackpy tracking algorithm (Allan et al., 2019) links features across times and will assign numbers for distinct tracks. An additional feature incorporated into this easterly wave tracking algorithm is that once the features have been tracked, the tracks are then reanalyzed to handle the splitting and merging of vorticity features and to adjust their labels accordingly. Finally, the tracks are filtered to remove tracks that occur for less than 1.5 days using a trackpy function (Allan et al., 2019). When the tracking is complete, each years' easterly wave track data are combined and then can be analyzed.

3.3 Model Basic State

Figure 1 shows the topography in the control and gaps filled simulations that were discussed in the section above. In the control run, the Central American mountains and the Andes mountains in South America are evident. Also notable are the gaps in the Central American mountains that are responsible for the Tehuantepec jet (gap near 17.5N, 95W) and Papagayo jet (gap near 12N, 85W). In the modified topography simulation, these mountain gaps have been effectively "filled" by adding in a strip of raised topography to connect elevated regions in Central America. This new section of topography is 2000 m at its peak as discussed above.

With the mountain gaps successfully filled-in, changes to the mean state conditions in the east Pacific can be assessed. Figure 2 shows the mean precipitable water and 900 hPa wind for the control and modified topography simulations, along with the experimental minus control differences. In the control run, a mean moisture maximum extends westward from the Panama Bight and highlights the location of east Pacific ITCZ from approximately 7.5 to 10N in latitude. Moisture also decreases more sharply to the south of the ITCZ than it does northward, as discussed in Rydbeck and Maloney (2015). In terms of low level wind, flow through the gaps resembles the Tehuantepec and Papagayo jets while the strong easterlies in the Caribbean associated with the CLLJ are apparent. Westerly low level flow from the Chocó jet (Yepes et al., 2019) approaches the Panama Bight.

Looking at the gaps-filled run and differences from the control, it is clear that raising the topography in Central America effectively shuts down the Tehuantepec and Papagayo jets and leads to weaker mean easterlies north of the ITCZ. In addition to these westerly low level wind differences downstream of the raised topography, the added mountains appear to redirect some of the flow southward, crossing over Panama instead. The gaps filled run also has a notable reduction in precipitable water north of 7.5N with negative differences reaching over -1.2 kg m^{-2}. The southern portion of the basin and the eastern side of the raised topography have increased moisture relative to the control run.

Figure 3 highlights changes to outgoing longwave radiation (OLR) and 700 hPa vorticity in the simulations. With the gaps present in the control, positive vorticity is observed extending from the Papagayo jet region westward along 10N. Reduced OLR is a proxy for deep convection and largely follows the precipitable water in Figure 2, consistent with convective activity in the ITCZ region. The highest vorticity values near the ITCZ in the control are slightly north of the lowest OLR values. With the gaps filled-in, the 700 hPa positive vorticity feature in the east Pacific dissipates and negative vorticity differences are strongest near the Central American coastline. Further, differences in the OLR field suggest decreased convective activity in the basin for the modified topography run, particularly on the northern side of the ITCZ. Convective activity seems to strongly increase on the windward side of the new mountains, in the far western Caribbean Sea.

Changes in precipitation (Figure 4) largely follow the characteristics of moisture and OLR noted in Figures 2 and 3. Mean precipitation in the control run resembles the observed pattern of precipitation in the region (e.g., Maloney and Esbensen, 2007; Crosbie and Serra, 2014; Wu et al., 2015; Rydbeck et al., 2017), with strong rainfall in the Panama Bight and the east Pacific ITCZ. With the gaps and wind jets removed, the precipitation along and north of the ITCZ broadly decreases by at least 1.5 mm day^{-1} and is reduced by 3 mm day^{-1} in some locations. In the western Caribbean, precipitation strongly increases likely due to increased topographic lifting, while precipitation also increases to the south of Panama. The results in Figures 2-4 highlight that filling in the mountain gaps leads to a reduction in mean moisture, convective activity, precipitation, and mid level vorticity from the ITCZ northward in the east Pacific.

3.4 Easterly Wave Tracking

Using the tracking algorithm discussed in section 2, 850-600 hPa filtered vorticity disturbances are tracked in both simulations. Figure 5 provides an example of what the tracking looks like for individual disturbances. The top panel shows a snapshot from 2013 in the control run, with vorticity regions shown in black and tracked disturbances labeled. The bottom two panels show the easterly wave tracks for 2013 in the model runs. The control run appears to have more wave activity to the east of 105W in the east Pacific than in the gap-filled run, with both simulations having activity along the ITCZ and northward. The set of individual east Pacific tracks in Figure 5 have qualitative similarities to the 1994 and 1995 tracks shown in Thorncroft and Hodges (2001).

Now, these track observations can be converted to track density by recording the total number of disturbance observations in 2°x2°boxes. Figure 6 shows the track density total for the 2013-2017 control and modified topography runs, along with the experimental minus control difference. Track density for the control run highlights that easterly waves are active along the east Pacific ITCZ and northward. These regions of wave activity are consistent with prior tracking studies (Thorncroft and Hodges, 2001; Serra et al., 2010). Comparing the control run to the modified topography run, removing the gaps and wind jets leads to a reduction in track density in the basin, particularly to the east of 105W in the ITCZ and northward along 95W. In general, the shape of the track density pattern in the gaps filled simulation remains similar to the control, but the counts of wave observations are reduced in the aforementioned regions.

Figure 7 shows the genesis density for easterly wave disturbances in both simulations. Genesis of a wave is determined by the first coordinate point of a tracked disturbance. The control simulation has high genesis density in the Panama Bight region, the eastern ITCZ, and near where the Papagayo and Tehuantepec jets enter the basin. Serra et al. (2010) showed that the ITCZ and Papagayo jet regions are locations of easterly wave genesis, while the growth of Panama Bight disturbances into waves has been documented by Kerns et al. (2008), Rydbeck et al. (2017), and Whitaker and Maloney (2020). Both simulations have high genesis density on the eastern edge of the domain, likely due to the boundary forcing and waves entering the domain. The genesis density differences reveal a general reduction of generated waves in the eastern portion of the east Pacific during the modified topography run, especially near and downstream of the jet regions. So, Figures 6 and 7 show that easterly waves appear to not form as often when the gaps and wind jets are removed, which leads to a reduction in the number of easterly wave observations in the basin.

In a similar manner to Figures 6 and 7, track and genesis density was calculated for 2013-2017 ERA5 data for comparison (Figure 8). In ERA5, easterly waves are relatively more prominent in the ITCZ and the density map shows a slightly more coherent northwestward track than in WRF (Figure 6). In relation to the track density plots in Thorncroft and Hodges (2001) and Serra et al. (2010), the ERA5 track density has its peak values shifted to the southeast (Figure 8). Further, ERA5 track density counts are higher and more narrowly confined in the ITCZ versus the control and are somewhat lower and less widespread to the north. In terms of genesis density, ERA5 shows a strong genesis region around the Panama Bight, as well as near the Tehuantepec jet. This genesis pattern differs from Serra et al. (2010), who showed strong genesis density occurs downstream of the Papagayo jet, centered near 10N. Overall, the easterly wave track and genesis densities found for ERA5 (Figure 8) support the control run findings (Figures 6 and 7), and the ERA5 track density compares well to previous easterly wave track density analyses for the region (Thorncroft and Hodges, 2001; Serra et al., 2010).

3.5 Mechanisms and Easterly Wave Characteristics

To explore potential mechanisms for the reduction of easterly wave activity, Figures 9 and 10 show the mean vertically-integrated moisture flux and respective moisture flux divergence for 1000-200 hPa (Figure 9) and 1000-800 hPa (Figure 10). Equations 1 and 2 describe these calculations, and are inspired by similar equations from Trenberth and Guillemot (1998), Mundhenk et al. (2016), and Fu et al. (2017):

$$\text{moisture flux} = \langle \overline{[qu]}, \overline{[qv]} \rangle \tag{3.1}$$

$$\text{moisture flux divergence} = \frac{\partial \overline{[qu]}}{\partial x} + \frac{\partial \overline{[qv]}}{\partial y} \tag{3.2}$$

where q is specific humidity, u is the zonal component of the wind, v is the meridional component of the wind, $[\,] = \frac{1}{g}\int_{200\,hPa}^{1000\,hPa} (\,)\,dp$ is the vertical integral with dp = 5000 Pa and g = -9.8 m s^{-2}, and overbars are the time mean.

Both Figures 9 and 10 show that in the control run the ITCZ is a location of strong moisture flux convergence (negative divergence). This implies that more mean precipitation is occuring than evaporation in this region (e.g., Trenberth and Guillemot, 1998, Equation 1 in their paper). Figure 10 highlights the importance of the low level wind jets in transporting moisture across the Central American isthmus into the east Pacific, with evident moisture flux vectors in jet regions and low level moisture flux convergence along and north of the ITCZ. Looking at the differences in Figure 9, the removal of the gaps and wind jets leads to westerly moisture flux differences and moisture flux divergence differences north of 7.5N in the basin. This result suggests reduced mean precipitation from the ITCZ northward and compliments the positive OLR differences and negative precipitation differences seen in Figures 3 and 4. In addition, the differences in Figure 9 highlight that the introduction of additional topography leads to moisture flux convergence differences on the windward side of the mountains in the Caribbean and the directing of moisture southward across Panama. This difference pattern is similar at low levels (Figure 10). Strong low level moisture flux divergence differences and westerly moisture flux differences in Figure 10 demonstrate that the Papagayo and Tehuantepec jets are crucial for providing moisture to the east Pacific in the mean state. Taken together, Figures 9 and 10 illustrate that removing the Papagayo and Tehuantepec jets leads to a reduction of westward moisture transport, which inhibits convective activity and precipitation in the east Pacific relative to the control run. Thus, without the gaps, support for moisture and precipitation that helps maintain easterly waves is cut off, as these waves rely on a moist background environment that supports convection (Rydbeck and Maloney, 2015; Adames and Ming, 2018; Wolding et al., 2020).

Looking for evidence that removing the jets changes the eddy kinetic energy budget of the easterly waves through eddy-mean flow interactions, composite ITCZ easterly waves are calculated (Figure 11). These composites are calculated by averaging across all disturbance observations that occured in the ITCZ region (5-12.5N, 105-85W) based on the disturbance center, for a 15°x 15°box centered on the disturbance. The left panel of Figure 11 shows the composite 2.5-12 day bandpass filtered 850-600 hPa vorticity for ITCZ easterly waves in the control run (solid contours) and modified topography run (dashed contours). The right panel repeats the control run wave contours but also shows the vorticity differences when subtracting the composite control wave from the modified topography wave. In general, the composite ITCZ easterly waves in both simulations are similar, both in terms of strength and shape. The control run easterly wave has slightly higher composite vorticity and more of a southwest to northeast tilt. Southwest to northeast wave tilts promote wave growth from barotropic conversions in cyclonic shear (e.g., Rydbeck and Maloney, 2014). Interestingly, the control wave does not strongly show this horizontal tilting and there is not much of a difference between the horizontal structures of the waves. Further work assessing the barotropic energy conversions in these waves could put this finding into better context.

Furthering this composite analysis, Figure 12 shows the frequency distributions of area-averaged filtered 850-600 hPa vorticity for the identified ITCZ (5-12.5N, 105-85W) easterly wave observations, with the area-average taken across the relative longitudes -4 to 4 and relative latitudes -2 to 2 from the center point. The control run has more ITCZ wave observations (N=2357) and individual waves (N*=267) than the modified topography run (N=1769, N*=218), supporting the changes in track density seen in the region in Figure 6. The control distribution is broader than the modified topography distribution, and has its peak shifted slightly to the left. However, both distributions appear to have similar mean area-average vorticity values. Figures 11 and 12 highlight that although the aformentioned mean state changes occur with fewer waves, the ITCZ easterly waves that exist are of similar strength and have slight differences in tilt.

Figure 13 displays the 850-600 hPa bandpass filtered vorticity variance for both simulations and the differences subtracting off the control run. Reminescent of the easterly wave tracking results in Figure 6, the control run is associated with larger easterly wave-time scale variability than the gaps filled run. This reduction in variance is consistent with the findings discussed above, that fewer disturbances with similar strength seem to be occuring. While the reduction in ITCZ vorticity variability with the removal of gap winds is evident, there are also large changes in vorticity variance in the northern and western parts of the basin. These large variance differences may be due to changes in tropical cyclone activity, with a reduction in tropical cyclone activity potentially occuring when the mountain gaps are filled. Holbach and Bourassa (2014) highlight that both the Papagayo and Tehuantepec jets produce surface vorticity that contributes to tropical cyclogenesis in the region. Regardless of potential changes to tropical cyclone activity, the reduction in easterly wave-time scale variability coincides with the locations of negative precipitable water differences, positive OLR differences, negative precipitation differences, and moisture flux divergence differences.

While the Papagayo and Tehuantepec jets support a moister east Pacific basic state with increased convective and easterly wave activity, the composite ITCZ wave analysis suggests that the strength and horizontal structure of ITCZ waves in the model may change modestly with the removal of the wind jets. Additional analyses into the eddy kinetic energy and vorticity budgets of easterly waves in the simulations would provide a clearer picture of how the waves are developing in two different mean state conditions. For example, with the reduction of mean state moisture and convective activity, the conversion of eddy available potential energy to eddy kinetic energy in the waves may be reduced, but would the decreases in barotropic conversions to eddy kinetic energy (as a result of the removed positive shearing due to the Papagayo jet) be of similar magnitude? Do the aforementioned mean state changes have any consequence for the vertical structure of convection in the waves and the generation of vorticity via vortex stretching? Further, why do the waves have similar composite sizes and strengths while the wave frequency is the main easterly wave quantity that is affected by removing the wind jets? Easterly waves vary based on the background state (e.g., Rydbeck and Maloney, 2014, 2015), and the fact that the composite waves are similar in strength and structure could point to how the easterly waves are represented in the model, and may be a potential limitation of this study.

3.6 Conclusions

This study investigates how the east Pacific mean state and easterly wave activity are impacted by the Papagayo and Tehuantepec wind jets. Specifically, a WRF simulation that fills in the gaps in the Central American mountains is contrasted with a control run, with each simulation consisting of five summer seasons. To analyze easterly wave activity and composites, an easterly wave tracking algorithm adapted from Heikenfeld et al. (2019) and utilizing trackpy (Allan et al., 2019) is developed.

Mean state results and moisture flux calculations highlight the important thermodynamic and dynamic roles that the Papagayo and Tehuantepec jets have in conditions of the east Pacific. In the simulation without gap winds, the east Pacific from the ITCZ and northward is drier, has less convective activity and precipitation, and has a reduction in positive vorticity (Figures 2-4). A moisture flux and moisture flux divergence analysis (Figures 9 and 10) links these mean state precipitation changes to the reduction in moisture being fluxed into the basin from the Gulf of Mexico and Caribbean Sea, which is subsequently converged. Low level westerly wind differences are prominent from the ITCZ northward when the gap winds are blocked; the blocking of the flow also leads to a diversion of the low level wind and moisture southward over Panama (Figures 2 and 10). Further, the introduced topography leads to topographic lifting and precipitation on the windward side of the mountains (Figure 4). Rydbeck and Maloney (2014) and Rydbeck and Maloney (2015) show that mean state changes such as these can have important implications for easterly waves, particularly given that east Pacific easterly waves are reliant on moisture and subsequent diabatic heating for their development (Rydbeck and Maloney, 2015; Adames and Ming, 2018; Wolding et al., 2020).

Easterly wave tracking results show that the Papagayo and Tehuantepec wind jets appear to support both elevated track density and genesis density in the eastern portion of the basin in the control run compared to the gaps filled run (Figures 6 and 7). This result generally supports the findings of Serra et al. (2010) and Whitaker and Maloney (2018), who found that enhanced ITCZ easterly wave numbers are linked to stronger CLLJ conditions. In addition to a track density metric, easterly wave-time scale variance (Figure 13) decreases in the ITCZ and poleward in the gaps filled simulation. This result suggests that easterly wave and potentially tropical cyclone activity are aided by these gap winds, consistent with Holbach and Bourassa (2014). Interestingly, however, a composite analysis of ITCZ easterly waves reveals that there are not major differences in the horizontal structure and strength of vorticity in the waves between the simulations, although there are fewer of them. More work needs to be done to elucidate this finding.

Going forward, an analysis of the easterly wave eddy kinetic energy budget in these simulations will reveal how the mean state changes found in this study impact the growth of the waves. A budget study may be able to further investigate the pecularity of the modified topography run having reduced easterly wave activity but comparable wave structures and strengths to the control run. Finally, studies looking at the predictability of favorable interactions between gap winds and easterly waves would be beneficial to the operational community, while observations from field campaigns like OTREC (Fuchs-Stone et al., 2020; Huaman et al., 2021, submitted) may be able to provide additional insight into gap wind-easterly wave interactions as well.

Table 3.1: WRF model simulation details

Model	WRF-ARW V3.9.1.1 (Skamarock et al., 2008)
Domain	5S°-30N°, 120W°-60W°
Simulation Dates	May-Nov., 2013-2017
Input interval	6 hr (21600 seconds)
Input data	ERA5 (Hersbach et al., 2018); 0.5°(horizontal), six hourly, 29 pressure levels; surface input data has the same horizontal and temporal resolution, and SST is updated every 24 hours.
Time step	30 seconds
Resolution	18 km (horizontal), 40 vertical levels
Cumulus Parameterization	NSAS (Han and Pan, 2011)
Microphysics	WSM6 (Hong and Lim, 2006)
Radiation	CAM (Collins et al., 2004)
Land Surface Model	Noah (Tewari et al., 2004)
PBL scheme	YSU (Hong et al., 2006)

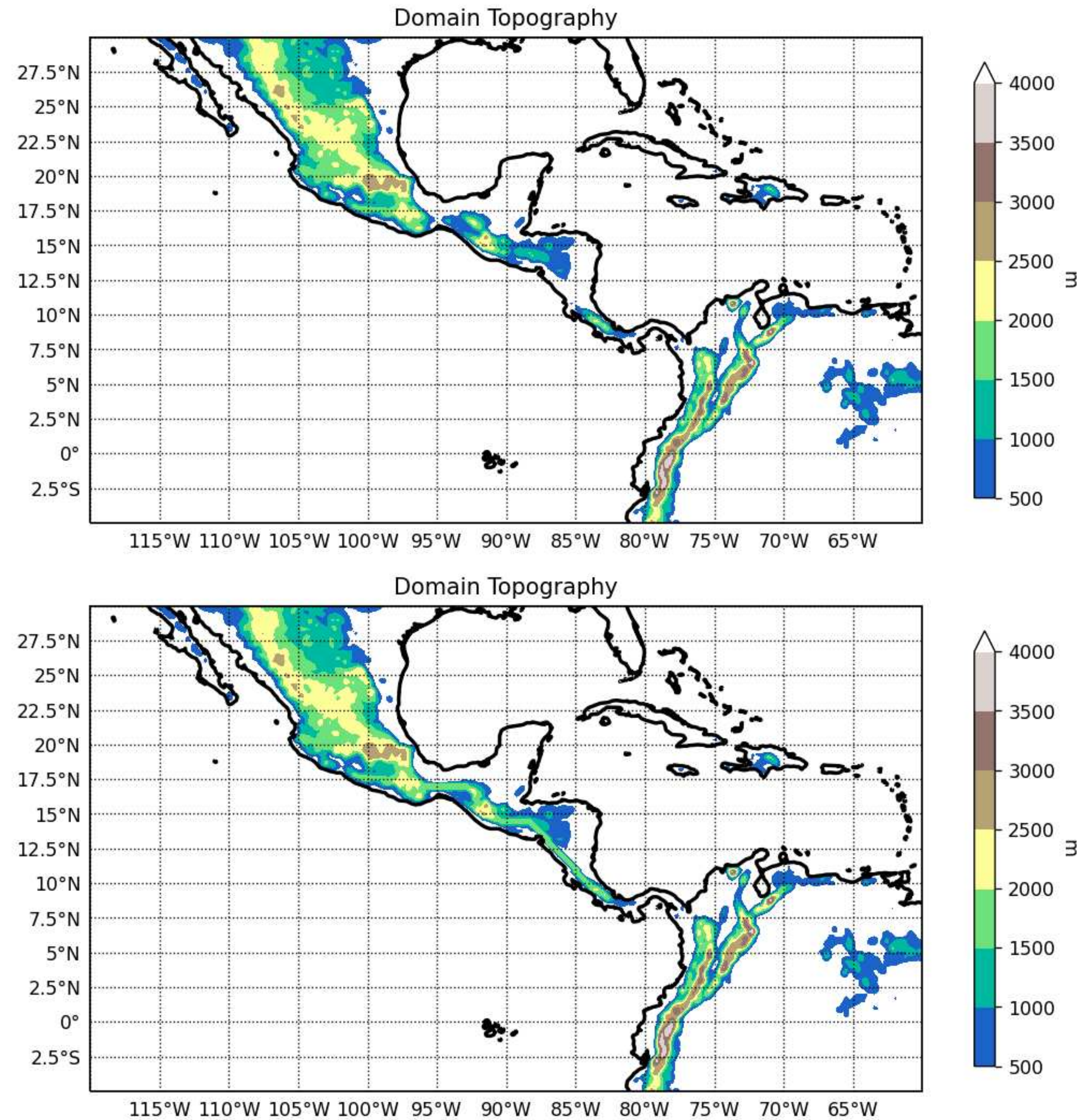

Figure 3.1: Model topography (meters MSL) for the control (top) and gaps filled (bottom) runs.

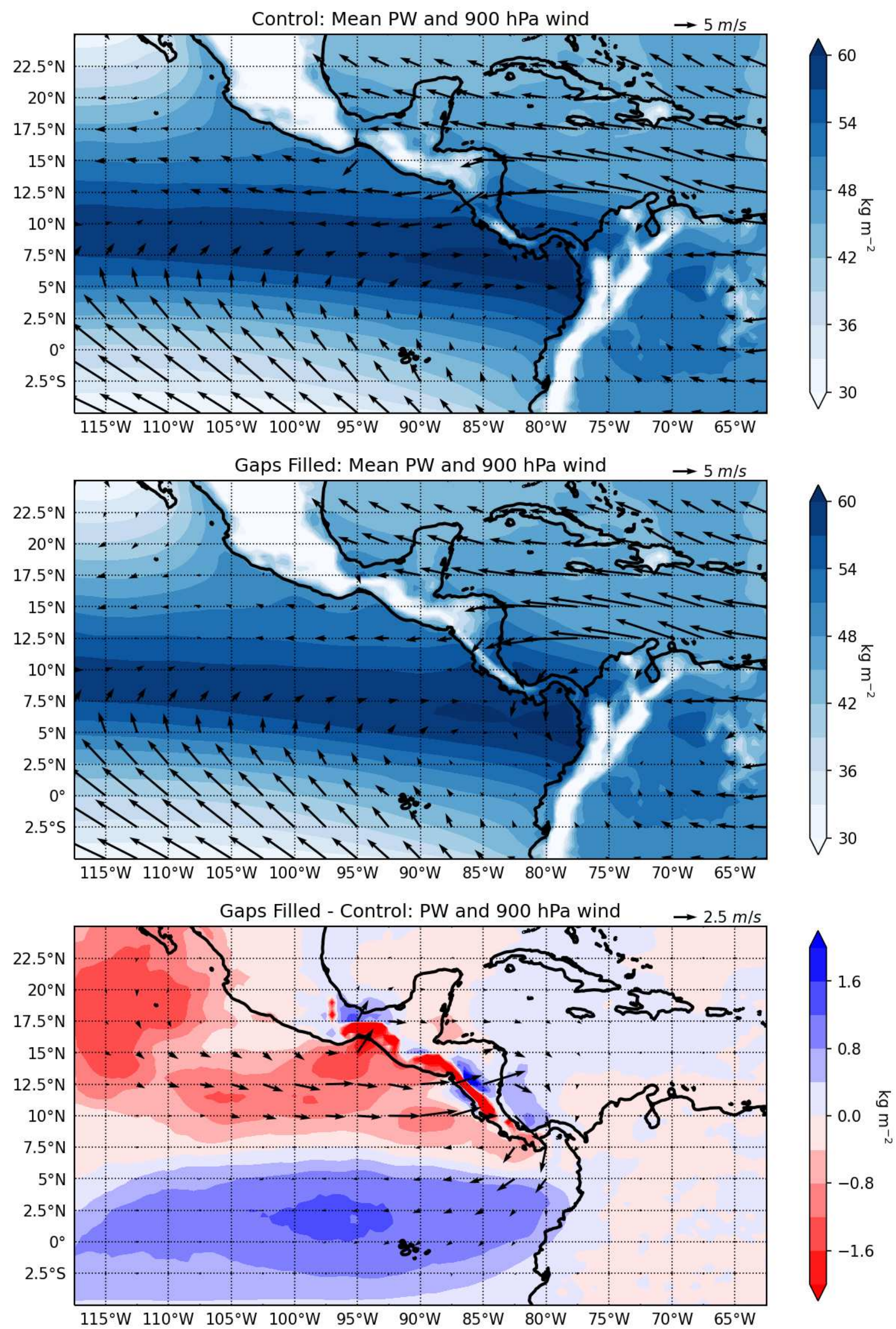

Figure 3.2: June-October mean precipitable water (kg m^{-2}, color contours) and 900 hPa wind (m s^{-1}, vectors) for the control (top) and gaps filled (middle) simulations. Differences of these variables (gaps filled minus control) are shown in the bottom panel.

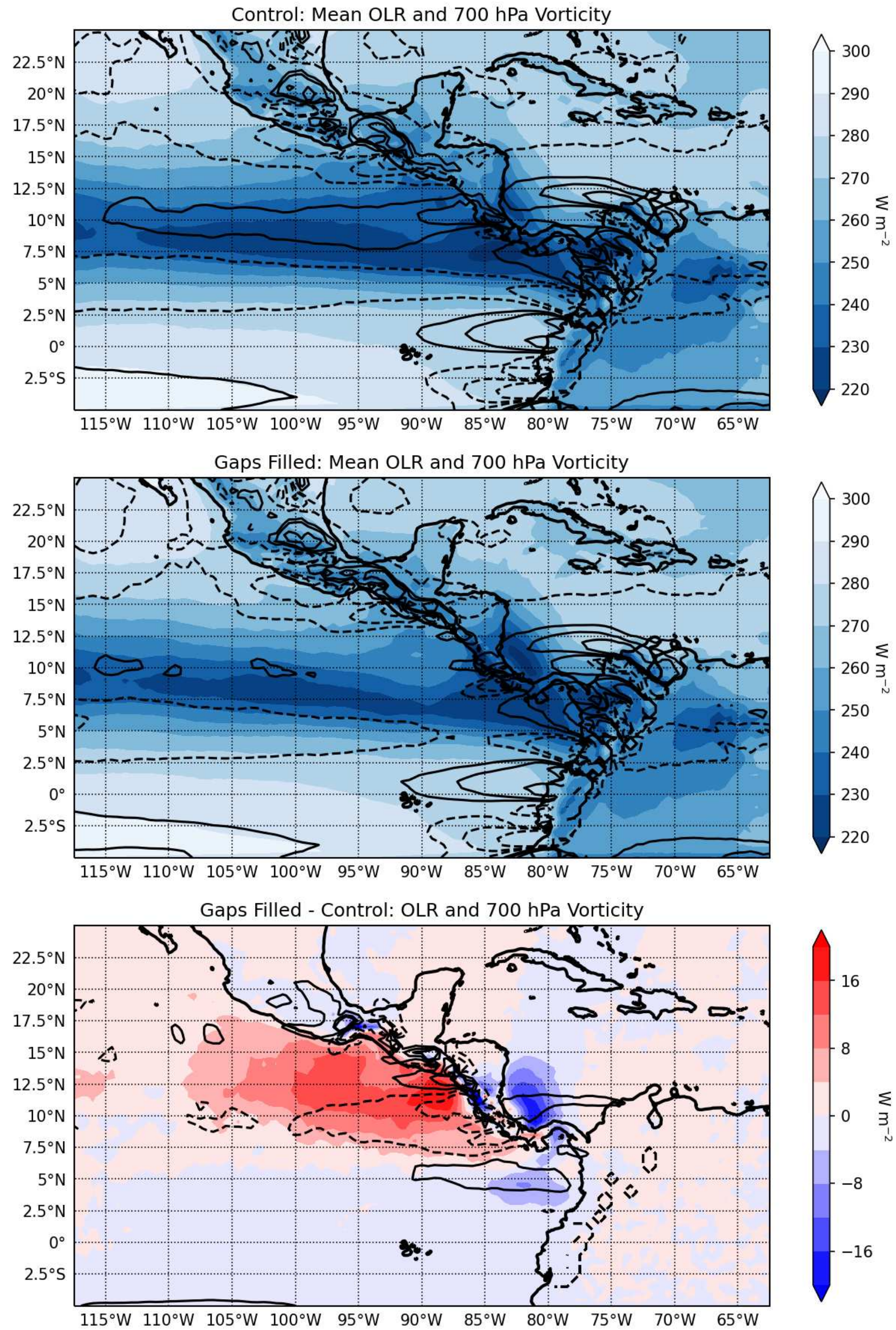

Figure 3.3: June-October mean OLR (W m^{-2}, color contours) and 700 hPa vorticity (s^{-1}, line contours of -20, -10, -5, 5, 10, 20 $\times 10^{-6}$) for the control (top) and gaps filled (middle) simulations. Differences of these variables (gaps filled minus control) are shown in the bottom panel. Vorticity difference line contours are -12.5, -7.5, -2.5, 2.5, 7.5, 12.5 $\times 10^{-6}$.

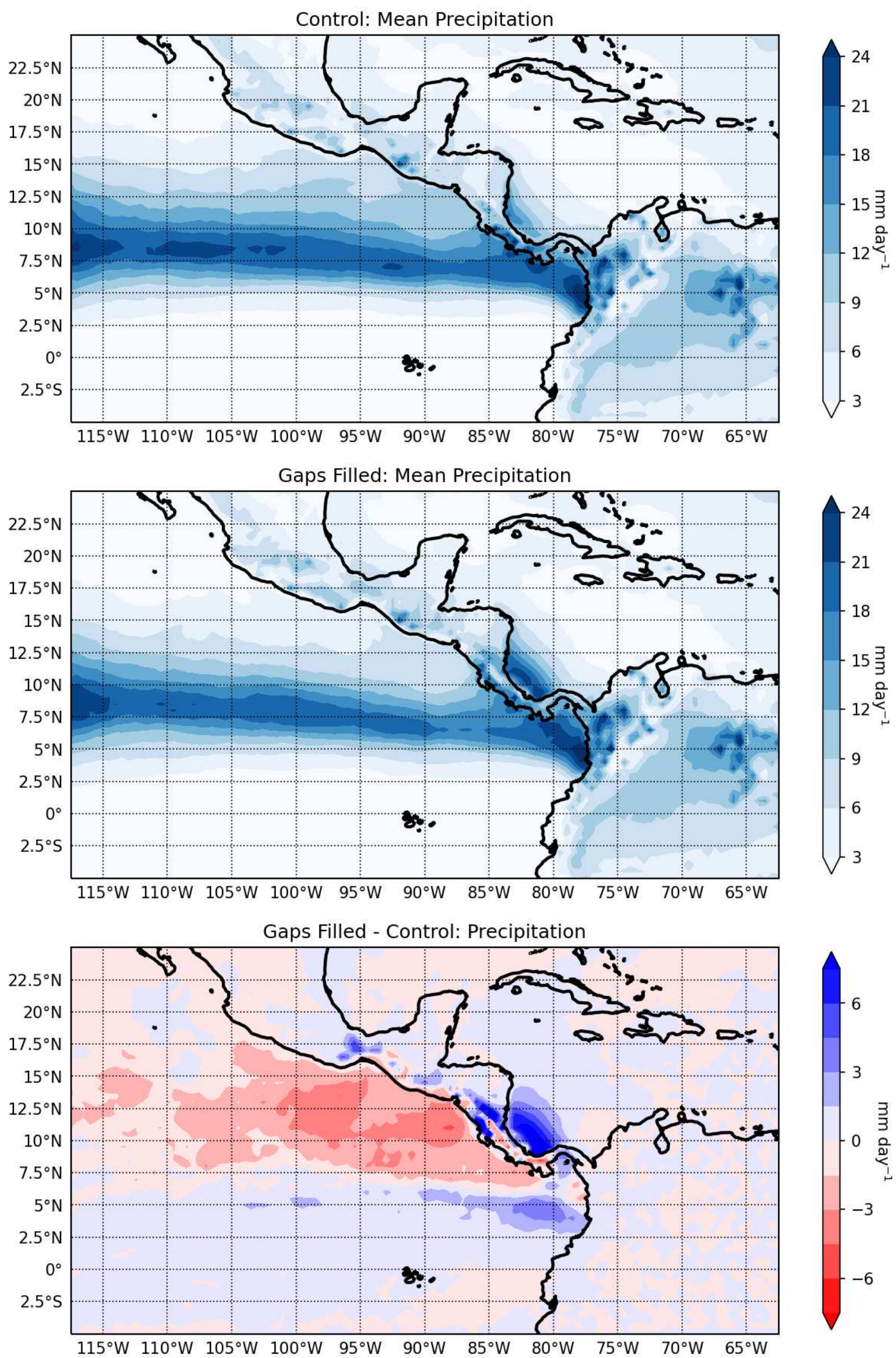

Figure 3.4: June-October mean precipitation rate (mm day^{-1}) for the control (top) and gaps filled (middle) simulations. Precipitation rate differences (gaps filled minus control) are shown in the bottom panel.

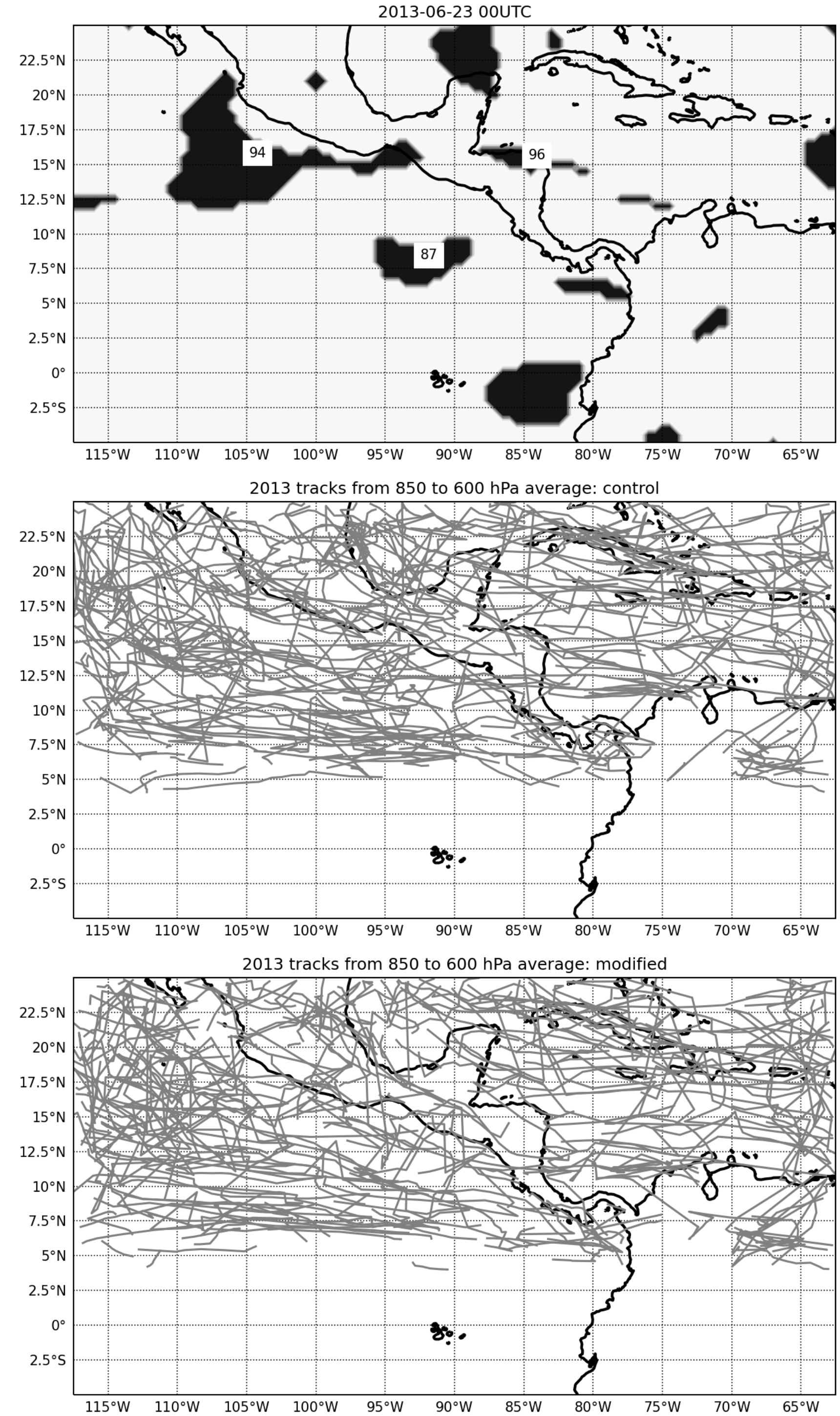

Figure 3.5: Example of the vorticity tracking algorithm. (Top) 850 to 600 hPa labeled vorticity features with values greater than 0.636×10^{-5} s^{-1} on 23 June 2013, 00 UTC in the control run. Easterly wave tracks for June-October 2013 are given for the control run (middle) and gaps filled run (bottom).

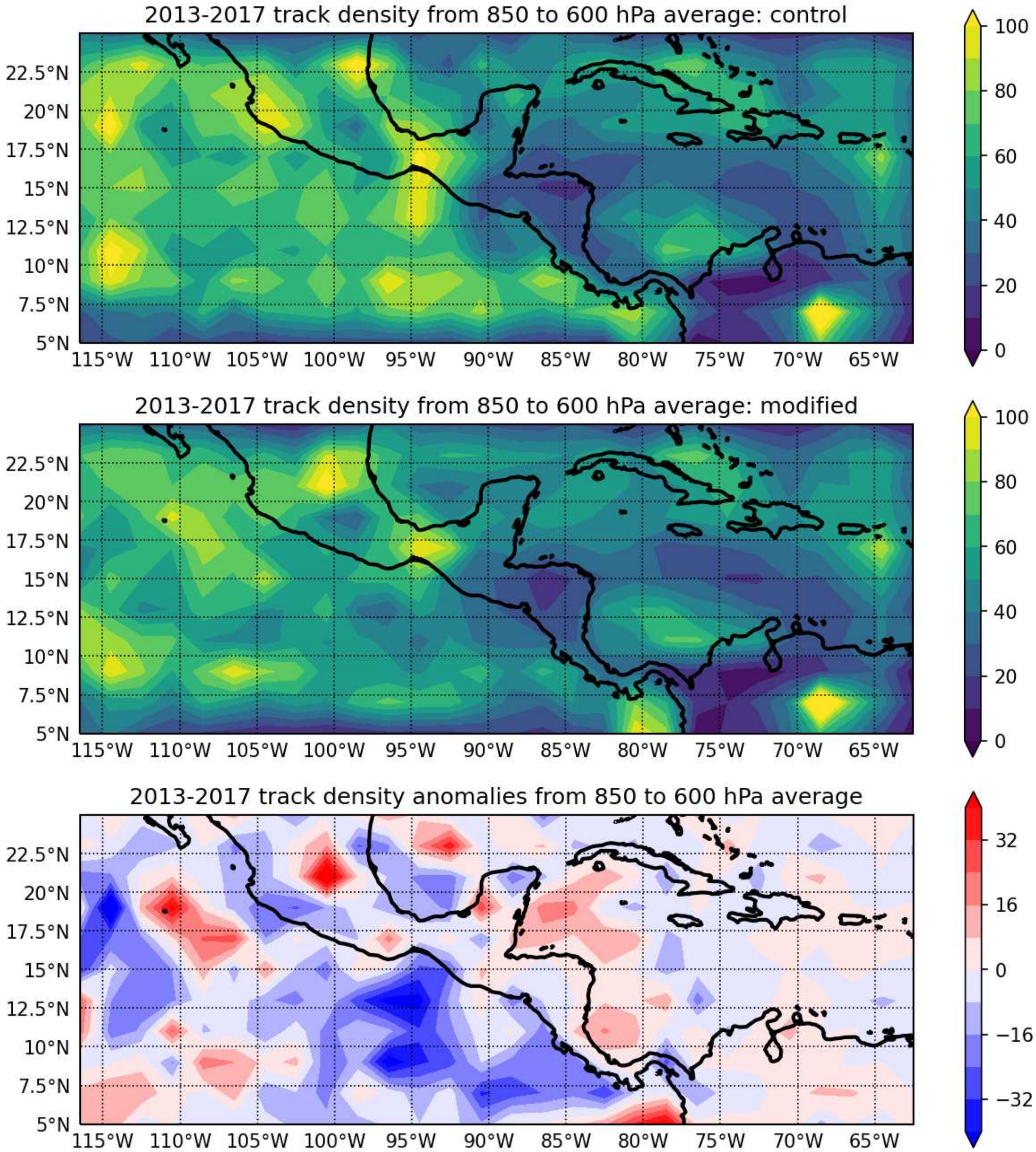

Figure 3.6: Total easterly wave track density for 2013-2017 in the control (top) and gaps filled (middle) runs. Track density differences (gaps filled minus control) are given in the bottom panel. The unit for track density is the total number of tracked vorticity feature centroids that occur per $2^{\circ} \times 2^{\circ}$box.

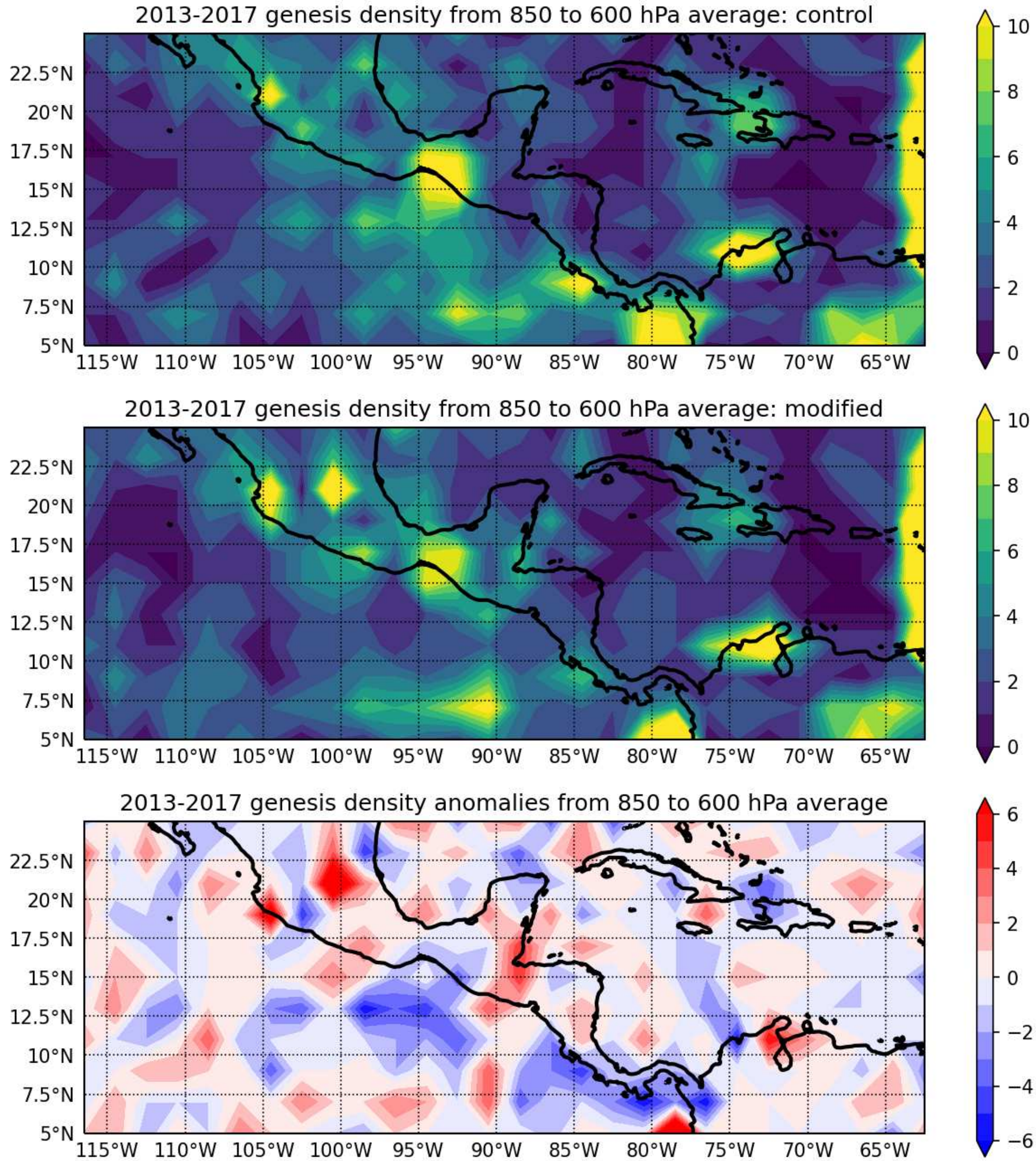

Figure 3.7: Total easterly wave genesis density for 2013-2017 in the control (top) and gaps filled (middle) runs. Genesis density differences (gaps filled minus control) are given in the bottom panel. The unit for genesis density is the total number of easterly wave track genesis points per 2°× 2°box.

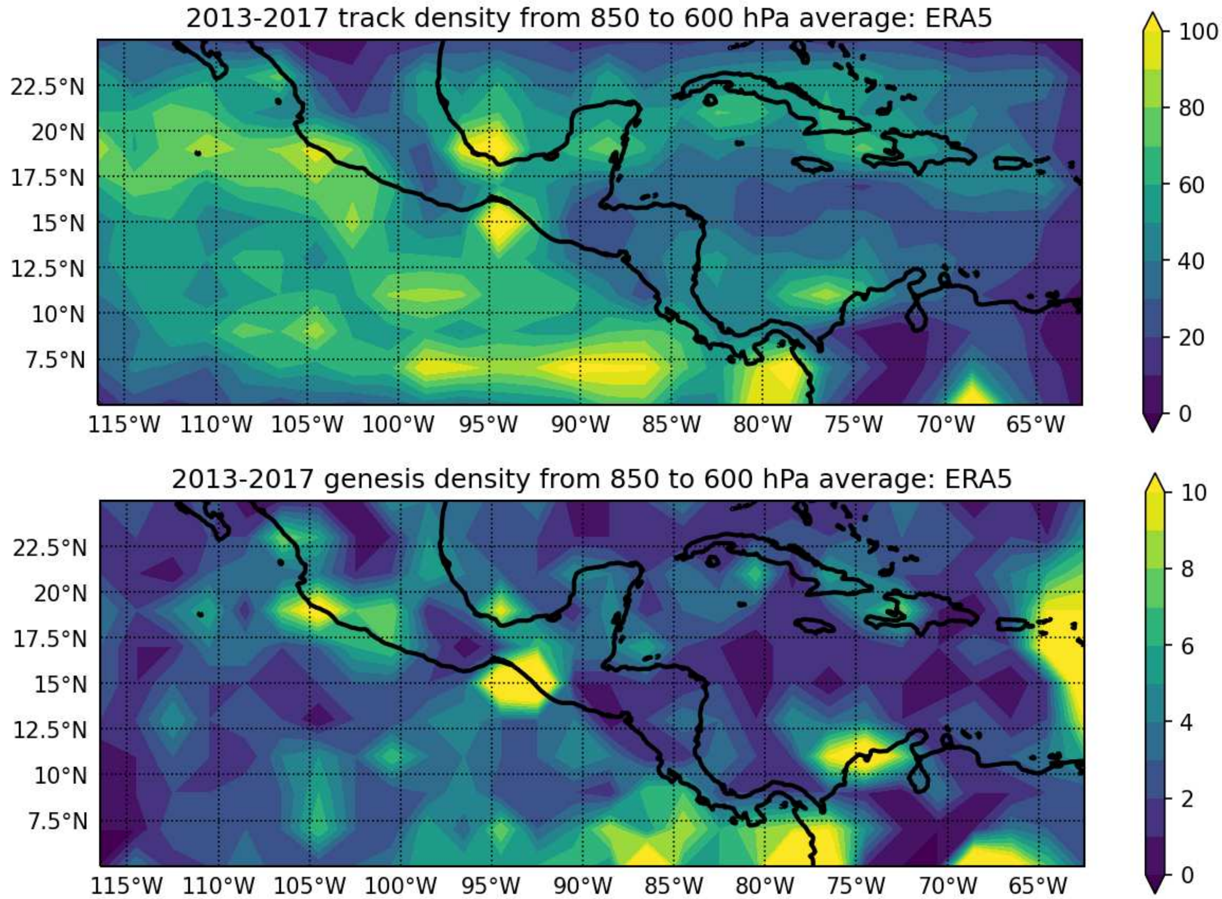

Figure 3.8: Total easterly wave track density (top) and genesis density (bottom) for 2013-2017 in ERA5. The unit for track density is the total number of tracked vorticity feature centroids that occur per $2^\circ \times 2^\circ$box. The unit for genesis density is the total number of easterly wave track genesis points per $2^\circ \times 2^\circ$box.

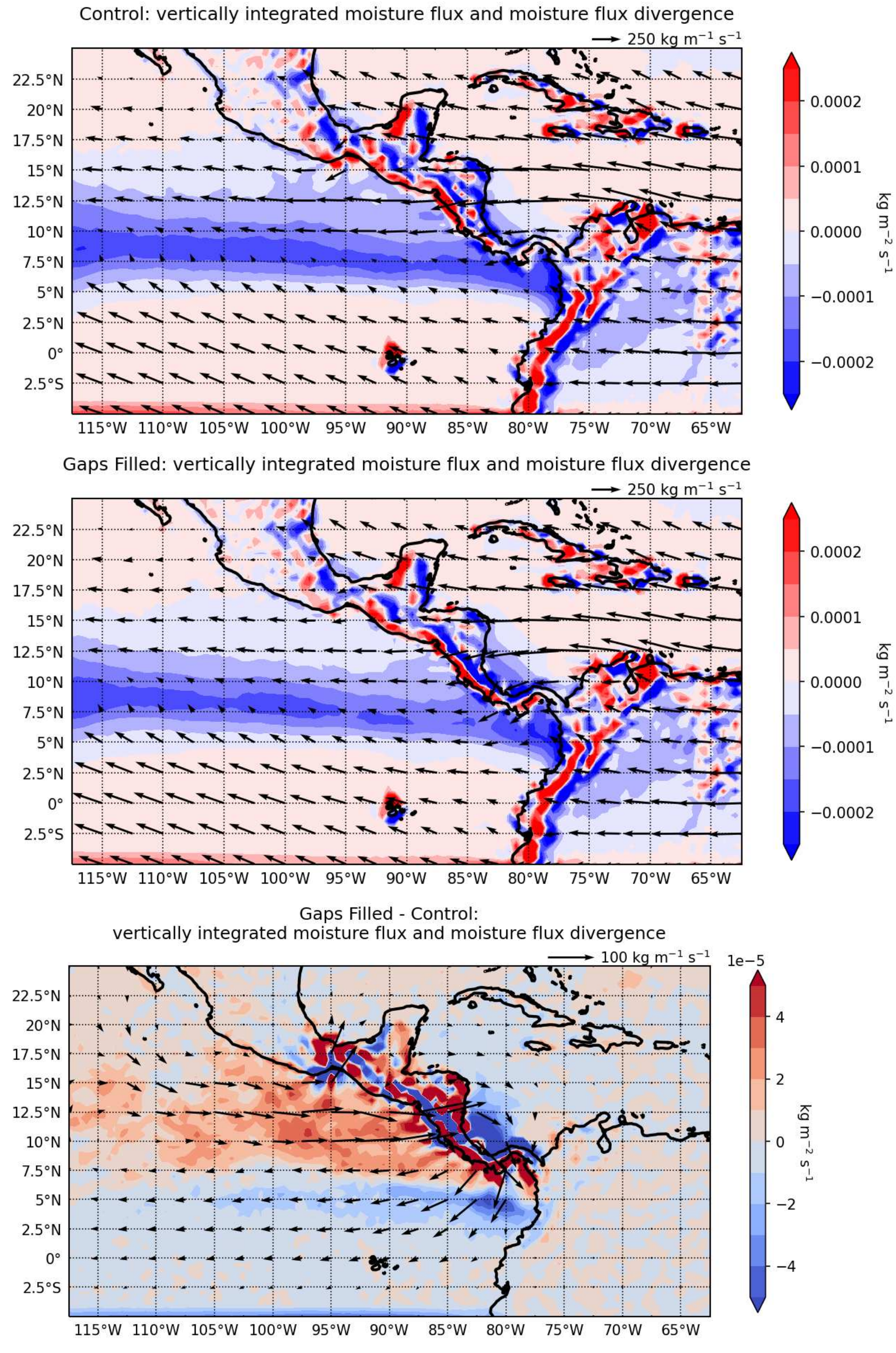

Figure 3.9: June-October mean vertically integrated (1000-200 hPa) moisture flux (kg m^{-1} s^{-1}, vectors) and moisture flux divergence (kg m^{-2} s^{-1}, color contours) for the control (top) and gaps filled (middle) simulations. Differences of these variables (gaps filled minus control) are shown in the bottom panel.

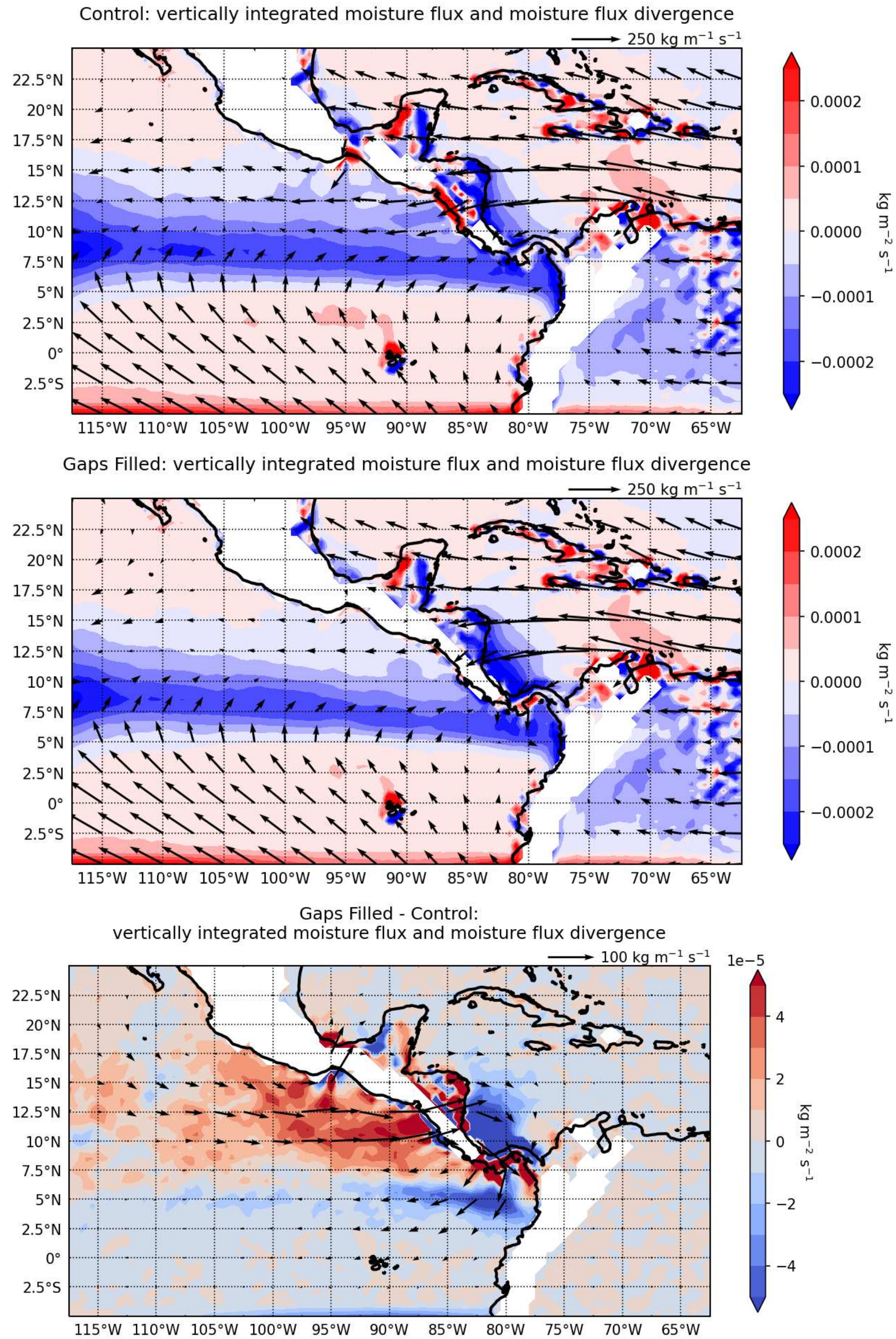

Figure 3.10: June-October mean low-level vertically integrated (1000-800 hPa) moisture flux (kg m^{-1} s^{-1}, vectors) and moisture flux divergence (kg m^{-2} s^{-1}, color contours) for the control (top) and gaps filled (middle) simulations. Differences of these variables (gaps filled minus control) are shown in the bottom panel.

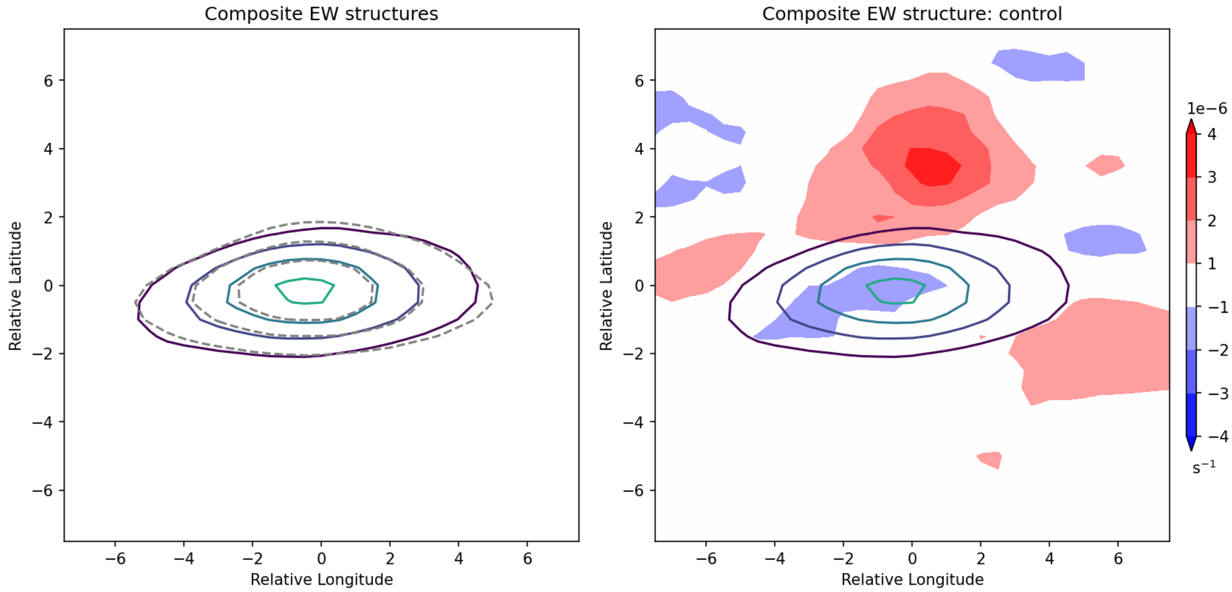

Figure 3.11: Composite easterly wave filtered, unsmoothed, 850-600 hPa vorticity structures (s^{-1}, based on all track observations whose centroid lies within 5-12.5N, 105-85W) across a centered $15° \times 15°$box. (Left) Composite vorticity structures for the control (color contours) and modified (dashed contours) simulations with contours of 5, 10, 15, 20, 25, 30 $\times 10^{-6}$ s^{-1}. (Right) A repeat of the control simulation composite easterly wave contours and the difference of composites between the simulations (gaps filled minus control; filled contours, s^{-1}).

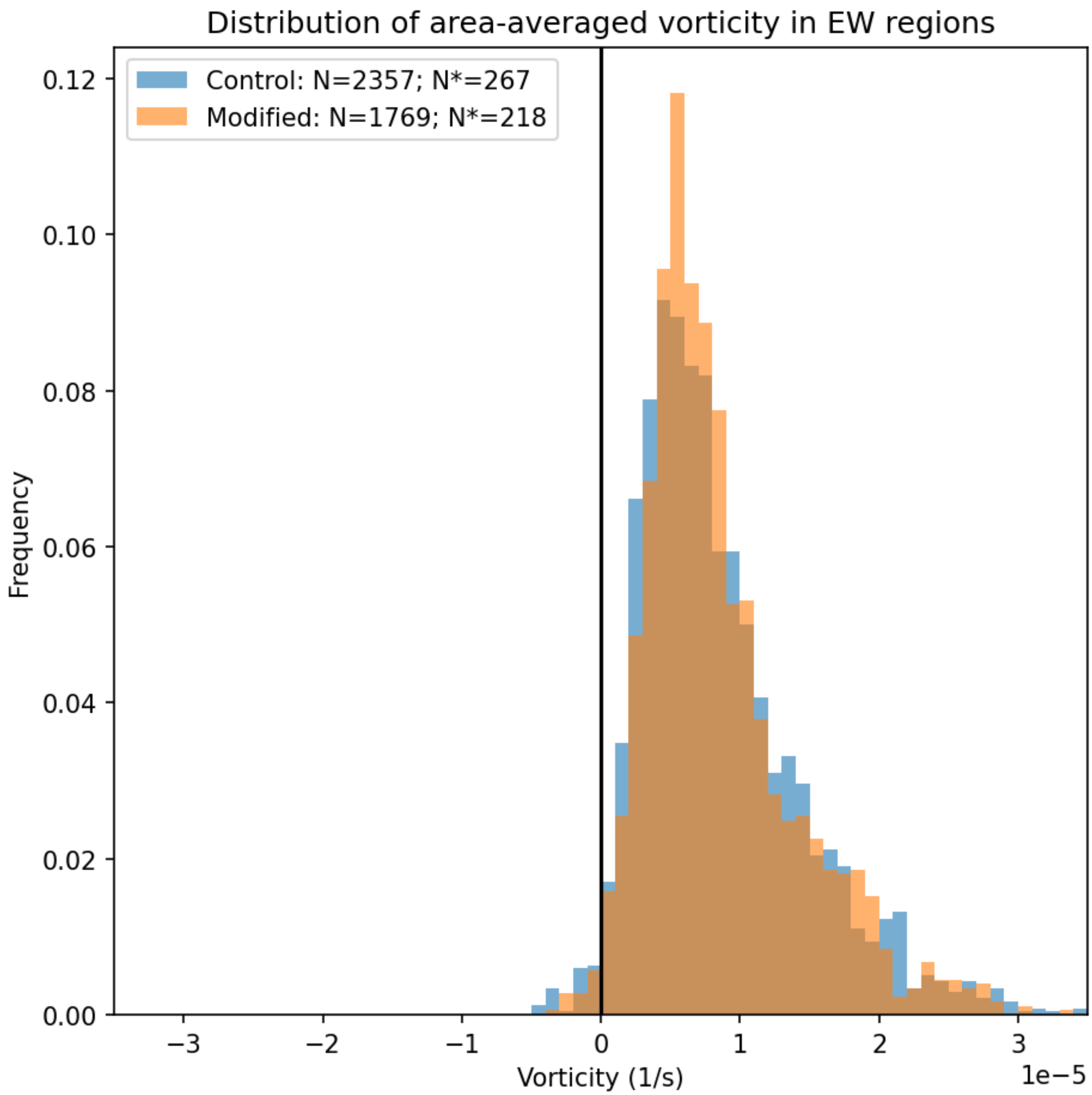

Figure 3.12: Distribution of filtered, unsmoothed, 850-600 hPa vorticity (s^{-1}) that is area-averaged from relative longitudes -4 to 4 and relative latitudes -2 to 2 for the composited easterly wave track observations in the ITCZ. The area-averaged vorticity distribution for the control simulation is in blue, and is in orange for the modified simulation.

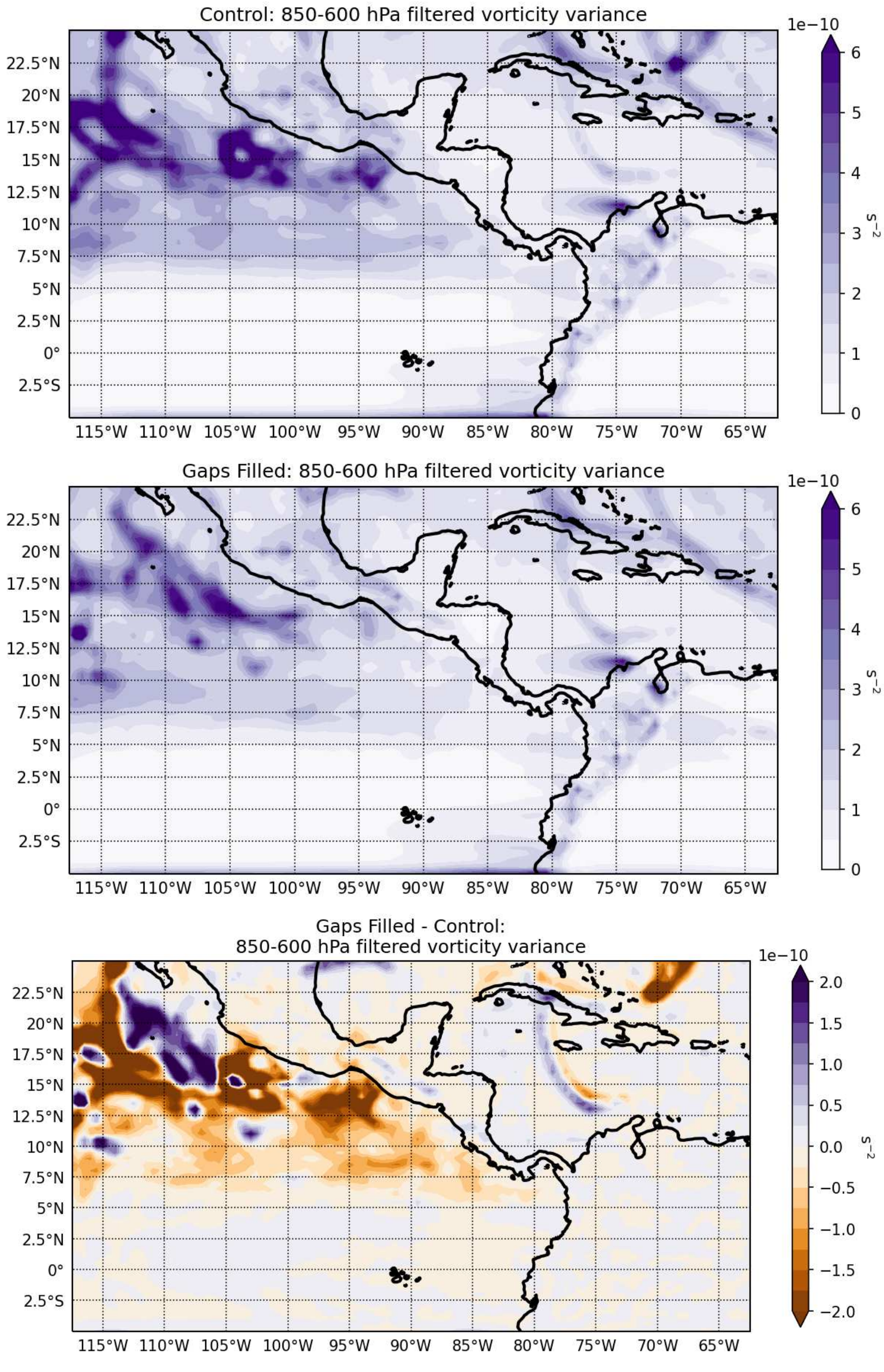

Figure 3.13: Average seasonal June-October filtered, unsmoothed, 850-600 hPa vorticity variance (s^{-2}, color contours) for the control (top) and gaps filled (middle) simulations. Vorticity variance differences (gaps filled minus control) are shown in the bottom panel.

Chapter 4

Eddy Kinetic Energy Budget Analysis for the Control and Gaps Filled Simulations

4.1 Introduction and Methods

In Chapter 3, WRF simulations of a control and gaps filled run showed that the Papagayo and Tehuantepec wind jets support a moister, more convectively active northern half of the east Pacific basin, as well as a 700 hPa positive vorticity region that extends from the Papagayo jet region westward. Further, the presence of these wind jets resulted in higher easterly wave track density compared to the gaps filled run, suggesting that they are important to easterly wave activity in the region. Interestingly, the strength and horizontal structure of ITCZ easterly waves were similar between the simulations, although waves in the control run are slightly more tilted. To provide more context to the Chapter 3 results and to investigate how the growth processes of easterly waves change between the simulations, an eddy kinetic energy (EKE) budget analysis will be performed. EKE budgets have been used to study east Pacific easterly waves in prior work (Maloney and Hartmann, 2001; Serra et al., 2010; Rydbeck and Maloney, 2014; Whitaker and Maloney, 2018), and Whitaker and Maloney (2018) utilized an EKE budget to examine how the strength of the Caribbean low-level jet (CLLJ) impacts the growth of easterly waves.

This analysis will extend on the work from Chapter 3 and will use the data from the afforementioned control and gaps filled WRF simulations. Following prior EKE studies (Rydbeck and Maloney, 2014; Whitaker and Maloney, 2018), the vertically averaged (from 1000 to 200 hPa) easterly wave EKE budget is calculated by:

$$\frac{\partial \overline{EKE}}{\partial t} = -\overline{V_h}\cdot\nabla_h\overline{EKE} - \overline{V_h'\cdot\nabla_h EKE} + \overbrace{\left(-\overline{u'u'}\frac{\partial\overline{u}}{\partial x} - \overline{u'v'}\frac{\partial\overline{u}}{\partial y} - \overline{u'v'}\frac{\partial\overline{v}}{\partial x} - \overline{v'v'}\frac{\partial\overline{v}}{\partial y}\right)}^{\text{Barotropic Conversion}}$$
$$- \nabla\cdot(\overline{V'\Phi'}) \underbrace{-\frac{R}{p}(\overline{\omega' T'})}_{\substack{\text{EAPE to EKE}\\ \text{Conversion}}} + D \tag{4.1}$$

where bars are an 11.25 day running mean and primes are deviations from the running mean. u and v are the zonal and meridional wind, respectively, ω is the vertical pressure velocity, $V =< u, v, \omega >$, $V_h =< u, v >$, $EKE = \frac{1}{2}\left(\overline{u'^2} + \overline{v'^2}\right)$, Φ is the geopotential, $R = 287.058$ J kg^{-1} K^{-1} is the gas constant for dry air, p is the pressure, and T is the temperature. The primary focus of this study will be on changes to EKE and the two labeled budget terms, barotropic conversion and EAPE to EKE conversion. Rydbeck and Maloney (2014) showed that barotropic conversion and EAPE to EKE conversion are the most important budget terms for east Pacific easterly waves, and are respectively related to eddy-mean flow interactions and convective invigoration in the waves. The approach of focusing on these two budget terms is consistent with that of Whitaker and Maloney (2018).

One metric that will be computed in this study is the growth rate related to a specific budget term. For example, the barotropic conversion growth rate is calculated by dividing barotropic conversion by EKE and has units of s^{-1} that are converted to day^{-1}. A higher growth rate signifies that easterly wave disturbances can grow more quickly via that budget term process. Also useful is the reciprocal of the growth rate, which corresponds to the amount of time required for the EKE at a given location to be replenished by a budget term in an easterly wave. Further, to diagnose the relative importance of barotropic conversion and EAPE to EKE conversion to easterly waves in the simulations, absolute value ratios of the budget terms will be calculated. Specifically, the procedure for calculating the absolute value ratio is to first spatially smooth the budget term data using a $\sigma = 1$ Gaussian smoother. Then, the absolute value of the smoothed terms is computed and barotropic conversion is divided by EAPE to EKE conversion. Finally, the ratios are plotted on a nonlinear colorbar to better display the data.

Section 2 of this Chapter will show the EKE budget results, and Section 3 will discuss the results and relate them to the findings from Chapter 3.

4.2 Results

Figure 1 shows the June-October seasonal average (average each season, then average across the seasons) EKE for the control run, gaps filled run, and the difference between the simulations (gaps filled minus control). In both simulations, EKE is the highest at the upper latitudes, which is related to synoptic mid-latitude disturbances. In the control run, elevated EKE can be seen extending westward from around the Papagayo jet region, slightly to the north of the 700 hPa positive vorticity feature seen in Chapter 3, Figure 3. Looking at the difference plot, there is a notable decrease in EKE in the northern half of the basin when the wind jets are blocked, with local minima in difference occuring near the Papagayo and Tehuantepec jet regions. This reduction in EKE is consistent with results in Chapter 3, where easterly wave track density decreases, but the strength of the disturbances remains similar.

Figures 2 and 3 show the average barotropic conversion and the barotropic conversion growth rate, respectively, for both simulations and their difference. Barotropic conversion in the control run peaks in the east Pacific near the Papagayo and Tehuantepec jet regions. The Papagayo jet feature extends further into the basin and lines up reasonably well with the 700 hPa positive vorticity feature in Chapter 3, Figure 3. Barotropic conversion is also high along the Mexican coastline and to the north of the ITCZ on the western side of the basin. The difference plot between the simulations highlights the importance of the wind jets in supporting easterly waves through eddy-mean flow interactions. Negative differences in barotropic conversion are most notable in the same locations described above, near the Tehuantepec and Papagayo jets. Further, the barotropic conversion growth rate (Figure 3) largely resembles the barotropic conversion in Figure 2, and shows that easterly waves grow more quickly by barotropic conversion in the control run than in the gaps filled run. For example, by taking the reciprocal of the growth rate, waves at the core of the control run Papagayo jet could replenish EKE at that location in about $\frac{1}{0.4} = 2.5$ days, as opposed to more than about $\frac{1}{0.1} = 10$ days for easterly waves in the gaps filled run. Thus, blocking the wind jets limits an important source of EKE tendency for developing waves.

Figure 4 shows the average EAPE to EKE conversion, while Figure 5 displays the corresponding growth rate for the budget term. In the east Pacific, control run EAPE to EKE conversion is maximized in the northwest portion of the basin. This location also lines up well with the enhanced filtered vorticity variance observed in Chapter 3, Figure 13, suggesting that this strong EAPE to EKE conversion signal may be related to tropical cyclone activity, as discussed in Chapter 3. It is also important to note the change in the color scale for Figures 4 and 5 versus Figures 2 and 3, showing that in the WRF simulations contributions from EAPE to EKE are generally higher than barotropic conversion, which could be impacted by the fact that convection is parameterized in the model. Positive control run EAPE to EKE conversion is also notable along the ITCZ region, while it is surprisingly negative in the Panama Bight region (also seen in the gaps filled run). Rydbeck and Maloney (2014) and Whitaker and Maloney (2018) both show that the Panama Bight is a region of positive EAPE to EKE conversion, which is related to the convective activity there (Chapter 3, Figures 3 and 4). So, the negative EAPE to EKE conversion in the Panama Bight could signify that the WRF model is struggling to accurately represent mesoscale convective systems in that region. In terms of the difference between the simulations, the blocking of wind jets, and presumably the drier and less convective environment leads to mostly negative difference values in the northern half of the basin. In the ITCZ, differences are on the order of -1 to -4 m^2s^{-3}, while Figure 2 shows that barotropic conversion differences in the Papagayo jet region are also around -1 to -4 m^2s^{-3}.

As was the case for barotropic conversion, the EAPE to EKE growth rate (Figure 5) resembles the EAPE to EKE conversion (Figure 4). In the control run ITCZ, EAPE to EKE growth rates are above 0.2 day^{-1} and are over 0.4 day^{-1} in some places. These growth rates are on par with the core of the Papagayo jet feature in Figure 3, though the EAPE to EKE growth rate values are more widespread and generally higher than for barotropic conversion. In terms of differences, the reduction in EAPE to EKE conversion corresponds to a general reduction in growth rate in the northern part of the basin. While the regions likely impacted by tropical cyclone activity have large growth rate differences, ITCZ difference values range from -0.1 to -0.4 day^{-1}, similar to the core of the Papagayo and Tehuantepec jets in Figure 3. So, in the presence of wind jets, easterly wave timescale disturbances have stronger convective invigoration contributions to their growth than disturbances in the gaps filled run.

Figure 6 shows the absolute value ratios of barotropic conversion to EAPE to EKE conversion, after the terms were spatially smoothed. Barotropic conversion line contours are shown for 1, 3, and 5 $\times 10^{-5}$ m^{2}s^{-3}, and the hatched regions cover these areas. First, in both simulations it is clear that EAPE to EKE is the primary contributor to disturbance growth in the northern half of the basin, with the primary exception of the Papagayo jet region in the control run. Second, in the regions where barotropic conversion is relatively high in both simulations (hatched), the ratios seem to be roughly similar, with the exceptions that the ratio increases near the Mexican coastline and slightly decreases near the ITCZ in the gaps filled run. However, it should also be noted that the presence (or lack thereof) of the wind jets influences the ratio. In the control run, the hatched region of barotropic conversion is much larger, and the ratio is greater than 2 in the Papagayo jet region. In the gaps filled run, there are also ratios greater than 1; however, this is not associated with high overall barotropic conversion values, just that both budget terms are small in this area. Further, on the northern side of the ITCZ, the ratio generally decreases from the control run to the gaps filled run, likely associated with the reduction of barotropic conversion in those regions.

4.3 Discussion

The results from the EKE budget analysis are consistent with the mean state, easterly wave tracking, and easterly wave composite analysis presented in Chapter 3. The blocking of the Papagayo and Tehuantepec wind jets led to a general reduction in EKE, barotropic conversion, EAPE to EKE conversion and their respective growth rates in the northern part of the basin. The reduction of barotropic conversion is linked to the dynamical impact of the jets and matches reasonably well with the 700 hPa vorticity (Chapter 3, Figure 3). The reduction in EAPE to EKE conversion aligns with the reduction in moisture, moisture flux, moisture flux convergence, and convective activity shown in Chapter 3.

The reductions in both of these budget terms as well as EKE brought about by blocking the jets would suggest that either the waves are weaker due to reduced energy conversion, or that fewer conversions are occurring in general. To this end, the Chapter 3 analysis suggests that the waves in the ITCZ are of similar strength, but that fewer waves occur. Thus, if fewer waves are occurring with similar strength, then the reductions in barotropic conversion, EAPE to EKE, and EKE between the simulations could at least in part be a consequence of fewer waves developing in general in a less favorable environment. However, this statement may not apply quite as much for barotropic conversion since the mean state flow is being altered; more work will need to be done to address why easterly wave activity, the budget terms, and EKE decrease while the strength of the waves are similar. Finally, the slight change in wave tilt in the composite analysis (Chapter 3, Figure 11) seems consistent with the reduction in barotropic conversion between the simulations, though not as drastic as the changes to the budget term.

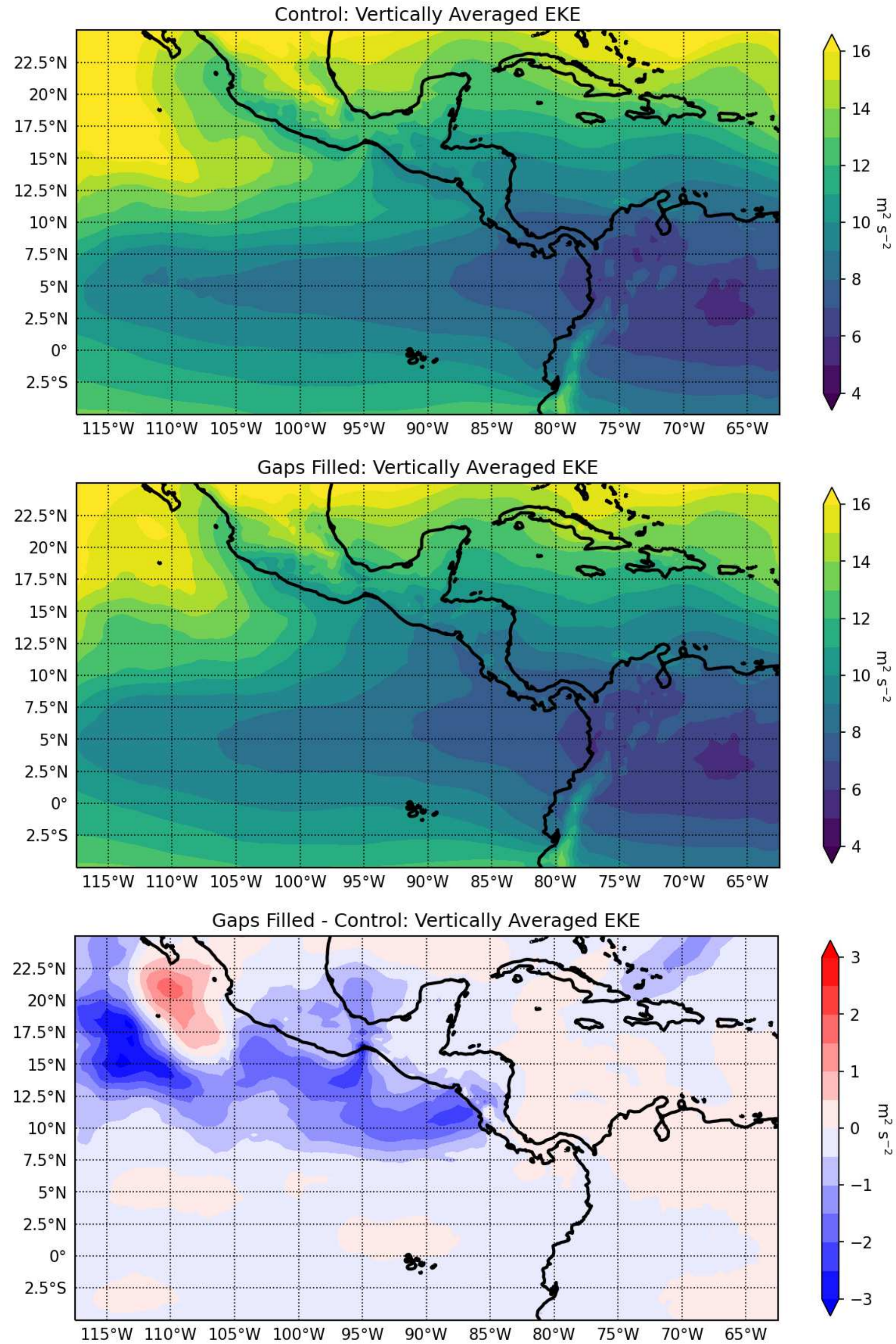

Figure 4.1: June-October vertically averaged eddy kinetic energy (m^2s^{-2}) for the (top) control run, (middle) gaps filled run, and (bottom) the gaps filled minus control difference.

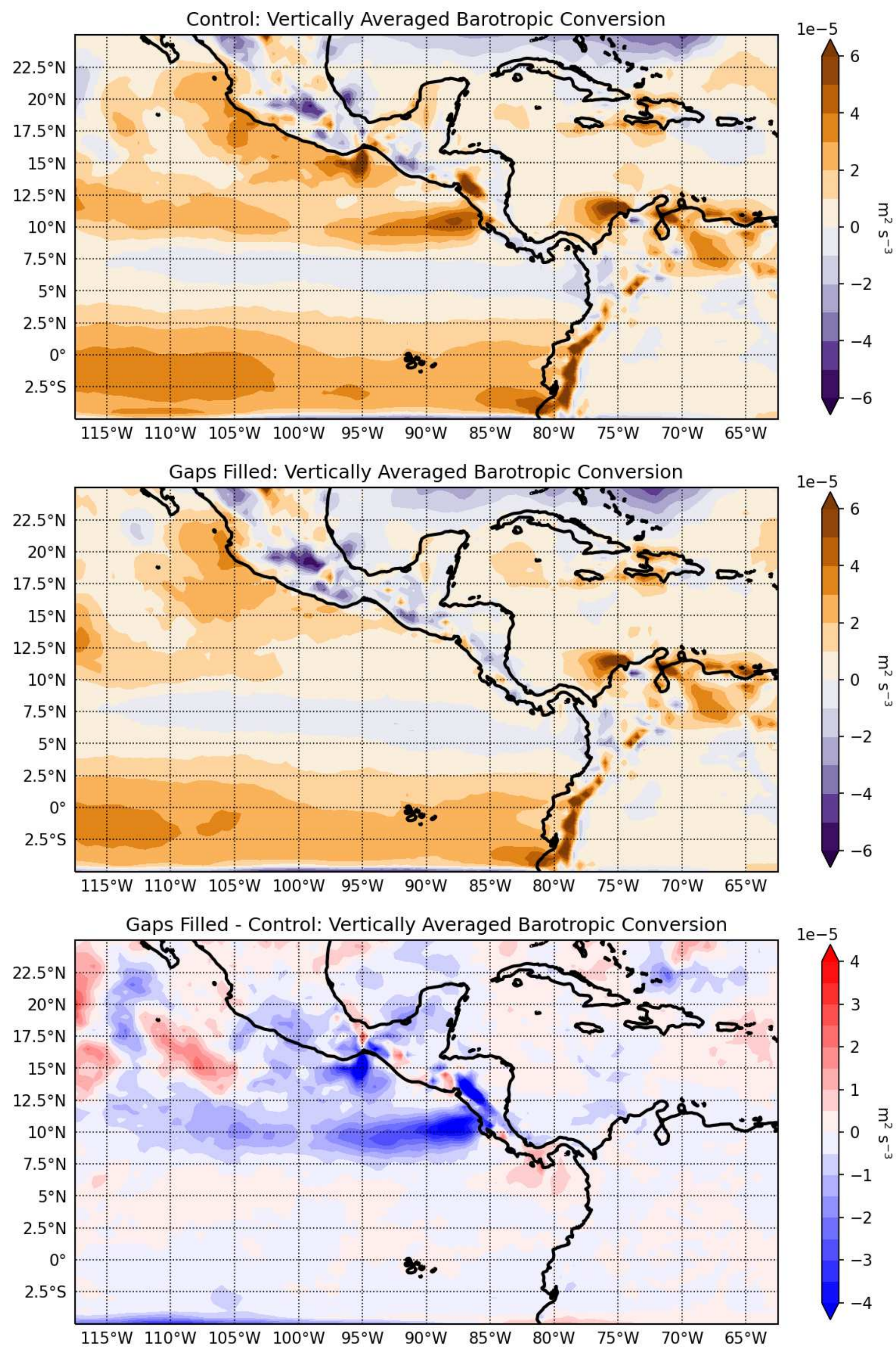

Figure 4.2: June-October vertically averaged barotropic conversion (m^2s^{-3}) for the (top) control run, (middle) gaps filled run, and (bottom) the gaps filled minus control difference.

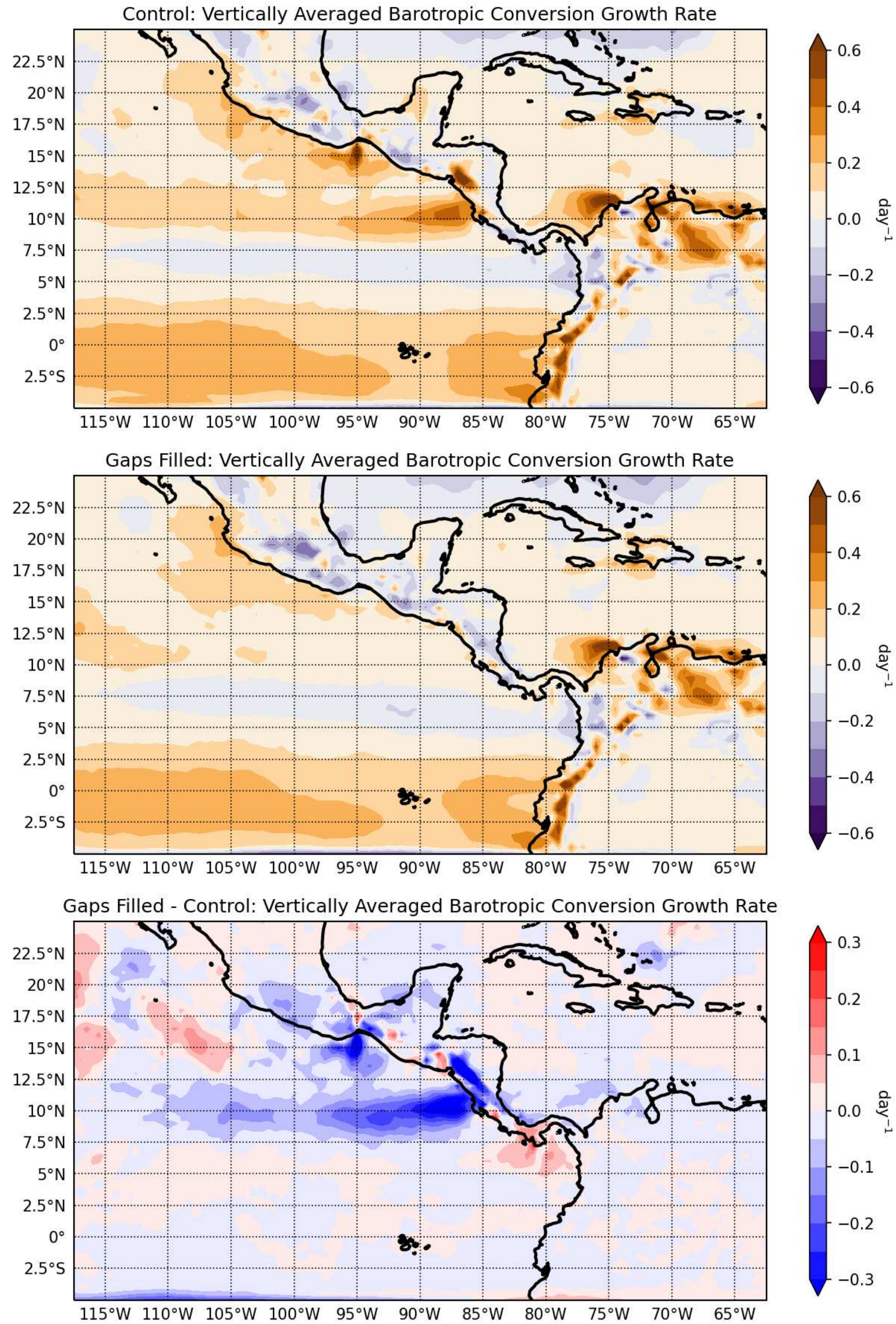

Figure 4.3: June-October vertically averaged barotropic conversion growth rate (day^{-1}) for the (top) control run, (middle) gaps filled run, and (bottom) the gaps filled minus control difference.

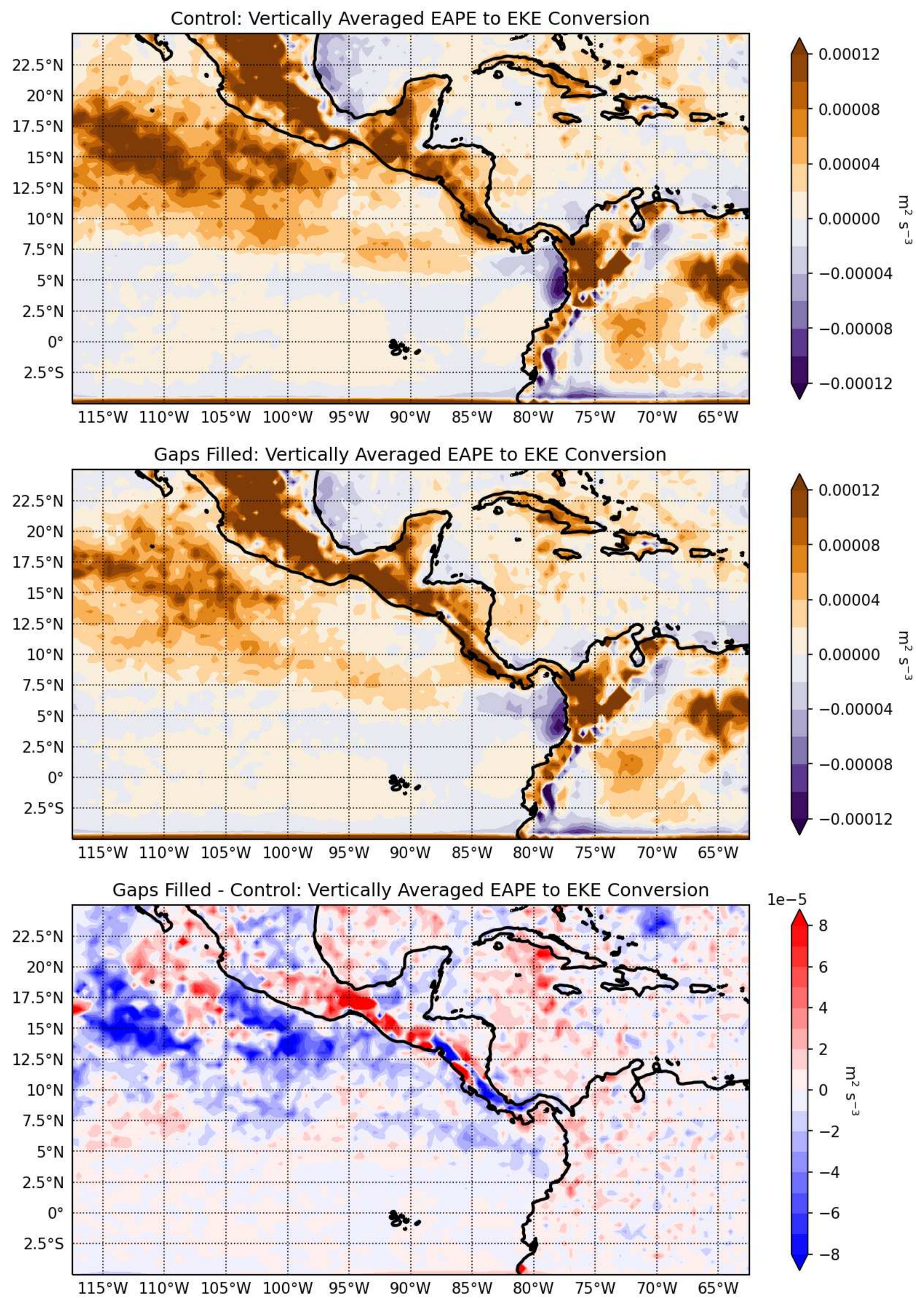

Figure 4.4: June-October vertically averaged EAPE to EKE conversion (m^2s^{-3}) for the (top) control run, (middle) gaps filled run, and (bottom) the gaps filled minus control difference.

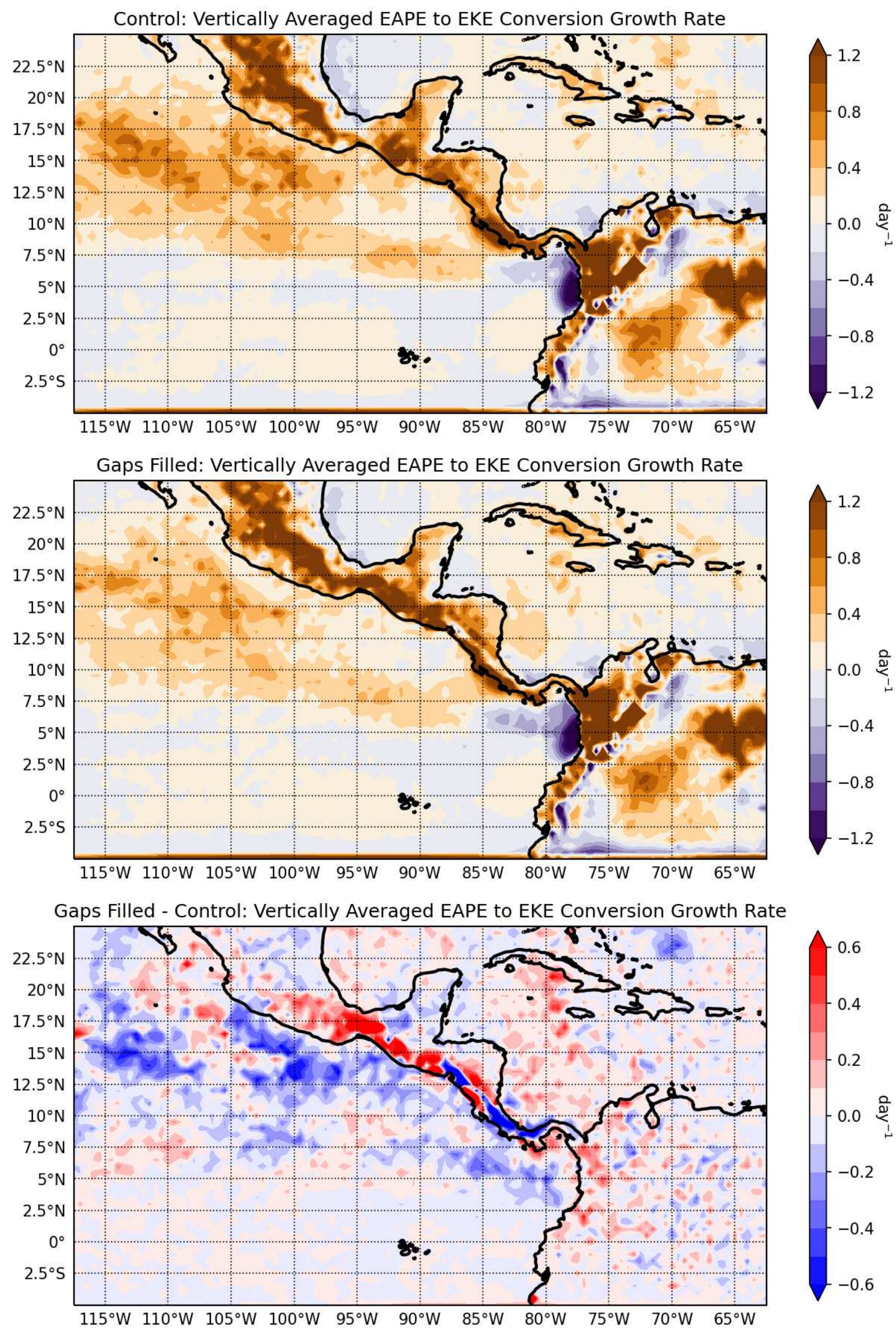

Figure 4.5: June-October vertically averaged EAPE to EKE conversion growth rate (day^{-1}) for the (top) control run, (middle) gaps filled run, and (bottom) the gaps filled minus control difference.

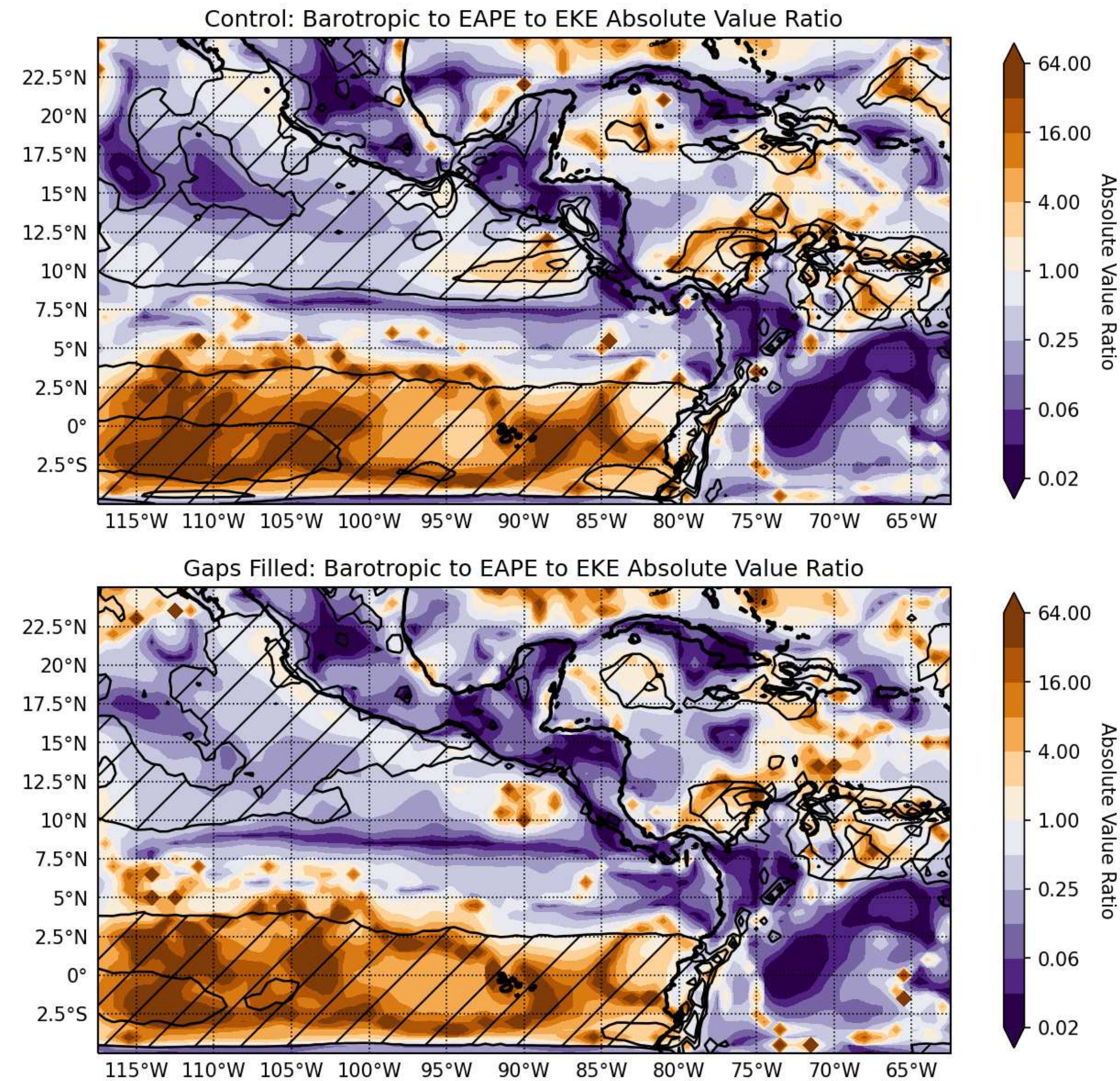

Figure 4.6: June-October vertically averaged barotropic conversion to EAPE to EKE conversion absolute value ratio for the (top) control run and (bottom) gaps filled run. Line contours are barotropic conversion at 1,3,5 $\times 10^{-5}$ m^2s^{-3}, and hatching encompasses these regions. The budget terms are spatially smoothed before the absolute value ratio is calculated.

Chapter 5

Conclusions and Future Work

In Chapter 2, it was found that convection (via vortex stretching) is very important to the growth of a Panama Bight MCS into an easterly wave in a high-resolution WRF model simulation. In particular, top-heavy vertical profiles, associated with stratiform precipitation, were present during the disturbance's evolution and supported the strengthening of a mid-level vortex. Overall, the model results compared reasonably well with ERA5 reanalysis, although there were differences in the vertical structures of the disturbances. For example, the disturbance in ERA5 tended to be less top-heavy than in WRF. The analysis also suggested that the ERA5 disturbance may be interacting with the Papagayo jet around the time that the easterly wave formed, while this does not appear to be the case in WRF.

To test the interactions between easterly waves and the Papagayo and Tehuantepec wind jets, Chapters 3 and 4 utilize WRF simulations that consist of a control run and a gaps filled run that blocks these wind jets. The Papagayo and Tehuantepec wind jets help provide moisture to the northern half of the east Pacific basin, which supports convective activity and precipitation. Additionally, a 700 hPa positive vorticity feature that extends westward from the Papagayo jet region and just to the north of the ITCZ weakens in the modified topography simulation. From a developed easterly wave tracking algorithm, it is shown that easterly wave track density generally decreases as a result of blocking the wind jets and the associated mean state changes. Further, a composite analysis of ITCZ easterly waves shows that control run waves are slightly more tilted, suggesting stronger barotropic growth (e.g., Rydbeck and Maloney, 2014). However, the composite analysis also finds that the easterly waves in both simulations are around the same strength, contrasting with the notable differences mentioned earlier. Chapter 4 continues the easterly wave analysis by calculating an easterly wave EKE budget for each simulation. Comparing the budgets shows that blocking the wind jets leads to a reduction in EKE, barotropic conversion, and EAPE to EKE conversion, suggesting some combination of the waves being weaker and that there are fewer waves in the gaps filled run. Overall, the Papagayo and Tehuantepec wind jets support the energy budget of easterly waves, likely more directly through barotropic conversion (as it is related to eddy-mean flow interactions) and more indirectly through EAPE to EKE conversion.

From this dissertation, future work could examine the Panama Bight MCS to easterly wave genesis pathway and easterly wave-wind jet interactions in more detail. To do this, databases of events for both topics would need to be created, likely using satellite and reanalysis data. For the genesis pathway, identified successful events would need to be compared against data from all other Panama Bight MCSs to provide a sense of the frequency of occurrence and to investigate potential differences in environmental conditions. Further, the MCS to easterly wave events could then be compared with tropical cyclone data to determine how often this easterly wave genesis pathway results in tropical cyclogenesis. For easterly wave-wind jet interactions, the events could be composited together and analyzed with a vorticity budget to quantify the impact of wind jets on easterly wave vorticity. Further, the number of easterly wave-wind jet events in a given season could be compared with the results of Holbach and Bourassa (2014) to provide additional context to how frequently this process occurs. Finally, for both event datasets, the seasonality of the events could be determined along with investigating whether these processes are influenced by phenomena like the Madden-Julian Oscillation.

Bibliography

Adames, A. F., and Y. Ming, 2018: Interactions between Water Vapor and Potential Vorticity in Synoptic-Scale Monsoonal Disturbances: Moisture Vortex Instability. *J. Atmos. Sci.*, **75 (6)**, 2083–2106.

Allan, D. B., T. Caswell, N. C. Keim, and C. M. van der Wel, 2019: Trackpy v0.4.2. Zenodo. doi:10.5281/zenodo.3492186, URL github.com/soft-matter/trackpy.

Amador, J. A., 2008: The Intra-Americas Sea Low-level Jet. *Annals of the New York Academy of Sciences*, **1146 (1)**, 153–188, doi:10.1196/annals.1446.012.

Chelton, D. B., M. H. Freilich, and S. K. Esbensen, 2000: Satellite Observations of the Wind Jets off the Pacific Coast of Central America. Part I: Case Studies and Statistical Characteristics. *Monthly Weather Review*, **128 (7)**, 1993–2018, doi:10.1175/1520-0493(2000)128<1993:SOOTWJ>2.0.CO;2.

Collins, W. D., P. J. Rasch, B. A. Boville, J. J. Hack, J. R. McCaa, D. L. Williamson, J. T. Kiehl, and B. Briegleb, 2004: Description of the NCAR Community Atmosphere Model (CAM 3.0). NCAR Tech. Note NCAR/TN–464+STR, 214 pp.

Copernicus Climate Change Service (C3S), 2017: ERA5: Fifth generation of ECMWF atmospheric reanalyses of the global climate. Copernicus Climate Change Service Climate Data Store (CDS), *Accessed in 2019*, URL https://cds.climate.copernicus.eu/cdsapp#!/home.

Crosbie, E., and Y. Serra, 2014: Intraseasonal Modulation of Synoptic-Scale Disturbances and Tropical Cyclone Genesis in the Eastern North Pacific. *J. Climate*, **27**, 5724–5745.

Dominguez, C., J. M. Done, and C. L. Bruyère, 2020: Easterly wave contributions to seasonal rainfall over the tropical Americas in observations and a regional climate model. *Climate Dynamics*, **54 (1)**, 191–209, doi:10.1007/s00382-019-04996-7.

Dunkerton, T. J., M. T. Montgomery, and Z. Wang, 2009: Tropical cyclogenesis in a tropical wave critical layer: easterly waves. *Atmos. Chem. Phys.*, **9**, 5587–5646.

Feng, Z., L. R. Leung, R. A. Houze Jr., S. Hagos, J. Hardin, Q. Yang, B. Han, and J. Fan, 2018: Structure and Evolution of Mesoscale Convective Systems: Sensitivity to Cloud Microphysics in Convection-Permitting Simulations Over the United States. *Journal of Advances in Modeling Earth Systems*, **10 (7)**, 1470–1494, doi:10.1029/2018MS001305, URL https://agupubs.onlinelibrary.wiley.com/doi/abs/10.1029/2018MS001305, https://agupubs.onlinelibrary.wiley.com/doi/pdf/10.1029/2018MS001305.

Ferreira, R. N., and W. H. Schubert, 1997: Barotropic Aspects of ITCZ Breakdown. *J. Atmos. Sci.*, **54**, 261–285.

Frank, N. L., 1970: Atlantic tropical systems of 1969. *Mon. Wea. Rev.*, **98**, 307–314.

Fu, D., P. Chang, and C. M. Patricola, 2017: Intrabasin Variability of East Pacific Tropical Cyclones During ENSO Regulated by Central American Gap Winds. *Scientific Reports*, **7 (1)**, 1658.

Fu, D., P. Chang, C. M. Patricola, R. Saravanan, X. Liu, and H. E. Beck, 2021: Central American mountains inhibit eastern North Pacific seasonal tropical cyclone activity. *Nature Communications*, **12 (1)**, 4422.

Fuchs-Stone, Z., D. J. Raymond, and S. Sentic, 2020: Otrec2019: Convection over the east pacific and southwest caribbean. *Geophysical Research Letters*, **47 (11)**, e2020GL087 564, doi:10.1029/2020GL087564.

Han, J., and H.-L. Pan, 2011: Revision of Convection and Vertical Diffusion Schemes in the NCEP Global Forecast System. *Weather and Forecasting*, **26 (4)**, 520 – 533, doi:10.1175/WAF-D-10-05038.1, URL https://journals.ametsoc.org/view/journals/wefo/26/4/waf-d-10-05038_1.xml.

Heikenfeld, M., P. J. Marinescu, M. Christensen, D. Watson-Parris, F. Senf, S. C. van den Heever, and P. Stier, 2019: tobac 1.2: towards a flexible framework for tracking and analysis of clouds in diverse datasets. *Geoscientific Model Development*, **12 (11)**, 4551–4570, doi:10.5194/gmd-12-4551-2019, URL https://gmd.copernicus.org/articles/12/4551/2019/.

Hersbach, H., and Coauthors, 2018: ERA5 hourly data on single levels from 1979 to present. Copernicus Climate Change Service (C3S) Climate Data Store (CDS). (Accessed in 2019). doi: 10.24381/cds.adbb2d47.

Holbach, H. M., and M. A. Bourassa, 2014: The Effects of Gap-Wind-Induced Vorticity, the Monsoon Trough, and the ITCZ on East Pacific Tropical Cyclogenesis. *Mon. Wea. Rev.*, **142 (3)**, 1312–1325.

Hong, S.-Y., and J.-O. J. Lim, 2006: The WRF Single-Moment 6-Class Microphysics Scheme (WSM6). *J. Korean Meteor. Soc.*, **42**, 129 – 151.

Hong, S.-Y., Y. Noh, and J. Dudhia, 2006: A New Vertical Diffusion Package with an Explicit Treatment of Entrainment Processes. *Mon. Wea. Rev.*, **134 (9)**, 2318–2341.

Houze, R. A., 2004: Mesoscale convective systems. *Rev. Geophys.*, **42 (4)**.

Huaman, L., E. D. Maloney, C. Schumacher, and G. N. Kiladis, 2021: Easterly waves in the East Pacific during the OTREC 2019 field campaign. *J. Atmos. Sci.*, submitted.

Joyce, R. J., J. E. Janowiak, P. A. Arkin, and P. Xie, 2004: CMORPH: A Method that Produces Global Precipitation Estimates from Passive Microwave and Infrared Data at High Spatial and Temporal Resolution. *J. Hydrometeor.*, **5 (3)**, 487–503.

Kerns, B., K. Greene, and E. Zipser, 2008: Four Years of Tropical ERA-40 Vorticity Maxima Tracks. Part I: Climatology and Vertical Vorticity Structure. *Mon. Wea. Rev.*, **136 (11)**, 4301–4319.

Maloney, E. D., and S. K. Esbensen, 2007: Satellite and Buoy Observations of Boreal Summer Intraseasonal Variability in the Tropical Northeast Pacific. *Monthly Weather Review*, **135 (1)**, 3–19, doi:10.1175/MWR3271.1.

Maloney, E. D., and D. L. Hartmann, 2000: Modulation of Eastern North Pacific Hurricanes by the Madden-Julian Oscillation. *J. Climate*, **13**, 1451–1460.

Maloney, E. D., and D. L. Hartmann, 2001: The Madden-Julian Oscillation, Barotropic Dynamics, and North Pacific Tropical Cyclone Formation. Part I: Observations. *J. Atmos. Sci.*, **58**, 2545–

2558.

Mapes, B. E., T. T. Warner, and M. Xu, 2003a: Diurnal Patterns of Rainfall in Northwestern South America. Part III: Diurnal Gravity Waves and Nocturnal Convection Offshore. *Mon. Wea. Rev.*, **131**, 830–844.

Mapes, B. E., T. T. Warner, M. Xu, and A. J. Negri, 2003b: Diurnal Patterns of Rainfall in Northwestern South America. Part I: Observations and Context. *Mon. Wea. Rev.*, **131**, 799–812.

Mestas-Nuñez, A. M., D. B. Enfield, and C. Zhang, 2007: Water Vapor Fluxes over the Intra-Americas Sea: Seasonal and Interannual Variability and Associations with Rainfall. *Journal of Climate*, **20 (9)**, 1910–1922, doi:10.1175/JCLI4096.1.

Molinari, J., D. Knight, M. Dickinson, D. Vollaro, and S. Skubis, 1997: Potential Vorticity, Easterly Waves, and Eastern Pacific Tropical Cyclogenesis. *Mon. Wea. Rev.*, **125**, 2699–2708.

Molinari, J., and D. Vollaro, 2000: Planetary- and Synoptic-Scale Influences on Eastern Pacific Tropical Cyclogenesis. *Mon. Wea. Rev.*, **128**, 3296–3307.

Mozer, J. B., and J. A. Zehnder, 1996: Lee vorticity Production by Large-Scale Tropical Mountain Ranges. Part I: Eastern North Pacific Tropical Cyclogenesis. *J. Atmos. Sci.*, **53 (4)**, 521–538.

Mundhenk, B. D., E. A. Barnes, and E. D. Maloney, 2016: All-Season Climatology and Variability of Atmospheric River Frequencies over the North Pacific. *Journal of Climate*, **29 (13)**, 4885 – 4903, doi:10.1175/JCLI-D-15-0655.1.

Pasch, R. J., and D. A. Zelinsky, 2012: Tropical Cyclone Report Hurricane Carlotta (EP032012) 14-16 June 2012. National Hurricane Center. 13 pp, URL https://www.nhc.noaa.gov/data/tcr/EP032012_Carlotta.pdf.

Pasch, R. J., and Coauthors, 2009: Eastern North Pacific hurricane season of 2006. *Mon. Wea. Rev.*, **137**, 3–20.

Perdigón-Morales, J., R. Romero-Centeno, P. Ordoñez, R. Nieto, L. Gimeno, and B. S. Barrett, 2021: Influence of the Madden-Julian Oscillation on moisture transport by the Caribbean Low Level Jet during the Midsummer Drought in Mexico. *Atmospheric Research*, **248**, 105 243, doi:

https://doi.org/10.1016/j.atmosres.2020.105243, URL https://www.sciencedirect.com/science/article/pii/S0169809520311807.

Petersen, W. A., R. Cifelli, D. J. Boccippio, S. A. Rutledge, and C. Fairall, 2003: Convection and Easterly Wave Structures Observed in the Eastern Pacific Warm Pool during EPIC-2001. *J. Atmos. Sci*, **60**, 1754–1773.

Poveda, G., and O. J. Mesa, 2000: On the Existence of Lloro (the Rainiest Locality on Earth): Enhanced Ocean-Land-Atmosphere Interaction by a Low Level Jet. *Geophys. Res. Lett.*, **27**, 1675–1678.

Rasmussen, K. L., and R. A. Houze, 2016: Convective Initiation near the Andes in Subtropical South America. *Monthly Weather Review*, **144 (6)**, 2351–2374, doi:10.1175/MWR-D-15-0058.1, URL https://doi.org/10.1175/MWR-D-15-0058.1, https://doi.org/10.1175/MWR-D-15-0058.1.

Romero-Centeno, R., J. Zavala-Hidalgo, and G. B. Raga, 2007: Midsummer Gap Winds and Low-Level Circulation over the Eastern Tropical Pacific. *Journal of Climate*, **20 (15)**, 3768–3784, doi:10.1175/JCLI4220.1.

Rydbeck, A. V., and E. D. Maloney, 2014: Energetics of East Pacific Easterly Waves during Intraseasonal Events. *J. Climate*, **27**, 7603–7621.

Rydbeck, A. V., and E. D. Maloney, 2015: On the Convective Coupling and Moisture Organization of East Pacific Easterly Waves. *J. Atmos. Sci.*, **72**, 3850–3870.

Rydbeck, A. V., E. D. Maloney, and G. J. Alaka, 2017: In Situ Initiation of East Pacific Easterly Waves in a Regional Model. *J. Atmos. Sci.*, **74**, 333–351.

Schultz, D. M., W. E. Bracken, L. F. Bosart, G. J. Hakim, M. A. Bedrick, M. J. Dickinson, and K. R. Tyle, 1997: The 1993 superstorm cold surge: Frontal structure, gap flow, and tropical impact. *Monthly Weather Review*, **125 (1)**, 5–39, doi:10.1175/1520-0493(1997)125<0005:TSCSFS>2.0.CO;2.

Serra, Y. L., G. N. Kiladis, and M. F. Cronin, 2008: Horizontal and Vertical Structure of Easterly Waves in the Pacific ITCZ. *J. Atmos. Sci.*, **65**, 1266–1284.

Serra, Y. L., G. N. Kiladis, and K. I. Hodges, 2010: Tracking and Mean Structure of Easterly Waves over the Intra-Americas Sea. *J. Climate*, **23**, 4823–4840.

Shapiro, L. J., 1986: The Three Dimensional Structure of Synoptic-Scale Disturbances over the Tropical Atlantic. *Mon. Wea. Rev.*, **114**, 1876–1891.

Skamarock, W. C., and Coauthors, 2008: A Description of the Advanced Research WRF Version 3. NCAR Tech. Note NCAR/TN–475+STR, 113 pp, doi:10.5065/D68S4MVH.

Tewari, M., and Coauthors, 2004: Implementation and verification of the unified NOAH land surface model in the WRF model. *20th conference on weather analysis and forecasting/16th conference on numerical weather prediction*, pp. 11–15, 14.2A, URL http://www2.mmm.ucar.edu/wrf/users/phys_refs/LAND_SURFACE/noah.pdf.

Thompson, G., P. R. Field, R. M. Rasmussen, and W. D. Hall, 2008: Explicit Forecasts of Winter Precipitation Using an Improved Bulk Microphysics Scheme. Part II: Implementation of a New Snow Parameterization. *Mon. Wea. Rev.*, **136 (12)**, 5095–5115.

Thorncroft, C., and K. Hodges, 2001: African Easterly Wave Variability and Its Relationship to Atlantic Tropical Cyclone Activity. *J. Climate*, **14**, 1166–1179.

Thorncroft, C. D., N. M. J. Hall, and G. N. Kiladis, 2008: Three-Dimensional Structure and Dynamics of African Easterly Waves. Part III: Genesis. *J. Atmos. Sci.*, **65**, 3596–3607.

Toma, V. E., and P. J. Webster, 2010: Oscillations of the Intertropical Convergence Zone and the genesis of easterly waves. Part I: diagnostics and theory. *Clim. Dyn.*, **34**, 587–604.

Torres, V. M., and C. D. Thorncroft, 2018: Genesis of Easterly Waves over the Intra Americas Seas and the tropical Eastern Pacific. *33rd Conference on Hurricanes and Tropical Meteorology*, Ponte Vedra, FL, Amer. Meteor. Soc., 8A.7, URL https://ams.confex.com/ams/33HURRICANE/videogateway.cgi/id/46693?recordingid=46693&uniqueid=Paper340265&entry_password=null.

Torres, V. M., C. D. Thorncroft, and N. M. J. Hall, 2021: Genesis of Easterly Waves over the Tropical Eastern Pacific and the Intra-Americas Sea. *Journal of the Atmospheric Sciences*, doi:10.1175/JAS-D-20-0389.1, URL https://journals.ametsoc.org/view/journals/atsc/aop/JAS-D-20-0389.1/JAS-D-20-0389.1.xml.

Trenberth, K. E., and C. J. Guillemot, 1998: Evaluation of the atmospheric moisture and hydrological cycle in the NCEP/NCAR reanalyses. *Climate Dynamics*, **14 (3)**, 213–231, doi: 10.1007/s003820050219.

Velasco, I., and J. M. Fritsch, 1987: Mesoscale Convective Complexes in the Americas. *J. Geophys. Res.*, **92 (D8)**, 9591–9613.

Wang, C., 2007: Variability of the Caribbean Low-Level Jet and its relations to climate. *Climate Dynamics*, **29 (4)**, 411–422, doi:10.1007/s00382-007-0243-z.

Wang, C.-c., and G. Magnusdottir, 2006: The ITCZ in the Central and Eastern Pacific on Synoptic Time Scales. *Mon. Wea. Rev.*, **134 (5)**, 1405–1421.

Whitaker, J. W., and E. D. Maloney, 2018: Influence of the Madden-Julian Oscillation and Caribbean Low-Level Jet on East Pacific Easterly Wave Dynamics. *J. Atmos. Sci.*, **75 (4)**, 1121–1141.

Whitaker, J. W., and E. D. Maloney, 2020: Genesis of an East Pacific Easterly Wave from a Panama Bight MCS: A Case Study Analysis from June 2012. *Journal of the Atmospheric Sciences*, **77 (10)**, 3567–3584, doi:10.1175/JAS-D-20-0032.1.

Wolding, B., J. Dias, G. Kiladis, E. Maloney, and M. Branson, 2020: Interactions between Moisture and Tropical Convection. Part II: The Convective Coupling of Equatorial Waves. *Journal of the Atmospheric Sciences*, **77 (5)**, 1801–1819, doi:10.1175/JAS-D-19-0226.1.

Wu, L., J.-L. F. Li, C.-J. Pi, J.-Y. Yu, and J.-P. Chen, 2015: An observationally based evaluation of WRF seasonal simulations over the Central and Eastern Pacific. *Journal of Geophysical Research: Atmospheres*, **120 (20)**, 10,664–10,680, doi:https://doi.org/10.1002/2015JD023561.

Yepes, J., G. Poveda, J. F. Mejía, L. Moreno, and C. Rueda, 2019: CHOCO-JEX: A Research Experiment Focused on the Chocó Low-Level Jet over the Far Eastern Pacific and Western Colombia. *Bull. Amer. Meteor. Soc.*, **100 (5)**, 779–796.

Yoo, J., R. V. Rohli, and J. M. Collins, 2017: Low-Level Westerly Winds, Topography, and Tropical Cyclogenesis of Arlene (2005): Observations and Model Simulations. *The Professional Geographer*, **69 (3)**, 348–361, doi:10.1080/00330124.2016.1252270, URL https://doi.org/10.1080/00330124.2016.1252270, https://doi.org/10.1080/00330124.2016.1252270.

Zehnder, J. A., 1991: The Interaction of Planetary-Scale Tropical Easterly Waves with Topography: A Mechanism for the Initiation of Tropical Cyclones. *J. Atmos. Sci*, **48**, 1217–1230.

Zuluaga, M. D., and R. A. Houze, 2015: Extreme Convection of the Near-Equatorial Americas, Africa, and Adjoining Oceans as seen by TRMM. *Mon. Wea. Rev.*, **143 (1)**, 298–316.